

University of Nebraska - Lincoln

DigitalCommons@University of Nebraska - Lincoln

Theses, Dissertations, and Student Research:
Department of Physics and Astronomy

Physics and Astronomy, Department of

6-2022

Magnetism of novel rare-earth-free intermetallic compounds

Haohan Wang

University of Nebraska - Lincoln, haohan.wang@huskers.unl.edu

Follow this and additional works at: <https://digitalcommons.unl.edu/physicsdiss>



Part of the [Condensed Matter Physics Commons](#)

Wang, Haohan, "Magnetism of novel rare-earth-free intermetallic compounds" (2022). *Theses, Dissertations, and Student Research: Department of Physics and Astronomy*. 57.
<https://digitalcommons.unl.edu/physicsdiss/57>

This Article is brought to you for free and open access by the Physics and Astronomy, Department of at DigitalCommons@University of Nebraska - Lincoln. It has been accepted for inclusion in Theses, Dissertations, and Student Research: Department of Physics and Astronomy by an authorized administrator of DigitalCommons@University of Nebraska - Lincoln.

MAGNETISM OF NOVEL RARE-EARTH-FREE INTERMETALLIC COMPOUNDS

by

Haohan Wang

A DISSERTATION

Presented to the Faculty of
The Graduate College at the University of Nebraska
In Partial Fulfillment of Requirements
For the Degree of Doctor of Philosophy

Major: Physics and Astronomy
Under the Supervision of Professor Xiaoshan Xu

Lincoln, Nebraska

June, 2022

MAGNETISM OF NOVEL RARE-EARTH-FREE INTERMETALLIC COMPOUNDS

Haohan Wang, Ph.D.

University of Nebraska, 2022

Advisor: Xiaoshan Xu

Rare-earth-free magnets have drawn lots of interest because of their low cost, and the production is not limited by the shortage of rare-earth elements. This dissertation focuses on three rare-earth-free materials, Fe-Co-Ti alloys, Fe-Ni-B alloys, and Co-Si. All of them are synthesized by arc melting followed by melt-spinning. $\text{Fe}_{3+x}\text{Co}_{3-x}\text{Ti}_2$ ($x = 0, 2, 3$) alloys exhibit hexagonal crystal structures and show non-collinear spin structures according to neutron diffraction. The magnetic moments have projections on both the c -axis and basal plane, and the corresponding misalignment angle exhibits a nonlinear decrease with x , which we explain as a micromagnetic effect caused by Fe-Co site disorder. To increase the magnetic anisotropy of Fe_2Ni alloy, we dope boron into Fe_2Ni and analyze the structure with X-ray diffraction, which shows face center cubic or body center cubic structure according to different temperatures. Magnetic analysis with magnetometer shows that the presence of boron dramatically increases the anisotropy of Fe-Ni-B alloy. Neutron powder diffraction is employed to investigate the magnetism and spin structure in single-phase B20 $\text{Co}_{1.043}\text{Si}_{0.957}$. The magnetic contributions to the neutron powder diffraction data measured in zero fields are consistent with the helical order among the allowed spin structures derived from group theory. The magnitude of the magnetic moment is larger than the bulk magnetization determined from magnetometry, indicating the formation of a helical spin phase and the associated conical states in high magnetic fields.

Preface

The results presented in Chapter 3 have been published in Physical Review Materials (Haohan Wang, Balamurugan Balasubramanian, Rabindra Pahari, Ralph Skomski, Yaohua Liu, Ashfia Huq, D. J. Sellmyer, and Xiaoshan Xu Physical Review Materials 3, 064403 (2019))

The results in Chapter 5 and Appendix B have been published in Journal of Applied Physics (Haohan Wang, Balamurugan Balasubramanian, Yaohua Liu, Robert Streubel, Rabindra Pahari, Thilini Kumari Ekanayaka, Esha Mishra, Christoph Klewe, Padraic Shafer, Rohan Dhall, Ralph Skomski, David J. Sellmyer, and Xiaoshan Xu Journal of Applied Physics 131, 183902 (2022))

The results in Appendix A have been published in Nanoscale (Balamurugan Balasubramanian, Xin Zhao, Shah R. Valloppilly, Sumit Beniwal, Ralph Skomski, Anandakumar Sarella, Yunlong Jin, Xingzhong Li, Xiaoshan Xu, HuiBo Cao, Haohan Wang, Axel Enders, Cai-Zhuang Wang, Kai-Ming Ho and David J. Sellmyer Nanoscale, 10, 13011 (2018))

ACKNOWLEDGMENTS

First, I would like to thank my advisor, Prof. Xiaoshan Xu, for his guidance, patience, and support during my program. It is my honor to join his group in 2016, and Prof. Xu gave me fantastic ideas for my research. He taught me physics, coding, and, most importantly, creative thinking, which will benefit me after graduation. He infected me with his professionalism and enthusiasm for research. He also provided the opportunity to work on the most advanced instruments in lab and national laboratories. Without his generous support, I will not be able to finish my program.

I want to thank other members of my committee: Prof. Christian Binek, Prof. Shireen Adenwalla, and Prof. Abdelghani Laraoui, for taking their precious time to read my comprehensive report and thesis.

I would like to thank my collaborators Prof. David J. Sellmyer, and his group members: Prof. Ralph Skomski and Dr. Bala Balasubramanian. Working with Prof. Sellmyer and his group is a pleasure since they can always give me fantastic ideas and creative suggestions.

One of my most valuable experiences is my beamtime at Oak Ridge National Laboratory. I would like to thank the scientists: Dr. Yaohua Liu, Dr. Qiang Zhang, Dr. Huibo Cao, and Dr. Ashfia Huq. They offered me great help with hands-on experience and data analysis skills. I am incredibly thankful to Dr. Liu for his help throughout my three stays in Oak Ridge.

I would like to thank all postdoctoral researchers in my group: Dr. Yuewei Yin, Dr. Yu Yun, and Dr. Jing Li. They offered me great help with my research and shared their experience during their Ph.D. periods which has valuable guides to my career. I would also like to thank all graduate students in my group: Dr. Kishan Sinha, Dr. Xuanyuan Jiang, Dr. Corbyn Mellinger, Dr. Yifan Yuan, Detian Yang, Yuanyuan Ni, Xin Li, Bharat Giri, and Bibek Tiwari. I benefit a lot from their presentations and our discussions all the time.

I would like to thank all my friends in Lincoln: Prof. Dingfu Shao and his wife Yao Wang, Prof. Xuegang Chen, Dr. Guanhua Hao, Dr. Zilin Chen, Dr. Ming Li, Dr. Bo Li, Dr. Yi Yang, Dr. Dihua Xue, Dr. Zhao Li, Dr. Bin Zhuo, Xiaojun Wang, Pingyang Tao, Yibo Wang, Tianlin Li, Wuzhang Fang, Furong Yan, Jia Wang, and Haopeng Zhang. We have lots of happy memories in Lincoln during my six years of studies here,

I would like to sincerely thank my college friends who continue their studies in the US: Haolin Chen from UCD, Shichen Tang from UCI, and Shaoyu Huang from PITT. Our discussions share the most recent news, exciting experiences, and different opinions about a future career that is full of happiness and hope.

Finally, I would like to say thank you to my parents and other family members. They are always my strongest supporters. I appreciate their understanding and encouragement.

Table of Contents

Chapter I: Introduction.....	1
1.1 Magnetic Anisotropy.....	1
1.2 Rare-earth-free Hard Magnet.....	4
1.3 Helical Spin Structure.....	8
References	11
Chapter II: Experimental Methods and Principle of Data Analysis.....	20
2.1 Synthesis of Magnetic Alloy	20
2.2 Crystal Structure Analyze	21
2.2.1 X-ray Diffraction and Neutron Diffraction Instruments.....	21
2.2.2 Structure Analysis with Diffraction.....	23
2.2.3 Intensity of Diffracted Beams.....	26
2.3 Intensity Analysis from Neutron Powder Diffraction.....	29
2.3.1 Debye-Waller Factor of Neutron Powder Diffraction.....	30
2.3.2 Magnetic Moment for Ferromagnetic Material from Neutron Powder Diffraction	31
2.3.3 Magnetic Moment for Complex Spin Structure from Neutron Powder Diffraction	32
References	34
Chapter III: Noncollinear Spin Structure in $\text{Fe}_{3+x}\text{Co}_{3-x}\text{Ti}_2$ ($x = 0, 2, 3$) from Neutron Diffraction.....	36

3.1 Introduction	36
3.2 Experimental method.....	38
3.3 Result and Discussion	40
3.3.1 Crystallographic Structure.....	41
3.3.2 Separation of Magnetic and Magnetic Contributions.....	44
3.3.3 Micromagnetic Analysis.....	47
3.4 Summary	53
References	53
Chapter IV: Effect of Boron Doping on Magnetic Anisotropy in Fe₂Ni Alloy Grown by Spin Melting Method.....	60
4.1 Introduction	60
4.2 Experiment Details.....	62
4.3 Crystal Structure of Fe-Ni-B Alloy.....	63
4.4 Magnetic Behavior of Fe-Ni-B Alloy	72
4.5 Summary	74
References	74
Chapter V: Magnetic Moments and Spin Structure in Single-Phase B20 Co_{1+x}Si_{1-x} (x=0.043).....	77
5.1 Introduction	77
5.2 Experiment Details.....	80

5.3 Spin Structure and Magnetic Moment from NPD	82
5.3.1 Crystal Structure	82
5.3.2 Analysis of NPD Peak Broadening.....	83
5.3.3 Separation of Magnetic and Nuclear Contributions of the NPD	85
5.3.4 Group Theory Analysis of Spin Structures Allowed by the B20 Crystal Structure.....	90
5.3.5 Magnitude of the Magnetic Moment	95
5.4 Surface Magnetization Probed by XMCD Spectroscopy	96
5.5 Discussion.....	98
5.6 Summary	99
References	99
Chapter VI: Conclusion and Outlook.....	105
Appendix A: Magnetism of Cobalt-Nitride Measured by Neutron Diffraction.....	106
A.1 Introduction	106
A.2 Experiment Details.....	108
A.3 Crystal Structure of Co-N	108
A.4 Neutron Diffraction of Co₃N	113
A.5 Summary	115
Reference.....	116

Appendix B: Symmetry Analysis of the Spin Structure for CoSi by the Group

Theory	122
B.1 Crystal Symmetry and Space Group	122
B.2 Propagation Vector $k = (0, 0, 0)$	124
B.3 Propagation Vector $k // [100]$	125
B.4 Propagation Vector $k // [111]$	128
B.5 Propagation Vector $k // [110]$	130

Chapter I: Introduction

1.1 Magnetic Anisotropy

Magnetism is one of the most fundamental topics in science. Information technologies ranging from personal computers to mainframes use magnetic materials to store information on tapes, floppy diskettes, and hard disks. More efficient power conversion devices such as motors, transformers, and inductors with magnetic alloys are necessary to enable the growing global demand for energy consumption.[1] Two-dimensional magnetic materials are widely investigated in spintronics, magnetoelectric, and biomedicine.[2–4] Magnetic anisotropy is one of the key properties of magnets. When a physical property of a material is a function of direction, that property is said to exhibit anisotropy. The preference for the magnetization to lie in a particular direction in a sample is called magnetic anisotropy.

Anisotropy includes magnetocrystalline anisotropy and shape anisotropy. Magnetocrystalline anisotropy comes from the crystal structure and spin-orbit interaction of the electrons, which means the magnetic moment produced by electron orbitals is strongly linked to the crystallographic structure. Magnetic materials are easy to magnetize along the easy axis and hard to magnetize along the hard axis. **Fig. 1** shows the crystal structure for Fe, Ni, Co, and the magnetization curve.[5] The easy axis of iron (100) is the hard axis of nickel, and the hard axis of iron (111) is the easy axis of nickel. As the magnetization curve in **Fig. 1** shows, the field needed to magnetize iron to saturation is smaller in the (100) directions than in any others, and the field needed to magnetize nickel to saturation is smaller in the (111) directions than in any others. Cobalt is hexagonal, and its easy axis is the c axis. Saturating the sample in the basal plane is

much more difficult than saturating along the c axis. Cobalt has only one easy axis along the c axis, which is said to be uniaxial anisotropy. For iron and cobalt, cubic structure results in several equivalent easy axis according to symmetry, so they are said to have cubic anisotropy. Examples of Fe, Ni, and Co show that magnetic anisotropy is related to crystal structure. The anisotropy energy is defined as the energy needed to saturate the magnetization in the hard axis minus that needed to saturate along the easy axis.

After saturation, the process of reducing the field to zero leaves some magnetization along the direction in which the field had been applied. In the absence of an external field, the magnetization prefers to lie along the easy directions. The magnetization remaining at $H = 0$ is called the remanence.

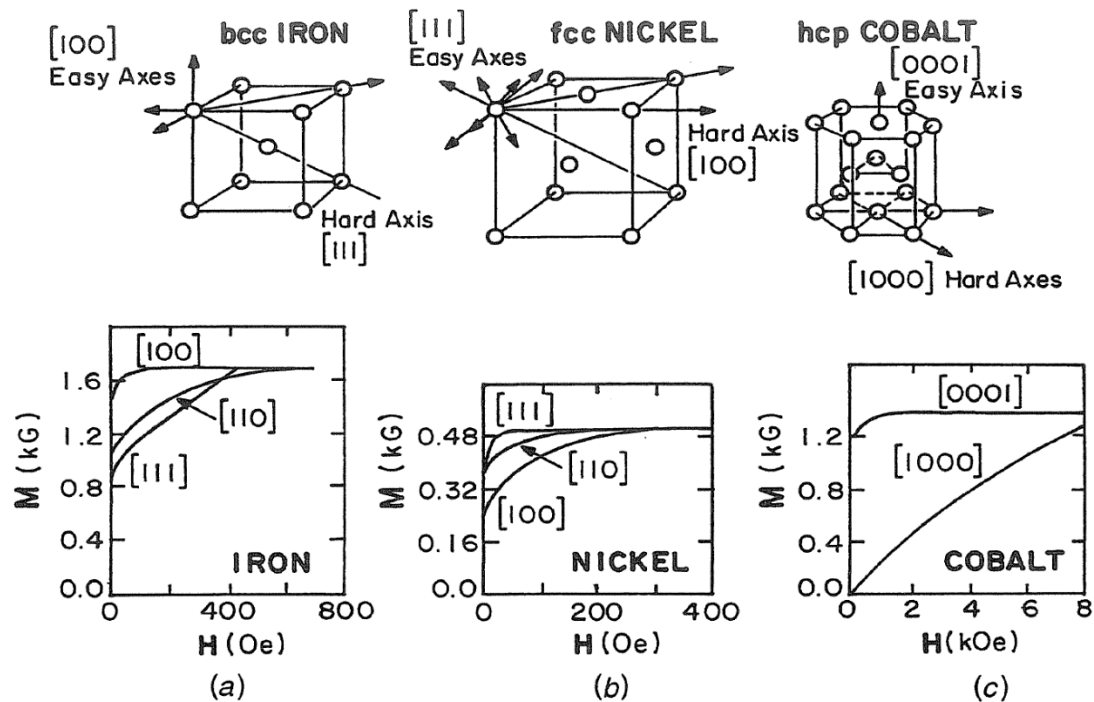


Figure 1.5 Crystal structure showing easy and hard magnetization directions for (a) Fe, (b) Ni, and (c) Co, above. Respective magnetization curves are below.

Shape anisotropy comes from magnetostatic energy. The magnetization generates a demagnetization field. The effect depends on the geometry of the sample, which can be described by the demagnetization tensor N , which depends only on the shape. For example, for a thin film with demagnetizing tensor $N_x = N_y = 0, N_z = 1$, and the z-axis directed across the film's thickness, the volume shape anisotropy is $K_{shape}^V = \mu_0 \frac{M_s^2}{2}$ where M_s is the saturation magnetization.[6] Shape anisotropy is essential since it is an effective way to increase magnetic anisotropy.

The magnetic material can range from soft magnetic to hard magnet. Hard magnets, also referred to as permanent magnets, are magnetic materials that retain their magnetization in zero magnetic fields (high remanence magnetization). The field of a magnetic material to withstand an external magnetic field without becoming demagnetized is called coercivity. Practically, hard magnets have a high coercivity. For example, SmCo_5 has a coercivity larger than 2.7 MA/m (3.5 T).[7] Soft magnets, in contrast, have low remanence magnetization and low coercivity. In some very soft magnetic materials, such as certain crystalline NiFe alloys (permalloys) or amorphous metallic alloys, coercivity can be as low as 1 A/m (12 mOe).[8] By definition, coercivity along the hard axis is always small. However, the coercivity is not necessarily large along the easy axis because the magnetization switching involves nucleation and domain wall motion, the latter takes much smaller energy. The magnetic anisotropy energy limits the maximum value of coercivity. If the domain wall motion dominates, the coercivity along the easy axis will be very small. To achieve high coercivity, one needs to suppress the domain wall motion. This can be done using nanostructures where the grain boundaries hinder the domain wall motion or synthesizing small powder ribbons to minimize the

domain wall motion. Note that there is no clear boundary between soft material and hard material since the definition of soft and hard material is from the applications in the industry.

Magnetic materials with high magnetocrystalline anisotropy are called hard magnets. Hard magnets are widely used in electromotors, generators, loudspeakers, microphones, and so on. More recent key developments are applications in computer hard-disk drives, wind generators, and hybrid-car motors. In industry, high-performance rare-earth transition-metal permanent magnets Sm-Co and Nd₂Fe₁₄B are used.[9–13] Most hard magnets include rare earth elements like Nd and Sm, because they have strong spin-orbit coupling which increases the magnetocrystalline anisotropy. Ordered intermetallic compounds containing strongly spin-orbit coupled nonmagnetic metals (e.g., Pd, Au, and Pt) and ferromagnetic metals (e.g., Fe and Co) can also be good candidates for hard magnets.[14–18] Magnetic anisotropy can also be improved by controlling shape[19] or doping[20].

1.2 Rare-earth-free Hard Magnet

Nd-Fe-B and Sm-Co magnets are widely used for conversion between electricity and mechanical energy. However, the magnetic property of Nd-Fe-B is strongly temperature-dependent, and the increasing demand for rare earth elements has raised the price of oxides like Nd₂O₃. [21] Rare-earth-free magnet is a good substitution for rare earth magnets like Nd-Fe-B and Sm-Co. Most rare-earth-free magnets are based on Fe,

Co, and Ni elements, but they have low magnetic anisotropy energy, so they are hard to be used as a hard magnet.[22]

In magnetic materials, the maximum energy product $(BH)_{max}$ is defined as the maximal value of the product of magnetic flux density B and the magnetic field strength H according to the hysteresis loop, typically given in units of either MGOe (CGS) or kJ/m^3 (SI) (1 MGOe is equal to 7.958 kJ/m^3). It is a variable that serves as a measure of the magnetic energy stored in a magnet. Usually, a rare-earth-magnet has a high energy product larger than 239 kJ/m^3 (30 MGOe).[21]

People try hard to solve the low anisotropy energy problem of rare-earth-free magnets. Alnico is the class of alloys contains Al, Ni, Co, thus its name. Sometimes it also contains copper, iron, and titanium. Alnico has a high Curie temperature (1073 K) and a high energy product of 159 kJ/m^3 (20 MGOe), but it is limited by its low magnetocrystalline anisotropy of 0.3 MJ/m^3 ($3 \times 10^6 \text{ erg/cm}^3$).[21] Further study of well-ordered $\text{L}_{10}\text{-FeNi}$ shows a high magnetic anisotropy of about 1 MJ/m^3 ($1 \times 10^7 \text{ erg/cm}^3$) and a $(BH)_{max}$ of 446 kJ/m^3 (56 MGOe).[23] $\text{L}_{10}\text{-FeNi}$ is discovered in meteorite[24] and can produce in thin films by alternate monatomic layer deposition.[25,26] However, bulk $\text{L}_{10}\text{-FeNi}$ is only found in meteorites since it requires billions of years to anneal at extremely low cooling rates.[27] Similarly, $\text{L}_{10}\text{-FeCo}$ has theoretical magnetic anisotropy as high as 10 MJ/m^3 ($1 \times 10^8 \text{ erg/cm}^3$),[28] but only thin film samples can be produced in the lab, and no bulk sample has been synthesized yet.[29]

Cobalt-rich intermetallic materials like HfCo_7 and $\text{Zr}_2\text{Co}_{11}$ are also treated as good candidates for rare-earth-free hard magnets. For HfCo_7 , the magnetic anisotropy is 1.4 MJ/m^3 ($1.4 \times 10^7 \text{ erg/cm}^3$); for $\text{Zr}_2\text{Co}_{11}$, the magnetic anisotropy is 1.35 MJ/m^3

(1.35×10^7 erg/cm³).[30] However, the hard magnetic structures for both materials are high-temperature metastable phase which is only available in nanoparticles instead of bulk material.[31,32] The energy products of bulk HfCo₇ and Zr₂Co₁₁ are 34 kJ/m³ (4.3 MGOe) and 42 kJ/m³ (5.3 MGOe), respectively, which is far lower than the theoretical value (259 kJ/m³ /32.5 MGOe and 207 kJ/m³ /26 MGOe, respectively for HfCo₇ and Zr₂Co₁₁).[30] **Fig. 2** shows the hard magnetic structure for HfCo₇ (orthorhombic) and Zr₂Co₁₁ (rhombohedral).[31,32]

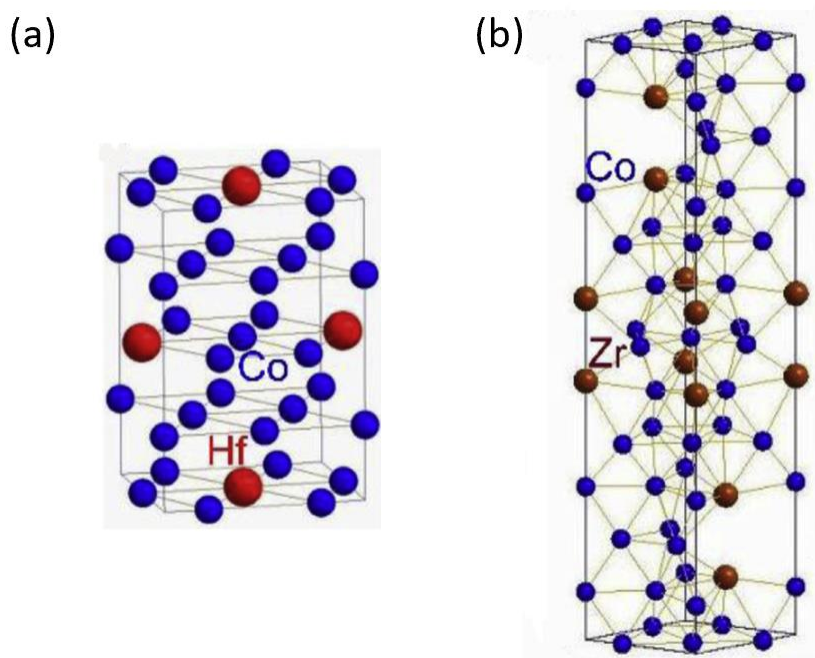


Figure 2. Hard magnet crystal structure of (a) orthorhombic HfCo₇ [31] and (b) rhombohedral Zr₂Co₁₁. [32]

Some rare-earth-free hard magnet does not contain Fe, Co, or Ni. Manganese-based alloy (Mn-B, Mn-Ga, Mn-Ge, Mn-Sb Mn-Al, Mn-Bi, and Mn-As) exhibits ferromagnetism, while manganese is antiferromagnetic.[21] Only Mn-Al and Mn-Bi have

large enough magnetic anisotropy as a hard magnet among these candidates. The theoretical magnetic anisotropy energy of the well-ordered tetragonal $L1_0$ structure τ -MnAl can be as high as 1.5 MJ/m^3 ($1.5 \times 10^7 \text{ erg/cm}^3$) with a magnetic moment of $2.2 \times 10^{-23} \text{ A} \cdot \text{m}^2$ ($2.4 \mu_B$) per formula unit ($0.164 \text{ A} \cdot \text{m}^2/\text{g}$ or 164 emu/g) and a maximal energy product of 105 kJ/m^3 (13.2 MGOe).[33] **Fig. 3(a)** shows the crystal structure of τ -MnAl. Experimental powder samples can show results similar to the theoretical value, $K_I \approx 1 \text{ MJ/m}^3$ ($1 \times 10^7 \text{ erg/cm}^3$), and $M_s \approx 0.11 \text{ A} \cdot \text{m}^2/\text{g}$ (110 emu/g).[34] However, metastable τ -phase MnAl is hard to obtain in bulk material, so the experimental magnetic property in bulk is far from theory. α -MnBi has a trigonal structure shown in **Fig 3(b)**. Powder α -MnBi has a magnetic moment of $0.08 \text{ A} \cdot \text{m}^2/\text{g}$ (80 emu/g), magnetic anisotropy energy of 1.6 MJ/m^3 ($1.6 \times 10^7 \text{ erg/cm}^3$), and maximal energy product of 159 kJ/m^3 (20 MGOe) at room temperature.[35] However, Mn-Bi has a similar problem to Mn-Al, that it is difficult to form a high-purity bulk α -MnBi. The magnetic property of bulk is usually not impressive.[36,37]

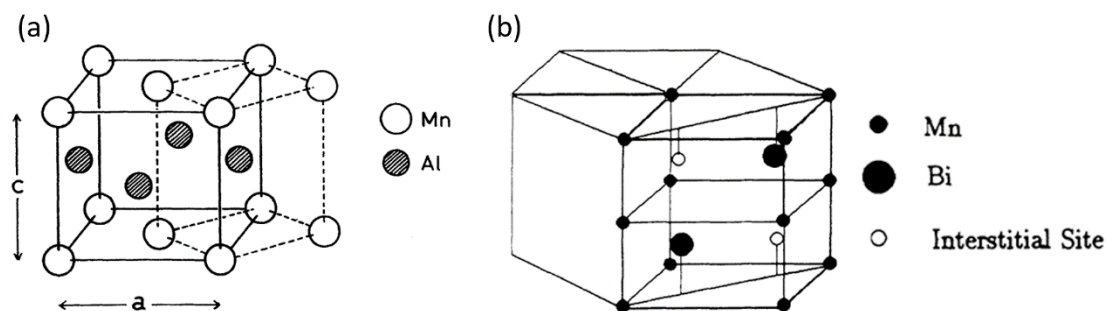


Figure 3. Crystal structure of (a) $L1_0$ structure τ -MnAl[34] and (b)trigonal α -MnBi[35].

1.3 Helical Spin Structure

When magnetic moments in a material align in the same direction, it is called a ferromagnetic material. When magnetic moments in the material have more than one direction and the total magnetic moments are not cancelled, it is called a ferrimagnetic material. If the total magnetic moments cancel, it is called an antiferromagnetic material. Helimagnetic material is just in between and has a helical spin structure that exhibits long-range antiferromagnetic and short-range ferromagnetic orders. The helical spin structure is one of the spiral spin structures. **Fig. 4** shows different kinds of spiral spin structures.[38]

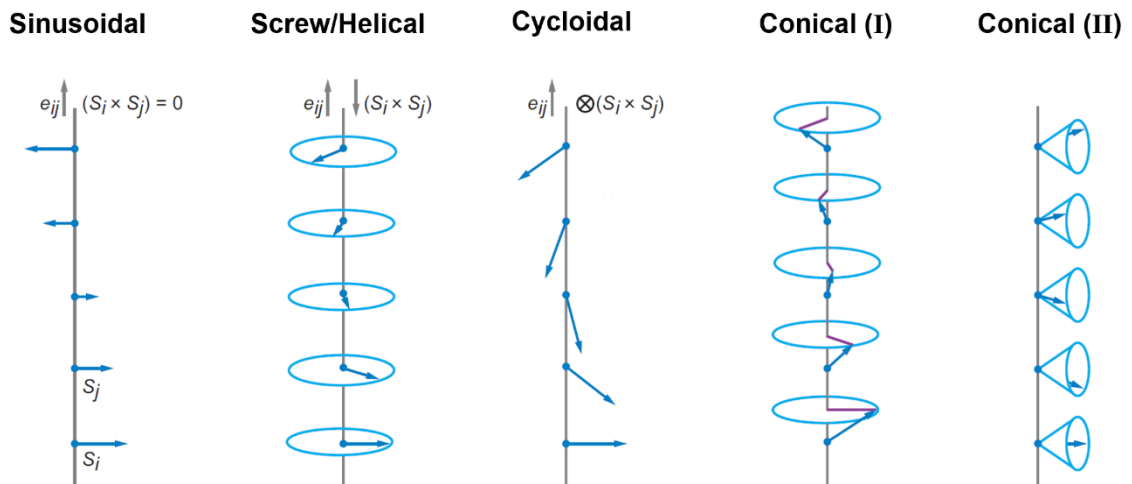


Figure 4. [38] Schematic illustrations of different types of spiral structures. (a)

Sinusoidal, (b) screw/helical, (c) cycloidal, and (d,e) conical structures. e_{ij} connects the neighboring magnetic moments S_i and S_j at i and j sites that have the same direction with the propagation vector.

Long-period helical structure comes from Dzyaloshinskii-Moriya (DM) exchange interaction. The long-range magnetic order was observed by neutron diffraction several decades ago,[39–42] while helical order gives rise to sharp Bragg peaks in neutron diffraction corresponding to the periodicity of the helical spin-density wave which is always different from the crystal period.[43,44] Other experiment methods exist to see the helical structure. Topological Hall effect can measure the Berry phase produced by helical spins.[45–47] Recent studies show helical structure can also be observed by Lorentz transmission electron microscopy[48,49] and spin-polarized scanning tunneling microscopy.[50,51]

Several materials have helical spin structures. Some RFeO₃ materials exhibit helical spins. BiFeO₃ has a helical spin structure with a period of 620 Å.[52] while the helical period of SrFeO₃ is 220 Å.[42] Another group of materials with a helical spin structure is the B20 material. B20 material has forms of MSi or MGe, where M can be Fe, Co, or Mn.[53–59] DM interaction is allowed when there is no inversion symmetry, So non-centrosymmetric P2₁3 space group of B20 material allows the DM interaction and therefore result in a helical or conical spin propagating along (111) or (100) directions. **Fig. 5** shows the crystal structure of BiFeO₃ and B20 material.

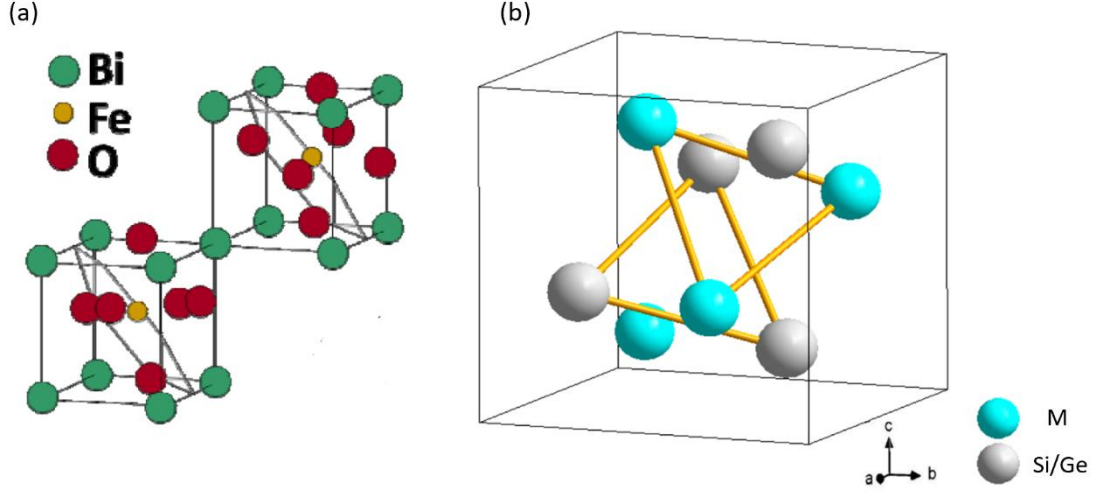


Figure 5. Crystal structure of (a) BiFeO₃ [52] and (b) MSi and MGe of B20 structures (M is Fe, Co, or Mn).

When there is no applied field, the free energy of a system with DM interaction can be written as [60]

$$F = AM^2 - \frac{J}{2} M \cdot \nabla^2 \vec{M} + 2D\vec{M} \cdot (\nabla \times \vec{M}) \quad (1.1)$$

Here, A , J , and D are parameters, AM^2 represent anisotropy energy, $-\frac{J}{2} M \cdot \nabla^2 \vec{M}$ represent exchange energy, and $2D\vec{M} \cdot (\nabla \times \vec{M})$ represent DM interaction. A magnetic spin \vec{M} of a helical structure can be written as,

$$\vec{M} = M_0 [\hat{e}_1 \cos(\vec{k} \cdot \vec{r}) + \hat{e}_2 \sin(\vec{k} \cdot \vec{r})] \quad (1.2)$$

where the propagation vector is parallel to $\hat{e}_1 \times \hat{e}_2$.

Substitute \vec{M} into the free energy gives,

$$\begin{aligned}
F &= AM^2 - \frac{J}{2} M \cdot \nabla^2 \vec{M} + 2D\vec{M} \cdot (\nabla \times \vec{M}) \\
&= AM_o^2 - \frac{J}{2} M \{M_o k^2 \cdot [-\hat{e}_1 \cos(\vec{k} \cdot \vec{r}) - \hat{e}_2 \sin(\vec{k} \cdot \vec{r})]\} \\
&\quad + 2D\vec{M} \cdot M_o k [-\hat{e}_2 \sin(\vec{k} \cdot \vec{r}) - \hat{e}_1 \cos(\vec{k} \cdot \vec{r})] \\
&= AM_o^2 + \frac{J}{2} k^2 M_o^2 - 2DkM_o^2
\end{aligned} \tag{1.3}$$

the minimization leads to

$$\frac{\partial F}{\partial k} = 0 \rightarrow JkM^2 - 2DM^2 = 0 \tag{1.4}$$

$$\rightarrow k = \frac{2D}{J} = \frac{2\pi}{\lambda} \tag{1.5}$$

Where λ is the helical period. This means the period of the helical structure is related to the exchange interaction and DM interaction. If the exchange interaction J is strong, the spins tend to be parallel to neighbors so that the helical period is long. Oppositely, if the DM interaction D is strong, the spins tend to be perpendicular to neighbors so that the helical period is small.

References

- [1] M. S J, Enzo F, L. H D and C. M T 2018 Soft magnetic materials for a sustainable and electrified world *Science*. **362** eaao0195
- [2] Sethulakshmi N, Mishra A, Ajayan P M, Kawazoe Y, Roy A K, Singh A K and Tiwary C S 2019 Magnetism in two-dimensional materials beyond graphene

Mater. Today **27** 107–22

- [3] Gibertini M, Koperski M, Morpurgo A F and Novoselov K S 2019 Magnetic 2D materials and heterostructures *Nat. Nanotechnol.* **14** 408–19
- [4] Cheng G and Xiang Z 2019 Two-dimensional magnetic crystals and emergent heterostructure devices *Science.* **363** eaav4450
- [5] O’Handley and C R 2000 *Modern magnetic materials : principles and applications* (New York: Wiley)
- [6] Gruszecki P, Banerjee C, Mruczkiewicz M, Hellwig O, Barman A and Krawczyk M 2019 Chapter Two - The influence of the internal domain wall structure on spin wave band structure in periodic magnetic stripe domain patterns *Recent Advances in Topological Ferroics and their Dynamics* vol 70, ed R L Stamps and H B T-S S P Schultheiß (Academic Press) pp 79–132
- [7] de Campos M F, Landgraf F J G, Saito N H, Romero S A, Neiva A C, Missell F P, de Moraes E, Gama S, Obrucheveva E V and Jalnin B V 1998 Chemical composition and coercivity of SmCo₅ magnets *J. Appl. Phys.* **84** 368–73
- [8] Jerome R, Valet T and Galtier P 1994 Correlation between magnetic and structural properties of Ni₈₀Fe₂₀ sputtered thin films deposited on Cr and Ta buffer layers *IEEE Trans. Magn.* **30** 4878–80
- [9] Kumar K 1988 RETM₅ and RE₂TM₁₇ permanent magnets development *J. Appl. Phys.* **63** R13–57
- [10] Strnat K, Hoffer G, Olson J, Ostertag W and Becker J J 1967 A Family of New

- Cobalt-Base Permanent Magnet Materials *J. Appl. Phys.* **38** 1001–2
- [11] Herbst J F 1991 R₂Fe₁₄B materials: Intrinsic properties and technological aspects *Rev. Mod. Phys.* **63** 819–98
- [12] Sagawa M, Fujimura S, Yamamoto H, Matsuura Y and Hiraga K 1984 Permanent magnet materials based on the rare earth-iron-boron tetragonal compounds *IEEE Trans. Magn.* **20** 1584–9
- [13] Sagawa M, Hirosawa S, Yamamoto H, Fujimura S and Matsuura Y 1987 Nd–Fe–B Permanent Magnet Materials *Jpn. J. Appl. Phys.* **26** 785–800
- [14] Tudu B and Tiwari A 2017 Recent Developments in Perpendicular Magnetic Anisotropy Thin Films for Data Storage Applications *Vacuum* **146** 329–41
- [15] Sbiaa R, Meng H and Piramanayagam S N 2011 Materials with perpendicular magnetic anisotropy for magnetic random access memory *Phys. status solidi – Rapid Res. Lett.* **5** 413–9
- [16] Sakuma A 1994 First Principle Calculation of the Magnetocrystalline Anisotropy Energy of FePt and CoPt Ordered Alloys *J. Phys. Soc. Japan* **63** 3053–8
- [17] Daalderop G H O, Kelly P J and Schuurmans M F H 1991 Magnetocrystalline anisotropy and orbital moments in transition-metal compounds *Phys. Rev. B* **44** 12054–7
- [18] Shick A B and Mryasov O N 2003 Coulomb correlations and magnetic anisotropy in ordered L1₀ CoPt and FePt alloys *Phys. Rev. B* **67** 172407
- [19] Lu Y, Altman R A, Marley A, Rishton S A, Trouilloud P L, Xiao G, Gallagher W

- J and Parkin S S P 1997 Shape-anisotropy-controlled magnetoresistive response in magnetic tunnel junctions *Appl. Phys. Lett.* **70** 2610–2
- [20] Nozaki T, Yamamoto T, Tamaru S, Kubota H, Fukushima A, Suzuki Y and Yuasa S 2018 Enhancement in the interfacial perpendicular magnetic anisotropy and the voltage-controlled magnetic anisotropy by heavy metal doping at the Fe/MgO interface *APL Mater.* **6** 26101
- [21] Cui J, Kramer M, Zhou L, Liu F, Gabay A, Hadjipanayis G, Balasubramanian B and Sellmyer D 2018 Current progress and future challenges in rare-earth-free permanent magnets *Acta Mater.* **158** 118–37
- [22] Burkert T, Eriksson O, James P, Simak S I, Johansson B and Nordström L 2004 Calculation of uniaxial magnetic anisotropy energy of tetragonal and trigonal Fe, Co, and Ni *Phys. Rev. B* **69** 104426
- [23] Paulevé J, Chamberod A, Krebs K and Bourret A 1968 Magnetization Curves of Fe–Ni (50–50) Single Crystals Ordered by Neutron Irradiation with an Applied Magnetic Field *J. Appl. Phys.* **39** 989–90
- [24] Lee S, Edalati K, Iwaoka H, Horita Z, Ohtsuki T, Ohkochi T, Kotsugi M, Kojima T, Mizuguchi M and Takanashi K 2014 Formation of FeNi with L1₀-ordered structure using high-pressure torsion *Philos. Mag. Lett.* **94** 639–46
- [25] Shima T, Okamura M, Mitani S and Takanashi K 2007 Structure and magnetic properties for L1₀-ordered FeNi films prepared by alternate monatomic layer deposition *J. Magn. Magn. Mater.* **310** 2213–4

- [26] Mizuguchi M, Kojima T, Kotsugi M, Koganezawa T, Osaka K and Takanashi K 2011 Artificial Fabrication and Order Parameter Estimation of $L1_0$ -ordered FeNi Thin Film Grown on a AuNi Buffer Layer *J. Magn. Soc. Japan* **35** 370–3
- [27] Néel L, Pauleve J, Pauthenet R, Laugier J and Dautreppe D 1964 Magnetic Properties of an Iron—Nickel Single Crystal Ordered by Neutron Bombardment *J. Appl. Phys.* **35** 873–6
- [28] Burkert T, Nordström L, Eriksson O and Heinonen O 2004 Giant Magnetic Anisotropy in Tetragonal FeCo Alloys *Phys. Rev. Lett.* **93** 27203
- [29] Winkelmann A, Przybylski M, Luo F, Shi Y and Barthel J 2006 Perpendicular Magnetic Anisotropy Induced by Tetragonal Distortion of FeCo Alloy Films Grown on Pd(001) *Phys. Rev. Lett.* **96** 257205
- [30] Balamurugan B, Das B, Zhang W Y, Skomski R and Sellmyer D J 2014 Hf–Co and Zr–Co alloys for rare-earth-free permanent magnets *J. Phys. Condens. Matter* **26** 64204
- [31] Zhao X, Nguyen M C, Zhang W Y, Wang C Z, Kramer M J, Sellmyer D J, Li X Z, Zhang F, Ke L Q, Antropov V P and Ho K M 2014 Exploring the Structural Complexity of Intermetallic Compounds by an Adaptive Genetic Algorithm *Phys. Rev. Lett.* **112** 45502
- [32] Das B, Balamurugan B, Kumar P, Skomski R, Shah V R, Shield J E, Kashyap A and Sellmyer D J 2013 HfCo₇-Based Rare-Earth-Free Permanent-Magnet Alloys *IEEE Trans. Magn.* **49** 3330–3

- [33] Sakuma A 1994 Electronic Structure and Magnetocrystalline Anisotropy Energy of MnAl *J. Phys. Soc. Japan* **63** 1422–8
- [34] Pareti L, Bolzoni F, Leccabue F and Ermakov A E 1986 Magnetic anisotropy of MnAl and MnAlC permanent magnet materials *J. Appl. Phys.* **59** 3824–8
- [35] Guo X, Chen X, Altounian Z and Ström-Olsen J O 1992 Magnetic properties of MnBi prepared by rapid solidification *Phys. Rev. B* **46** 14578–82
- [36] Poudyal N, Liu X, Wang W, Nguyen V V, Ma Y, Gandha K, Elkins K, Liu J P, Sun K, Kramer M J and Cui J 2016 Processing of MnBi bulk magnets with enhanced energy product *AIP Adv.* **6** 56004
- [37] Kim S, Moon H, Jung H, Kim S-M, Lee H-S, Choi-Yim H and Lee W 2017 Magnetic properties of large-scaled MnBi bulk magnets *J. Alloys Compd.* **708** 1245–9
- [38] Kimura T 2007 Spiral Magnets as Magnetoelectrics *Annu. Rev. Mater. Res.* **37** 387–413
- [39] Tomiyoshi S and Watanabe H 1975 Helical Spin Structure of Mn₃Si *J. Phys. Soc. Japan* **39** 295–302
- [40] Takeuchi S and Motizuki K 1968 Stability of the Helical Spin Structure in MnP *J. Phys. Soc. Japan* **24** 742–50
- [41] Ishimoto K, Yamaguchi Y, Mitsuda S, Ishida M and Endoh Y 1986 Stability and winding of the long period helical spin structure in Fe_{1-x}Co_xSi *J. Magn. Magn. Mater.* **54–57** 1003–4

- [42] Takeda T, Yamaguchi Y and Watanabe H 1972 Magnetic Structure of SrFeO₃ *J. Phys. Soc. Japan* **33** 967–9
- [43] Binz B and Vishwanath A 2006 Theory of helical spin crystals: Phases, textures, and properties *Phys. Rev. B* **74** 214408
- [44] Pfleiderer C, Reznik D, Pintschovius L, Löhneysen H v., Garst M and Rosch A 2004 Partial order in the non-Fermi-liquid phase of MnSi *Nature* **427** 227–31
- [45] Kanazawa N, Onose Y, Arima T, Okuyama D, Ohoyama K, Wakimoto S, Kakurai K, Ishiwata S and Tokura Y 2011 Large Topological Hall Effect in a Short-Period Helimagnet MnGe *Phys. Rev. Lett.* **106** 156603
- [46] Shiomi Y, Iguchi S and Tokura Y 2012 Emergence of topological Hall effect from fanlike spin structure as modified by Dzyaloshinsky-Moriya interaction in MnP *Phys. Rev. B* **86** 180404
- [47] Chakraverty S, Matsuda T, Wadati H, Okamoto J, Yamasaki Y, Nakao H, Murakami Y, Ishiwata S, Kawasaki M, Taguchi Y, Tokura Y and Hwang H Y 2013 Multiple helimagnetic phases and topological Hall effect in epitaxial thin films of pristine and Co-doped SrFeO₃ *Phys. Rev. B* **88** 220405
- [48] Togawa Y, Kishine J, Nosov P A, Koyama T, Paterson G W, McVitie S, Kousaka Y, Akimitsu J, Ogata M and Ovchinnikov A S 2019 Anomalous Temperature Behavior of the Chiral Spin Helix in CrNb₃S₆ Thin Lamellae *Phys. Rev. Lett.* **122** 17204
- [49] Gao Y, Zheng X, Li Z, Xu J, Qi J, Guo Y, Hu C, Qin W, He C, Shen S, Wei H,

- Zhang Y and Wang S 2022 Real-space observation of non-collinear spin structure in centrosymmetric TbGa rare-earth magnet *AIP Adv.* **12** 55315
- [50] Meckler S, Mikuszeit N, Preßler A, Vedmedenko E Y, Pietzsch O and Wiesendanger R 2009 Real-Space Observation of a Right-Rotating Inhomogeneous Cycloidal Spin Spiral by Spin-Polarized Scanning Tunneling Microscopy in a Triple Axes Vector Magnet *Phys. Rev. Lett.* **103** 157201
- [51] Haze M, Yoshida Y and Hasegawa Y 2017 Experimental verification of the rotational type of chiral spin spiral structures by spin-polarized scanning tunneling microscopy *Sci. Rep.* **7** 13269
- [52] Ederer C and Spaldin N A 2005 Weak ferromagnetism and magnetoelectric coupling in bismuth ferrite *Phys. Rev. B* **71** 60401
- [53] Jeong T and Pickett W E 2004 Implications of the B20 crystal structure for the magnetoelectronic structure of MnSi *Phys. Rev. B - Condens. Matter Mater. Phys.* **70** 075114
- [54] Beille J, Voiron J and Roth M 1983 Long period helimagnetism in the cubic B20 $\text{Fe}_x\text{Co}_{1-x}\text{Si}$ and $\text{Co}_x\text{Mn}_{1-x}\text{Si}$ alloys *Solid State Commun.* **47** 399–402
- [55] Beille J, Voiron J, Towfiq F, Roth M and Zhang Z Y 1981 Helimagnetic structure of the $\text{Fe}_x\text{Co}_{1-x}\text{Si}$ alloys *J. Phys. F Met. Phys.* **11** 2153–60
- [56] Kanazawa N, Onose Y, Arima T, Okuyama D, Ohoyama K, Wakimoto S, Kakurai K, Ishiwata S and Tokura Y 2011 Large topological hall effect in a short-period helimagnet MnGe *Phys. Rev. Lett.* **106** 156603

- [57] Bauer A, Neubauer A, Franz C, Münzer W, Garst M and Pfleiderer C 2010 Quantum phase transitions in single-crystal $\text{Mn}_{1-x}\text{Fe}_x\text{Si}$ and $\text{Mn}_{1-x}\text{Co}_x\text{Si}$: Crystal growth, magnetization, ac susceptibility, and specific heat *Phys. Rev. B* **82** 64404
- [58] Zheng F, Rybakov F N, Borisov A B, Song D, Wang S, Li Z A, Du H, Kiselev N S, Caron J, Kovács A, Tian M, Zhang Y, Blügel S and Dunin-Borkowski R E 2018 Experimental observation of chiral magnetic bobbbers in B20-type FeGe *Nat. Nanotechnol.* **13** 451–5
- [59] Spencer C S, Gayles J, Porter N A, Sugimoto S, Aslam Z, Kinane C J, Charlton T R, Freimuth F, Chadov S, Langridge S, Sinova J, Felser C, Blügel S, Mokrousov Y and Marrows C H 2018 Helical magnetic structure and the anomalous and topological Hall effects in epitaxial B20 $\text{Fe}_{1-y}\text{Co}_y\text{Ge}$ films *Phys. Rev. B* **97** 214406
- [60] Bak P and Jensen M H 1980 Theory of helical magnetic structures and phase transitions in MnSi and FeGe *J. Phys. C Solid State Phys.* **13** L881–5

Chapter II: Experimental Methods and Principle of Data Analysis

This Chapter includes the synthesis, characterization, and neutron powder diffraction analysis for the magnetic moment.

2.1 Synthesis of Magnetic Alloy

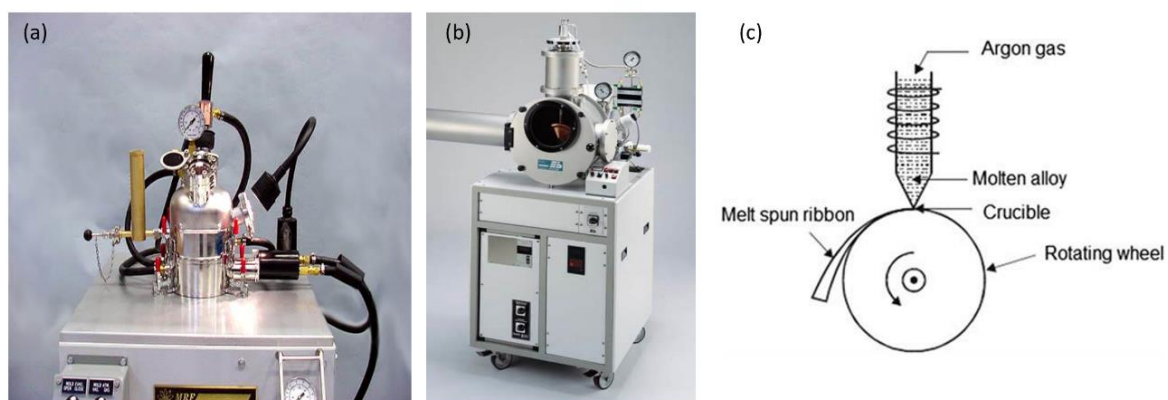


Figure 2.1: Picture of (a) ABJ-338 Bell Jar Arc-Melting Furnace,[1] (b) Edmund Bühler GmbH Melt Spinner SC,[2] and (c) the sketch inside the chamber of melt spinning. [3]

The polycrystalline samples are produced by conventionally melting appropriate amounts of high purity material, followed by melt spinning. The samples are put in an arc melting furnace ABJ-338 and melted via an electric arc struck between a tungsten electrode and metals placed in a copper holder. In our experiment, the chamber is backfilled with Argon to ensure the alloy does not interact with oxygen. After the materials are melted into a bulk alloy, this alloy is put into a melt-spinning instrument (Edmund Bühler GmbH melt spinner SC) with an argon environment. The melt spinning instrument drops melted liquid alloys onto a rotating wheel, which is cooled internally. A

wheel speed of 15-25 m/s was used to produce rapidly quenched ribbons of approximate width of 2 mm and thickness of 40 μm . **Fig. 2.1** shows the picture of arc melting, melt spinning, and the sketch inside the chamber of melt spinning.

2.2 Crystal Structure Analyze

2.2.1 X-ray Diffraction and Neutron Diffraction Instruments.

The X-ray diffraction was carried out with *Rigaku SmartLab X-ray Diffractometer* and *PANalytical Empyrean Diffractometer*, both using Cu K α radiation of a wavelength of 1.5406 Å. SmartLab is famous for its high resolution and multiple features. Empyrean produces a high-intensity X-ray beam, which is suitable for powder samples.

Neutron diffraction was carried out at Oak Ridge National Laboratory. Thin-film neutron diffraction was done with a dimensional extreme magnetic neutron diffractometer, DEMAND. DEMAND has a four-circle mode with the χ circle goniometer, which can operate with a closed-cycle-refrigerator (4 K to 800 K), and a detector sits on the 2θ rotation arm to cover the scattering angle range of $3^\circ < 2\theta < 155^\circ$. A monochromator was used to select polarized neutron with a wavelength of 1.005 Å, 1.546 Å, and 2.541 Å. **Fig. 2.2** shows the picture of the DEMAND beamline.

Temperature-dependent high-resolution neutron powder diffraction measurements were carried out without an external magnetic field on the time-of-flight (TOF) powder diffractometer, POWGEN. POWGEN is a third-generation powder diffractometer with the highest resolution to probe large unit cells in the powder suite at the Spallation Neutron Source Oak Ridge National Laboratory. The data were collected with neutrons with a central wavelength of 2.665 Å. A cryofurnace was used as the sample environment

to cover the temperature region between 20 K and 600K. **Fig. 2.3** shows the picture of the POWGEN beamline.



Figure 2.2: Picture of DEMAND beamline in Oak Ridge National Laboratory.[4]



Figure 2.3: Picture of POWGEN beamline in Oak Ridge National Laboratory.[5]

2.2.2 Structure Analysis with Diffraction

The crystal structure can be analyzed with diffraction. The sketch of X-ray diffracting on the crystal is shown in **Fig. 2.4**. The atom of the crystal is arranged on a set of parallel planes A, B, C, D, ..., normal to the plane of the drawing and spaced a distance d' apart. X-ray beam of wavelength λ is incident on this crystal at an incident angle θ , which is the angle between the incident beam and the crystal planes. The angle between diffracted beam and the crystal planes is θ , too. Diffraction appears where has a path difference. For example, the difference in the length of the path between rays I and Ia is

$$QK - PR = PK\cos\theta - PK\cos\theta = 0 \quad (2.1)$$

So, the rays scattered by all the atoms on the same plane are diffracted. For rays I and 2 , the path difference for rays IKI' and $2L2'$ is

$$ML + LN = d'\sin\theta + d'\sin\theta = 2d'\sin\theta \quad (2.2)$$

This is also the path difference for all rays scattered by planes A and B. The scattered rays are completely in phase if the path difference is equal to a whole number n of wavelengths,

$$n\lambda = 2d'\sin\theta \quad (2.3)$$

This relation is known as Bragg's law, n is called the order of diffraction ($n = 1, 2, 3, \dots$).

Bragg's law can also be written as

$$\lambda = 2\frac{d'}{n}\sin\theta \quad (2.4)$$

For convenience, we can have $d=d'/2$ so that

$$\lambda = 2d\sin\theta \quad (2.5)$$

which is the most common form of Bragg's law.

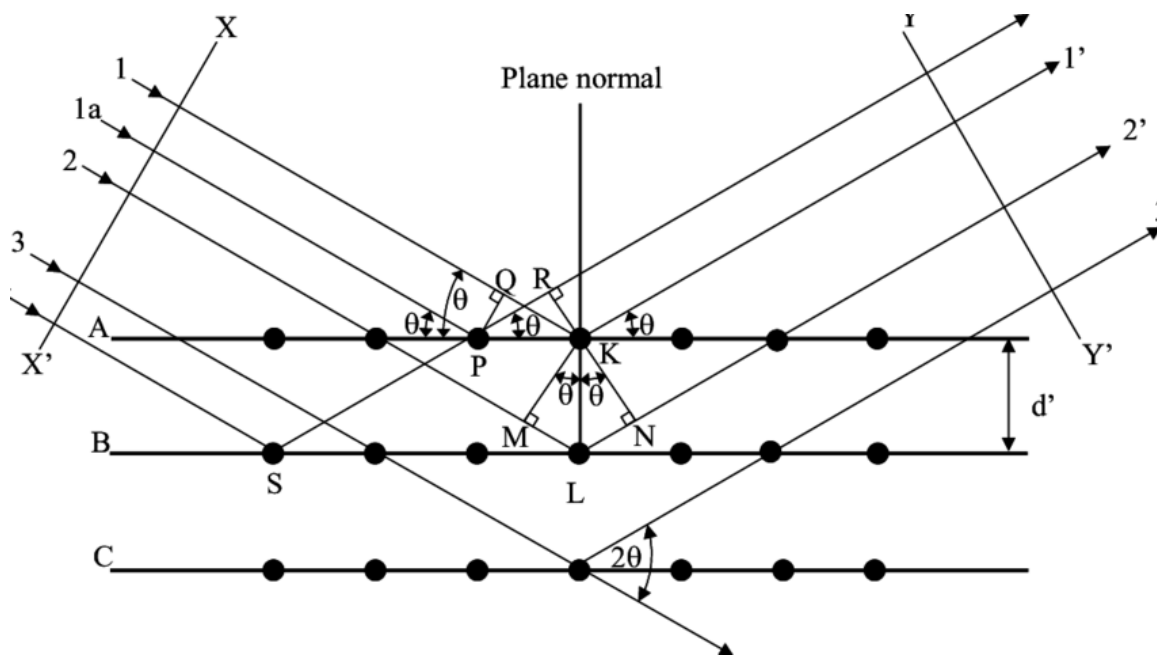


Figure 2.4: Diffraction of X-rays by a crystal.[6]

X-ray diffraction uses a monochromator to choose a specific wavelength λ of X-rays. DEMAND also uses a monochromator, so the wavelength of the neutron is fixed. However, in POWGEN, the wavelength of the neutrons is a wide range related to their speed.

Fig. 2.5 shows the sketch of neutron powder diffraction in POEGEN. A pulsed neutron beam incidents into a selection device to choose a specific range of neutron speed, the selected neutron then incident on the sample and diffracted to the detector, the detector records the time the neutron travels from the source to the detector (time-of-flight) and the angle position 2θ of the diffracted neutron. The wavelength of the neutron is

$$\lambda = \frac{h}{p} = \frac{h}{mv} = \frac{ht}{mL} \quad (2.6)$$

Where p is the momentum of the neutron, h is the Planck constant, v is the speed of the neutron, m is the mass of the neutron, and t is the time of pulsed neutron travels from the source to the detector, which is recorded by the detector, L is the distance between the source to the detector which is 60 meters in POWGEN. Substitute this Eq. (2.6) to Bragg's law

$$d = \frac{ht}{2mL\sin\theta} \quad (2.7)$$

Eq. (2.7) shows how we can get diffraction peaks in neutron diffraction.

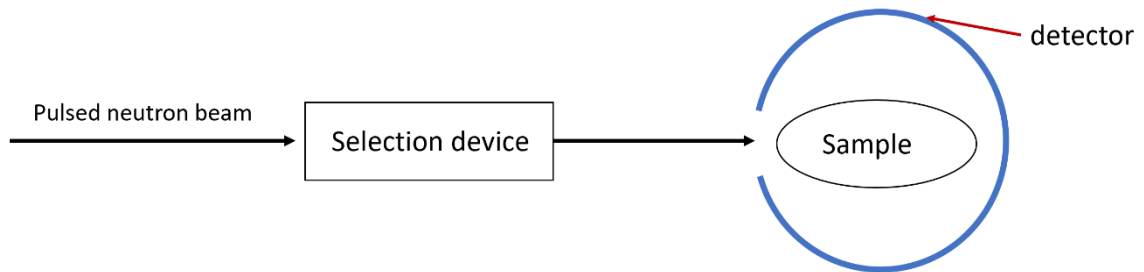


Figure 2.5: a sketch of neutron powder diffraction in POWGEN

2.2.3 Intensity of Diffracted Beams

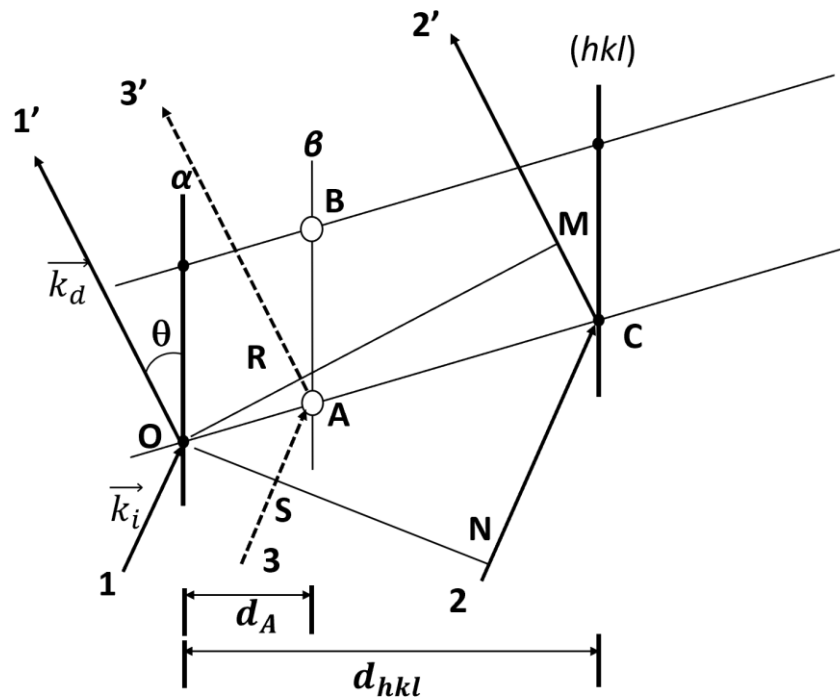


Figure 2.6: A sketch of diffraction that occurred on the plane (hkl) .

The phase difference between beams determines the intensity of the beam. For convenience, consider diffraction that occurs in an orthorhombic unit cell. **Fig. 2.6** shows the diffraction condition of the plane (hkl) inside an orthorhombic crystal with parameters a , b , and c in x , y , and z directions, respectively. Point O is the origin that has the coordinate $(0,0,0)$, and plane α is the plane parallel to the (hkl) plane and passing through the origin. An atom locates at point A has the coordinate (x_A, y_A, z_A) , and plane β is the plane parallel to the (hkl) plane and passing through point A . Here we derive the contribution of atom A to the diffraction pattern for the (hkl) reflection.

The position of atom A is specified by its fraction coordinate $u=x_A/a$, $v=y_A/b$, and $w=z_A/c$. We can define the position vector \vec{r} for atom A

$$\vec{r} = u\vec{a} + v\vec{b} + w\vec{c} \quad (2.8)$$

and the wave vectors of the incident and reflected beam in Fig. 2.6 are \vec{K}_i and \vec{K}_d , respectively. The magnitude of both wave vectors is $2\pi/\lambda$. The wave vector transfer \vec{K} which equals the vectors (h, k, l) in the reciprocal space that represents the diffraction planes can be described as

$$\vec{K} = \vec{K}_d - \vec{K}_i = h\vec{a}^* + kb^* + l\vec{c}^* \quad (2.9)$$

where \vec{a}^* , \vec{b}^* , and \vec{c}^* are the primitive vectors in reciprocal space.

$$\vec{a}^* = \frac{2\pi}{a}\vec{x}, \vec{b}^* = \frac{2\pi}{b}\vec{y}, \vec{c}^* = \frac{2\pi}{c}\vec{z} \quad (2.10)$$

When the Bragg's law is satisfied for the reflection, the path difference between ray 2' and ray 1' is

$$\delta_{2'1'} = MCN = 2d_{hkl}\sin\theta = \lambda \quad (2.11)$$

From the definition of Miller indices, the distance between (hkl) planes is

$$d_{hkl} = \frac{1}{\sqrt{\frac{h^2}{a^2} + \frac{k^2}{b^2} + \frac{l^2}{c^2}}} \quad (2.12)$$

Atom A locates at (x_A, y_A, z_A) and has a distance d_A to plane α . So, the path difference between ray 3' and ray 1' is

$$\delta_{3'1'} = RAS = \frac{OA}{OC}\lambda = \frac{d_A}{d_{hkl}}\lambda \quad (2.13)$$

d_A can be calculated with the position vector \vec{r} and the wave vector transfer \vec{K} ,

$$d_A = \frac{\vec{r}\vec{K}}{|\vec{K}|} = \frac{hu\vec{a} \cdot \vec{a}^* + kv\vec{b} \cdot \vec{b}^* + lw\vec{c} \cdot \vec{c}^*}{\sqrt{\frac{(2\pi h)^2}{a^2} + \frac{(2\pi k)^2}{b^2} + \frac{(2\pi l)^2}{c^2}}} = \frac{hu + kv + lw}{\sqrt{\frac{h^2}{a^2} + \frac{k^2}{b^2} + \frac{l^2}{c^2}}} \quad (2.14)$$

Substitute Eq. (2.14) and Eq. (2.12) into Eq. (2.13) gives

$$\delta_{3'1'} = (hu + kv + lw)\lambda \quad (2.15)$$

then the phase difference between ray 3' and ray 1' in radians is given by

$$\phi = \frac{\delta_{3'1'}}{\lambda} 2\pi = 2\pi(hu + kv + lw) \quad (2.16)$$

With Eq. (2.8) and Eq. (2.9), the phase difference from Eq. (2.16) can be written as

$$\phi = \vec{K} \cdot \vec{r} \quad (2.17)$$

Atom A contributes to the diffraction pattern in terms of planes with wave vector transfer \vec{K} by

$$f_A e^{i\phi} = f_A e^{i\vec{K} \cdot \vec{r}} \quad (2.18)$$

Where f_A is a constant related to the type of atom and the type of diffraction (neutron or X-ray). Eq. (2.18) represents the contribution of the intensity of atom A on the plane (hkl) in an orthorhombic structure. However, Eq. (2.18) is also true in other structures that are not orthorhombic. \vec{r} is the real space position of the atom and \vec{K} is the reciprocal space vector of the beam, the magnitude of \vec{r} and \vec{K} remains the same for any coordinate system, nor does the angle between \vec{r} and \vec{K} change in a different coordinate system. So, $\vec{K} \cdot \vec{r} = |K||r|\cos\theta$ (θ is the angle between \vec{r} and \vec{K}) does not change in any coordinate system.

The overall contribution to the planes with wave vector transfer \vec{K} is the sum of all waves scattered by the individual atoms in the unit cell

$$F_{hkl} = \sum_i f_i e^{i\vec{K} \cdot \vec{r}_i} \quad (2.19)$$

Eq. (2.19) is called the structure factor for the hkl reflection, and it is valid for any space group

2.3 Intensity Analysis from Neutron Powder Diffraction

Neutrons can exhibit wave phenomena like all quantum particles, diffraction is one of these phenomena. Neutron diffraction, also named as neutron elastic scattering, is an application to determine the atomic and magnetic structure of a material. The advantages of neutron diffraction include its high penetration depth and high sensitivity to light atoms.[7]

Nuclear scattering in neutron diffraction can get information about crystal structure of a material. Neutron diffraction follows Bragg's law that is the same with X-ray diffraction. Neutrons interact directly with the nucleus of the atom, and the contribution to the diffracted intensity depends on each isotope, so, light (low Z) atoms contribute strongly to the diffracted intensity, even in the presence of large Z atoms.[8] The scattering length varies from isotope to isotope rather than linearly with the atomic number.

Magnetic scattering in neutron diffraction can get information about magnetic ordering of a material.[9] Although the net charge of neutron is zero, it carries a magnetic moment, and therefore interacts with magnetic moments by dipole-dipole interactions. As a result, the diffraction intensity of magnetic part is related to the shape of electron cloud and the incident angle, this factor is called magnetic form factor (f'_i in Eq. (2.22)) in magnetic scattering of neutron diffraction.

If the neutron beam is not polarized, it is called unpolarized neutron. If the neutron beam is polarized that the diffraction only occurs for a specific vertical spin-polarization direction, it is called polarized neutron.[10] DEMAND can produce both unpolarized and polarized neutron beam, while POWGEN can only generate unpolarized neutron beam. [4]

Neutron diffraction can be used to trace the magnitude and direction of the magnetization after carefully separating the magnetic signal from the nuclear signal. The nuclear (n) and magnetic (m) parts of the powder neutron diffraction are

$$I_n = ABF_n^2 e^{-2W(T)} \quad (2.20)$$

and

$$I_m = ABF_m^2 e^{-2W(T)} \quad (2.21)$$

where A is a common constant factor and B is the multiplicity that depends on the diffracting plane indicated by (h, k, l) . The Debye-Waller factor $e^{-2W(T)}$ takes into account the effect of thermal fluctuation of atomic positions on the diffraction, where $W(T)$ increases with temperature.[11] F_n and F_m are the structure factors for the nuclear and magnetic parts, respectively.

2.3.1 Debye-Waller Factor of Neutron Powder Diffraction

To evaluate the nuclear contribution to the diffraction intensity, we have exploited that the temperature dependence of I_n comes from the Debye-Waller factor $e^{-2W(T)}$, The Debye-Waller factor is used to describe the attenuation of x-ray scattering or coherent neutron scattering caused by thermal motion.[12,13] It has also been called the B factor or the temperature factor. So long as there is no structural transition at high temperature (above Curie temperature T_c), we first estimated the Curie temperature T_c using the temperature-dependent magnetometry based on $W(T) = \beta T/(4d^2)$.[11] Two methods can estimate β -values. First method is fitting the intensity above T_c for different d-spacing at the same temperature. The intensity above T_c does not contain magnetic scattering, the

difference between theoretical intensity and the experimental value should result from Debye-Waller only. We can use the theoretical and the experimental peak intensity of different d-spacing at the same temperature to fit β value.

The other method is fitting the intensity above T_c for different temperatures of the same peak (same d-spacing). We can use the theoretical and the experimental intensity of the same peak at different temperature to fit β value.

The nuclear contribution can then be obtained from $I_n = I_n(T_1) \exp[-2W(T) + 2W(T_1)]$ and subtracted, where T_1 is a reference temperature.

2.3.2 Magnetic Moment for Ferromagnetic Material from Neutron

Powder Diffraction

In the nuclear part in Eq. (2.20), $F_n = \sum_i [f_i \exp(i\vec{K} \cdot \vec{r}_i)]$ is the crystal structure factor, and i is the index of atoms in the unit cell of the crystal structure. The position of the i -th atom in the unit cell is denoted by \vec{r}_i ; f_i is the neutron coherent scattering lengths of the elements; [14] \vec{K} is the neutron wave vector transfer which equals the vectors (h, k, l) in the reciprocal space that represents the diffraction planes.

For the magnetic part, if the magnetic structure in every unit cell is the same, one has [9,15]

$$F_m^2 = \frac{1}{2} (\gamma r_0 g)^2 \sum_{\alpha, \beta} \left(\delta_{\alpha\beta} - \frac{K_\alpha K_\beta}{K^2} \right) \sum_{i, j} f_i'(\vec{K}) f_j'(\vec{K}) e^{i\vec{K} \cdot (\vec{r}_i - \vec{r}_j)} S_{i\alpha} S_{j\beta} \quad (2.22)$$

Here $\alpha, \beta \in \{x, y, z\}$, $\delta_{\alpha\beta}$ is the unity matrix (Kronecker symbol), K_α is the projection of

\vec{K} along the α -direction, $S_{i\alpha}$ is the projection of the spin \vec{S}_i of the i -th atom onto the α -direction, $f'_i(\vec{K})$ is the magnetic form factor, which depends on the type of the magnetic atom.[16] For the Landé factor we assume $g = 2$ for $3d$ transition metal, $\gamma = 1.913$, and $r_0 = 2.818 \cdot 10^{-15}$ m is the classical electron radius.

In the case of ferromagnetism (all spins in one unit cell are aligned along the same axis), we can carry out a quantitative discussion where Eq. (2.22) simplifies to

$$I_m = \frac{1}{2} A (\gamma r_0 g)^2 e^{-2W(T)} B(\vec{K}) \left| \sum_i [f'_i(\vec{K}) e^{i\vec{K} \cdot \vec{r}_i}] \right|^2 S^2 Q^2(\vec{K}) \quad (2.23)$$

Here $Q^2(\vec{K}) = 1 - [\vec{S} \cdot \vec{K} / (SK)]^2$ and S is the average spin per atom.

Next, we analyze the magnitude S^2 . From Eq. (2.23) and Eq. (2.20), the ratio between the magnetic contribution and the nuclear contribution is

$$\frac{I_m}{I_n} = \frac{(\gamma r_0 g)^2 \left| \sum_i [f'_i(\vec{K}) e^{i\vec{K} \cdot \vec{r}_i}] \right|^2 S^2 Q^2(\vec{K})}{2 \left| \sum_i [f_i e^{i\vec{K} \cdot \vec{r}_i}] \right|^2} \quad (2.24)$$

$Q^2(\vec{K})$ can be calculated with $\sum_{i=\alpha,\beta,\gamma} \sin^2 \theta_i = 2$, where θ_α , θ_β , and θ_γ are the angle between the magnetic moment and the a, b , and c axis of the unit cell (an example is provided in chapter 3), S^2 is the only unknown variable.

2.3.3 Magnetic Moment for Complex Spin Structure from Neutron

Powder Diffraction

Neutron diffraction probes the arrangement of spins or spin texture. The spin structure extraction hinges on the magnetic diffraction intensity (magnetic contribution)

analysis from the coherent scattering of the spins. The intensity of the magnetic contribution can be expressed as

$$F_m^2(\vec{k}) = \frac{1}{2}(\gamma r_0 g)^2 \left| \sum_{\vec{r}} \vec{q}(\vec{k}, \vec{r}) f'(\vec{k}, \vec{r}) \exp(i\vec{k} \cdot \vec{r}) \right|^2 \quad (2.25)$$

with

$$\vec{q}(\vec{k}, \vec{r}) \equiv \vec{s}(\vec{r}) - \hat{k}[\hat{k} \cdot \vec{s}(\vec{r})]. \quad (2.26)$$

Here, \vec{r} is the position of a magnetic atomic site with spin $\vec{s}(\vec{r})$; $\hat{k} = \vec{k}/|\vec{k}|$ is the unit vector of \vec{k} , $f'(\vec{k}, \vec{r})$ is the isotope-specific form factor for each site, $\gamma = 1.913$, $r_0 = 2.818 \times 10^{-15}$ m is the classical electron radius, and $g \approx 2$ is the Landé factor.

Eq. (2.25) is a more general case for Eq. (2.23) since Eq (2.25) does not require the spin structure to be ferromagnetic. In a ferromagnetic structure $\vec{q}(\vec{k}, \vec{r})$ is the same for all atoms, which can be taken out from Eq. (2.25)

$$\begin{aligned} |\vec{q}(\vec{k}, \vec{r})|^2 &= |\vec{s} - \hat{k}[\hat{k} \cdot \vec{s}]|^2 = \vec{s}^2 - 2\vec{s} \cdot \hat{k}[\hat{k} \cdot \vec{s}] + (\hat{k}[\hat{k} \cdot \vec{s}])^2 \\ &= \vec{s}^2 - 2(\hat{k} \cdot \vec{s})^2 + (\hat{k} \cdot \vec{s})^2 = \vec{s}^2 - (\hat{k} \cdot \vec{s})^2 = \vec{s}^2 \left[1 - \left(\frac{\vec{s} \cdot \vec{k}}{|\vec{s}||\vec{k}|} \right)^2 \right] \end{aligned} \quad (2.27)$$

Which is the form of Eq. (2.23)

Multiple magnetic atomic sites within the unit cell can be described by defining $\vec{r} = \vec{R} + \vec{u}$ with the lattice point vector \vec{R} and the relative position \vec{u} of an atomic site in the unit cell. The form factor $f'(\vec{k}, \vec{r})$ depends on atomic (and isotopic) species and \vec{k} , but not on the lattice points, which implies $f'(\vec{k}, \vec{r}) = f'(\vec{k}, \vec{u})$. A spin texture, such as a helical

structure, with a propagation vector \vec{k}_s , can be considered by writing $\vec{s}(\vec{r}) = \vec{s}_0(\vec{u})e^{-i\vec{k}_s \cdot \vec{R}}$ and $\vec{q}(\vec{k}, \vec{r}) = \vec{q}_0(\vec{k}, \vec{u})e^{-i\vec{k}_s \cdot \vec{R}}$, yielding

$$\sum_{\vec{r}} \vec{q}(\vec{k}, \vec{r}) f'(\vec{k}, \vec{r}) e^{i\vec{k} \cdot \vec{r}} = \sum_{\vec{u}} \vec{q}_0(\vec{k}, \vec{u}) f'(\vec{k}, \vec{u}) e^{i\vec{k} \cdot \vec{u}} \sum_{\vec{R}} e^{i(\vec{k}_s + \vec{k}) \cdot \vec{R}} \quad (2.28)$$

The factor $\sum_{\vec{R}} e^{i(\vec{k}_s + \vec{k}) \cdot \vec{R}}$ determines the diffraction angle where the intensity peaks appear. The factor $\vec{f}'_s(\vec{k}) \equiv \sum_{\vec{u}} \vec{q}_0(\vec{k}, \vec{u}) f'(\vec{k}, \vec{u}) e^{i\vec{k} \cdot \vec{u}}$ can be treated as the vector structure factor for magnetic scattering. Eq. (2.25) and (2.28) can be used to simulate the magnetic contribution to the diffraction intensity according to the spin arrangement $\vec{s}(\vec{r}) = \vec{s}_0(\vec{u})e^{-i\vec{k}_s \cdot \vec{R}}$. The example is discussed in chapter 4.

References

- [1] Arc Melter | Nanomaterials & Thin Films Facility (URL: <https://ncmn.unl.edu/thinfilm/arc-melter>)
- [2] Melt Spinner SC | Nanomaterials & Thin Films Facility (URL: <https://ncmn.unl.edu/thinfilm/melt-spinner-sc>)
- [3] Sharma J, Suresh K G, Raja M M and Walke P 2020 Martensitic Transition, Magnetic, Microstructural and Exchange Bias Properties of Melt Spun Ribbons of Mn-Ni-Sn Shape Memory Heusler Alloy *Front. Mater.* **7**
- [4] Dimensional Extreme Magnetic Neutron Diffractometer | Neutron Science at ORNL (URL: <https://neutrons.ornl.gov/demand>)
- [5] Powder Diffractometer | Neutron Science at ORNL (URL: <https://neutrons.ornl.gov/powgen>)
- [6] Cullity Stock, Stuart R., Pearson India Education Services., B D 2015 *Elements of*

X-ray diffraction (Miejsce nieznane: Pearson India Education Services)

- [7] Anon 2005 *Measurement of Residual Stress in Materials Using Neutrons* (Vienna: INTERNATIONAL ATOMIC ENERGY AGENCY)
- [8] Combet, Sophie 2020 An introduction to neutrons for biology *EPJ Web Conf.* **236** 1001
- [9] Roberts B W 1956 Neutron Diffraction Study of the Structures and Magnetic Properties of Manganese Bismuthide *Phys. Rev.* **104** 607–16
- [10] Ressouche, E. 2014 Polarized neutron diffraction *JDN* **13** 2002
- [11] Xu X, Zhang X, Yin Y, Balasubramanian B, Das B, Liu Y, Huq A and Sellmyer D J 2017 Anti-site mixing and magnetic properties of $\text{Fe}_3\text{Co}_3\text{Nb}_2$ studied via neutron powder diffraction *J. Phys. D. Appl. Phys.* **50** 25002
- [12] Debye P 1913 Interferenz von Röntgenstrahlen und Wärmebewegung *Ann. Phys.* **348** 49–92
- [13] Waller I 1923 Zur Frage der Einwirkung der Wärmebewegung auf die Interferenz von Röntgenstrahlen *Zeitschrift für Phys.* **17** 398–408
- [14] Sears V F 1992 Neutron scattering lengths and cross sections *Neutron News* **3** 26–37
- [15] Squires G L 2013 Introduction to the theory of thermal neutron scattering
- [16] Prince International Union of Crystallography., E 2011 *International tables for crystallography. Volume C, Volume C*, (Chichester: J. Wiley & Sons for the International union of crystallography)

Chapter III: Noncollinear Spin Structure in $\text{Fe}_{3+x}\text{Co}_{3-x}\text{Ti}_2$ ($x = 0, 2, 3$) from Neutron Diffraction

3.1 Introduction

Permanent-magnet material free of rare earth and other expensive elements is a technologically important research topic because innovative technologies such as electric cars, wind generators, and medical resonance-imaging work are energy-efficient and easy to operate when using permanent magnets.[1–6] Most top-performing permanent magnets are made from rare-earth transition-metal metal intermetallics such as Nd-Fe-B and Sm-Co,[7–9] but supply-chain concerns and raw materials prices call for replacement options for these often bulky magnets.

The energy product is the key figure of merit for permanent magnets, which describes the magnetostatic energy stored in free space. High-energy-product permanent magnets require high magnetizations, high Curie temperatures, and high magnetocrystalline anisotropies.[2,10] Iron and cobalt have very high Curie temperature and magnetizations, Fe being preferred due to its lower raw-materials price. However, the anisotropies of Fe and Co-based magnets, such as steel magnets, are moderate at best. First, magnetocrystalline anisotropy requires spin-orbit coupling, which is strongest for heavy elements. Second, the atomic environments in the 3d elements are cubic (bcc Fe, fcc Co) or nearly cubic (hcp Co). Adding small amounts of rare earth elements, for example, through nanostructuring[11–13], is one option, but such structures are extremely difficult and expensive to produce.

Another option is to search for new permanent magnets entirely based on Fe-series (3d) transition-metal elements.[14–20] Some structures are structurally highly anisotropic, for example, orthorhombic HfCo_7 and the rhombohedral $\text{Zr}_2\text{Co}_{11}$,[21] and there is hope that this structural anisotropy turns into magnetic anisotropy, despite the relatively small spin-orbit coupling. A key challenge is that the addition of elements from the first half and the middle of the 3d series (Ti, Cr, Mn) tends to reduce magnetization and Curie temperature. Exploring the full range of ternary and quaternary transition-metal alloys is an important task. Examples of unexpected 'hot spots' in phase diagrams are $\text{Nd}_2\text{Fe}_{14}\text{B}$ [2] and, more recently, partially ordered Mn-Fe-Co.[16]

Our focus is on the recently discovered alloy $\text{Fe}_{3+x}\text{Co}_{3-x}\text{Ti}_2$, whose hexagonal crystal structure has recently been shown to support uniaxial anisotropies of the order of $K_1 = 1 \text{ MJ/m}^3$ ($1 \times 10^7 \text{ erg/cm}^3$)[22–24]. Emphasis is on the magnetic anisotropy as a function of the Co content. The dependence of the first uniaxial magnetic anisotropy constant on the number of d electrons tends to be highly nonlinear and needs separate consideration for each alloy system. Substitution of Co by Fe is also interesting from the viewpoint of raw-materials price.

The basics of the micromagnetism of polycrystalline magnets are well-established from the viewpoints of both general magnetism[25] and neutron experiments[26–28]. A particular feature is that easy-plane and easy-axis magnetisms are difficult to distinguish in nanocrystalline magnets, both yielding substantial coercivity[29]. Density-functional calculations indicate that rapidly-quenched $\text{Fe}_{3+x}\text{Co}_{3-x}\text{Ti}_2$ exhibits competing for anisotropies on an atomic scale caused by Fe-Co site disorder.[22–24] The effect of this disorder and the spin structure of $\text{Fe}_{3+x}\text{Co}_{3-x}\text{Ti}_2$ are poorly understood, especially from

an experimental viewpoint. Questions include the possible occurrence of easy-cone magnetism[4,10,30] and how atomic-scale easy-plane contributions caused by random-anisotropy disorder[25,31–33] affect the spin structure. In this chapter, we use temperature-dependent neutron powder diffraction (NPD)[34–40] to investigate the spin structure (magnitude and direction of the atomic magnetic moments) in $\text{Fe}_{3+x}\text{Co}_{3-x}\text{Ti}_2$ ($x = 0, 2, \text{ and } 3$).

3.2 Experimental method

Neutrons have long been used to investigate the spin structure of permanent magnets. Spin-polarized neutron experiments were used to investigate $R_2\text{Fe}_{14}\text{B}$ magnets, leading to the clarification of its spin structure and the observation of low-temperature easy-cone magnetism in $\text{Nd}_2\text{Fe}_{14}\text{B}$. [9,30,41,42] However, $\text{Fe}_{3+x}\text{Co}_{3-x}\text{Ti}_2$ is a nonequilibrium compound and, therefore, difficult to obtain in single-crystal form. Polycrystalline magnets, including $\text{Nd}_2\text{Fe}_{14}\text{B}$, have been investigated by small-angle neutron scattering (SANS), with emphasis on micromagnetic length scales[26–28], these measurements are cumbersome to perform over a wide temperature range and yield limited information about the spin structure. This chapter uses neutron diffraction over the whole angle and temperature range. In particular, the neutron-diffraction selection rules make it possible to determine the alignment between the magnetic moments and the crystalline orientations even in polycrystalline samples.

To produce the sample, we have used a melt-spinning method explained elsewhere.[21] The melt-spun ribbons, which have the compositions $\text{Fe}_{3+x}\text{Co}_{3-x}\text{Ti}_2$ ($x = 0, 2, 3$), were mechanically ground to obtain powders suitable for structural and magnetic

characterization. The high-resolution neutron powder diffraction measurements were carried out between 100 and 600 K without a magnetic field using pulsed neutron beams at the beamline POWGEN in the Spallation Neutron Source at the Oak Ridge National Laboratory. The sample masses for the neutron diffraction measurements are 4.46 g ($\text{Fe}_3\text{Co}_3\text{Ti}_2$), 3.41 g (Fe_5CoTi_2), and 4.27 g (Fe_6Ti_2), as shown in **Table 3.1**. The diffraction spectra were analyzed using the Rietveld method[43] with the FullProf program.[44] The bulk magnetization measurements were carried out using a superconducting quantum interference device (SQUID) magnetometer and a physical property measurement system (PPMS).

Sample (unit)	$\text{Fe}_3\text{Co}_3\text{Ti}_2$	Fe_5CoTi_2	Fe_6Ti_2
Mass (g)	4.46	3.41	4.27
Particle size (nm)	44±1	44±1	39±2
Thermal expansion coefficient (10^{-6} K^{-1})	8.9	8.6	7.9
T_C (K)	586		513
Magnetic moment per unit cell (μ_B)	23±4	25±3	26±2

Table 3.1: Properties of the three samples studied in this work.

3.3 Result and Discussion

In this section, we present and analyze the results of the neutron diffraction experiments. Structurally, we focus on the lattice constants as functions of composition x and temperature T , and the grain-size determination from the width of the diffraction peaks. The magnetic contribution to the neutron diffraction is used to extract the magnitude of the magnetization and its direction with respect to the local c -axis.

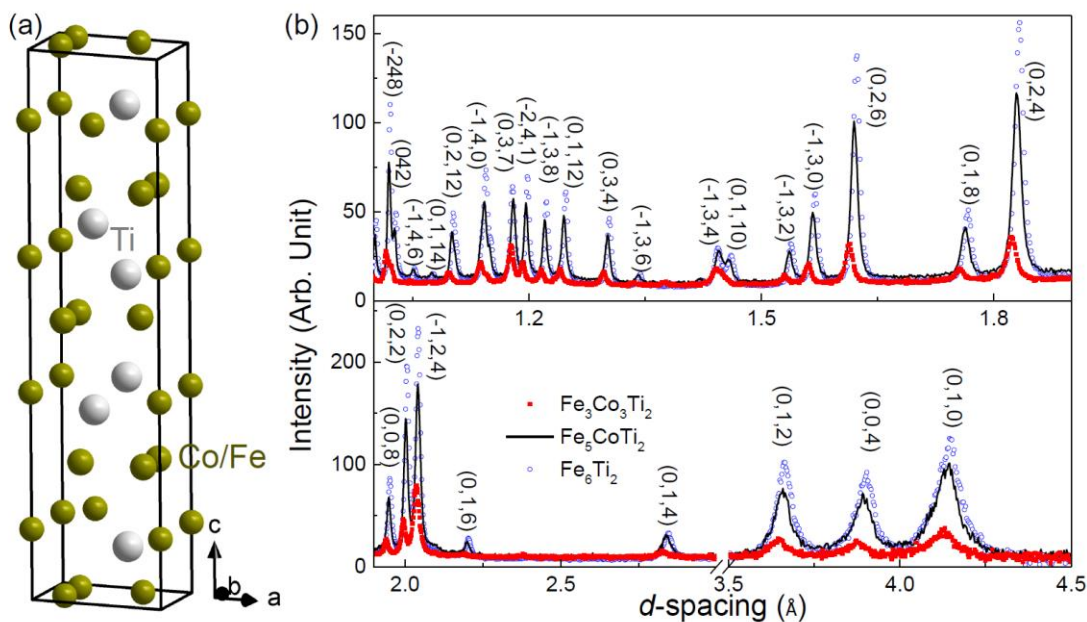


Figure 3.1: Crystal structure and neutron diffraction patterns: (a) unit cell of hexagonal $\text{Fe}_{3+x}\text{Co}_{3-x}\text{Ti}_2$ and (b) neutron powder diffraction spectra for different compositions, measured at 600 K and scaled by incident neutron counts and sample mass.

3.3.1 Crystallographic Structure

The $\text{Fe}_{3+x}\text{Co}_{3-x}\text{Ti}_2$ alloys crystallize in the hexagonal structure of **Fig. 3.1(a)**, which has the space group $P\bar{6}m2$ (point group C_{3h}). **Fig. 3.1(b)** shows the 600 K diffraction intensities of $\text{Fe}_{3+x}\text{Co}_{3-x}\text{Ti}_2$ ($x = 0, 2, 3$) as a function of the spacing d of the lattice planes. The intensities are scaled by the sample mass and the charge deposited by the proton beam on the liquid mercury target. The diffraction spectra are consistent with the hexagonal structure of polycrystalline $\text{Fe}_{3+x}\text{Co}_{3-x}\text{Ti}_2$; [22] the Miller indices (h, k, l) of selected peaks are marked accordingly. The significant differences between the diffraction intensities of the samples are due to the significant difference between the neutron coherent scattering length of Co and Fe. [45]

The powder samples consist of randomly oriented grains whose size D can be estimated from the widths of the diffraction peaks—provided that the instrument broadening is much smaller than the peak width of the nanograins, $D \approx 2d^2/\Delta d$, [23] where Δd is the peak's full width at half maximum. **Fig. 3.2(a)** shows the temperature dependence of the grain size D . Using the well-separated peaks (014), (024), (018), (026), and (034), we obtained grain sizes of about 44 nm for Fe_6Ti_2 and Fe_5CoTi_2 , whereas the grain size of the $\text{Fe}_3\text{Co}_3\text{Ti}_2$ sample is around 39 nm. The corresponding errors of 1-2 nm (**Table 3.1**) were calculated from the dispersion of the results of different peaks. The grain sizes do not exhibit any obvious temperature dependence, suggesting that the microstructures are stable over the temperature range of the measurements.

Fig. 3.2(b), the lattice constants and their temperature dependences were obtained by fitting the diffraction spectra with the Rietveld method implemented in the software FullProf. [44,46] The lattice constants of $\text{Fe}_{3+x}\text{Co}_{3-x}\text{Ti}_2$ increase with x , which is consistent

with Fe's smaller effective nuclear charge than Co. For each compound, the temperature dependences of the lattice constants a and c are similar. For $\text{Fe}_3\text{Co}_3\text{Ti}_2$ and Fe_5CoTi_2 , the thermal expansion appears to be linear in the range of 100 to 600 K, while for Fe_6Ti_2 , the thermal expansion is linear only above 300 K, indicating that Fe_6Ti_2 may have a substantially higher Debye temperature. The linear thermal expansion coefficients between 300 and 600 K are about $8 \cdot 10^{-6}/\text{K}$ in both the a and c directions (**Table 3.1**). These values are smaller than those for Co and Fe, $13 \cdot 10^{-6}/\text{K}$ and $11.8 \cdot 10^{-6}/\text{K}$, respectively, but close to that of Ti, $8.6 \cdot 10^{-6}/\text{K}$. [47]

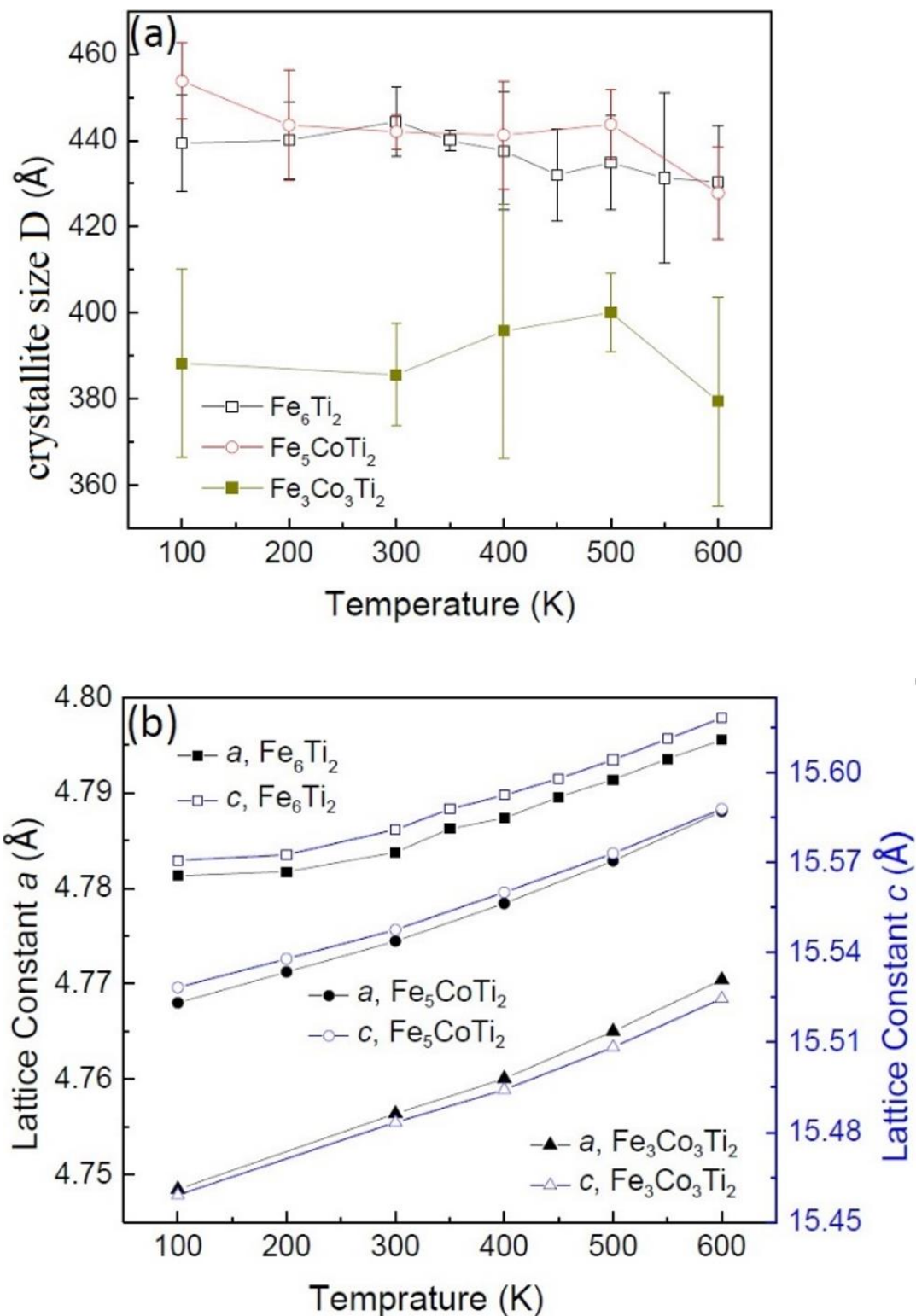


Figure 3.2: Temperature dependence of crystallographic properties: (a) particle size calculated from the diffraction peak widths and (b) lattice constants.

3.3.2 Separation of Magnetic and Nuclear Contributions

To extract the magnetic contribution, we first estimated the Curie temperature T_c using the temperature-dependent magnetometry during heating in a field of 1 kOe, as shown in **Fig. 3.3(a)**. The T_c extracted using linear extrapolation is shown in **Table 3.1**. Therefore, the neutron spectra above 500 K contain only minimal magnetic contribution, as also shown in **Fig. 3.3(b-d)**.

To evaluate the nuclear contribution to the diffraction intensity, we have exploited that the temperature dependence of I_n comes from the Debye-Waller factor $e^{-2W(T)}$, so long as there is no structural transition at high temperature. Based on $W(T) = \beta T/(4d^2)$, [23] the diffraction intensity above 500 K yields β -values of 2.5, 2.0, and $12.0 \cdot 10^{-4} \text{ \AA}^2/\text{K}$ for Fe_6Ti_2 , Fe_5CoTi_2 , and $\text{Fe}_3\text{Co}_3\text{Ti}_2$, respectively. The nuclear contribution can then be obtained from $I_n = I_n(T_1) \exp[-2W(T) + 2W(T_1)]$ and subtracted, where T_1 is a reference temperature.

Fig. 3.3(a-c) shows the integrated intensities of the magnetic part for the (008) and (010) peaks. All peak intensities in **Fig. 3.3(a-c)** decrease with increasing temperature, as expected from the temperature dependence of the magnetization. In **Fig. 3.3(b-d)**, the (008) intensities are much smaller than the (010) intensities. Magnetic neutron diffraction detects mainly the part of magnetic moment perpendicular to the neutron wave vector transfer \vec{K} , so that the less intense (008) diffraction suggests that the magnetic moment is nearly parallel to the c axis.

From **Chapter 2.3.2**, the ratio between the magnetic contribution and the nuclear contribution is

$$\frac{I_m}{I_n} = \frac{(\gamma r_0 g)^2 \left| \sum_i [f'_i(\vec{K}) e^{i\vec{K} \cdot \vec{r}_i}] \right|^2 S^2 Q^2(\vec{K})}{2 \left| \sum_i [f_i e^{i\vec{K} \cdot \vec{r}_i}] \right|^2} \quad (3.1)$$

Where $Q^2(\vec{K}) = 1 - [\vec{S} \cdot \vec{K} / (SK)]^2$ and S is the average spin per atom

First, we analyze $Q^2(\vec{K})$. Since $e^{i\vec{K} \cdot \vec{r}_i}$, and $f'_i(\vec{K})$ depend on the atomic structure only, and one can calculate the product $S^2 Q^2(\vec{K})$ from the magnetic contribution in **Fig. 3.3**. Introducing the angle θ between the magnetic moment and the \vec{K} vector, $Q^2(\vec{K}) = \sin^2 \theta$. The angles between a certain vector and three orthogonal coordinates in space satisfy $\sum_{i=\alpha,\beta,\gamma} \sin^2 \theta_i = 2$. Since the vector (010) is perpendicular to the vector (008) and the vectors within the basal plane are equivalent due to the crystal symmetry, one has $2Q^2[(010)] + Q^2[(008)] = 2$. Using this relation, we obtained $Q^2[(010)]$ and $Q^2[(008)]$ for all three compounds. Furthermore, we calculated the average angle θ_c between the magnetization and the c axis at 100 K, which is displayed in **Fig. 3.4(a)**.

With $Q^2(\vec{K})$ being calculated, S^2 in Eq. (3.1) is the only unknown variable. This procedure yields the respective spin values $0.81 \pm 0.03 \mu_B/\text{magnetic atom}$, $0.64 \pm 0.06 \mu_B/\text{magnetic atom}$, and $0.61 \pm 0.06 \mu_B/\text{magnetic atom}$ for Fe_6Ti_2 , Fe_5CoTi_2 , and $\text{Fe}_3\text{Co}_3\text{Ti}_2$ at 100 K. The corresponding magnetic moments per unit cell are $29 \pm 1 \mu_B$, $23 \pm 2 \mu_B$, and $22 \pm 2 \mu_B$ for Fe_6Ti_2 , Fe_5CoTi_2 , and $\text{Fe}_3\text{Co}_3\text{Ti}_2$. These values are consistent with the saturation magnetizations previously [24] extracted from the magnetometry measurements at 10 K, **Fig. 3.4(b)**.

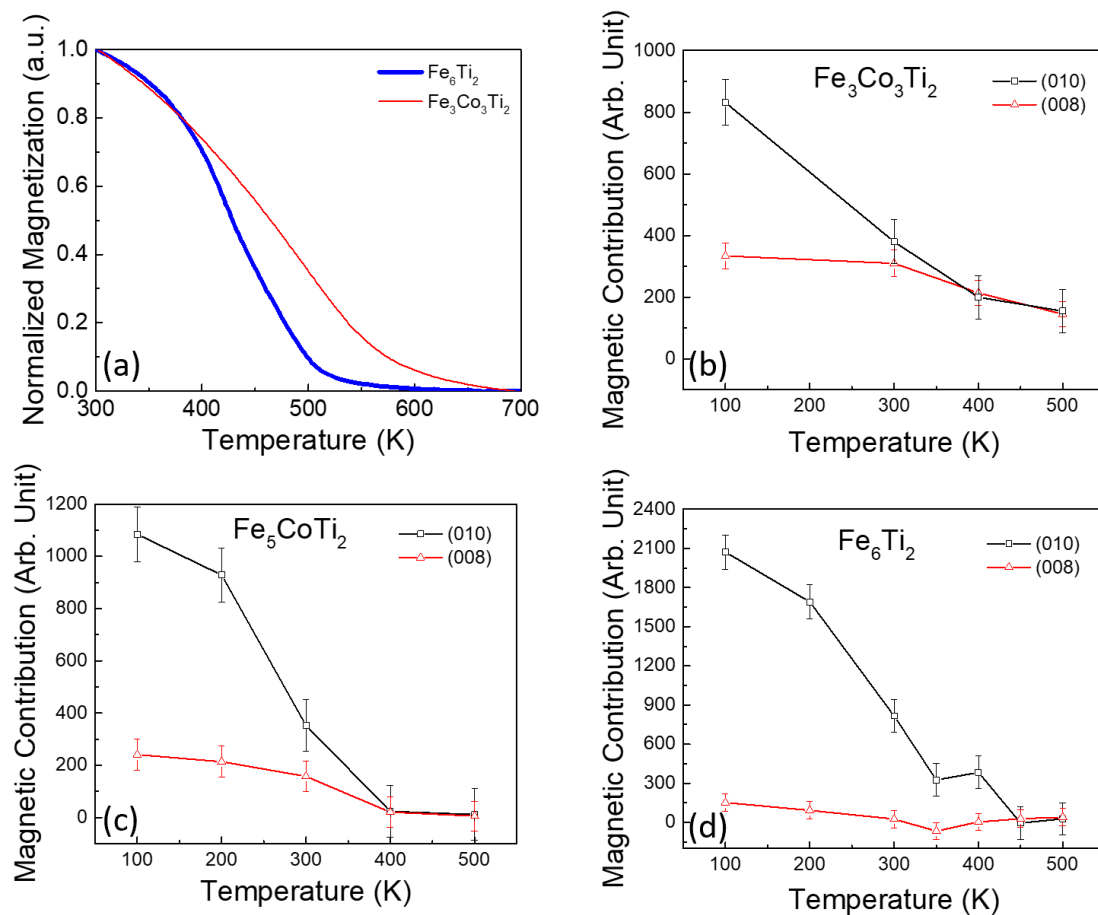


Figure 3.3: Temperature dependence of magnetization: (a) magnetic measurements during heating in a field of 1 kOe and (b-d) magnetic signal from neutron scattering.

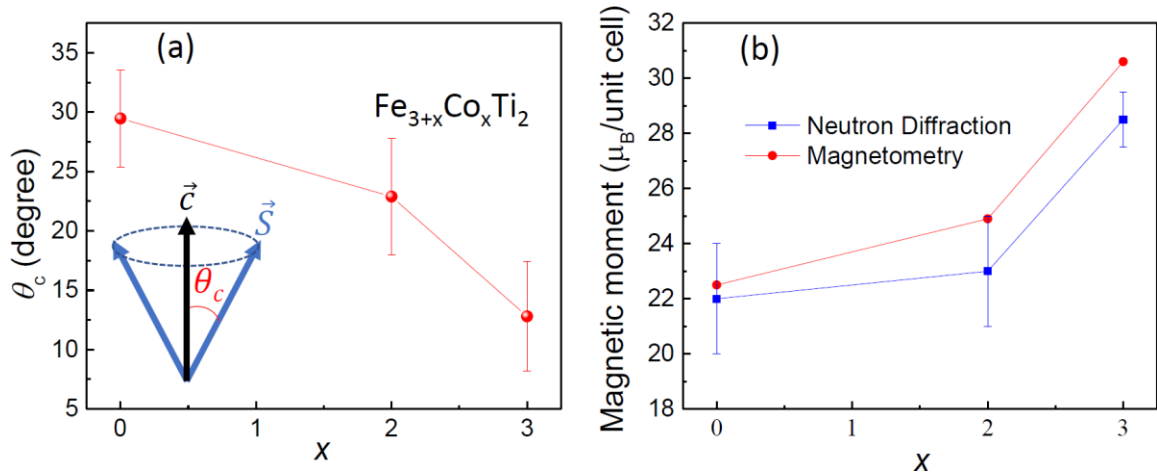


Figure 3.4: Dependence of magnetic moment on chemical composition x : (a) direction of the moment at 100 K (neutron experiment) and (b) magnitude of the moment at 10 K [24].

3.3.3 Micromagnetic Analysis

Figure 3.4(a) shows that the average misalignment angle θ_c increases with Co content. We explain this trend as a combined intrinsic and micromagnetic effect. Intrinsically, the substitution of Co for Fe creates a chemical disorder (site disorder), leading to a local anisotropy distribution. The corresponding random-anisotropy contribution will be shown in this subsection to enhance θ_c .

The present alloys crystallize in a hexagonal structure and therefore exhibit the magnetocrystalline anisotropy-energy density[25]

$$\eta = K_1 \sin^2\theta + K_2 \sin^4\theta + K_3 \sin^6\theta + K'_3 \sin^6\theta \cos\phi \quad (3.2)$$

Here K_1 , K_2 , and K_3 are the 2nd-, 4th-, and 6th-order uniaxial anisotropy constants, and K'_3 describes the 6th-order in-plane anisotropy of the crystals. The lower-order in-plane anisotropies K'_1 and K'_2 are zero in hexagonal crystals. By definition, magnetocrystalline

anisotropies are macroscopic, that is, averaged over several interatomic distances. Additional terms may exist on an atomic scale, for example, due to chemical disorder; they average to zero macroscopically but affect the anisotropy constants in Eq. (3.2).

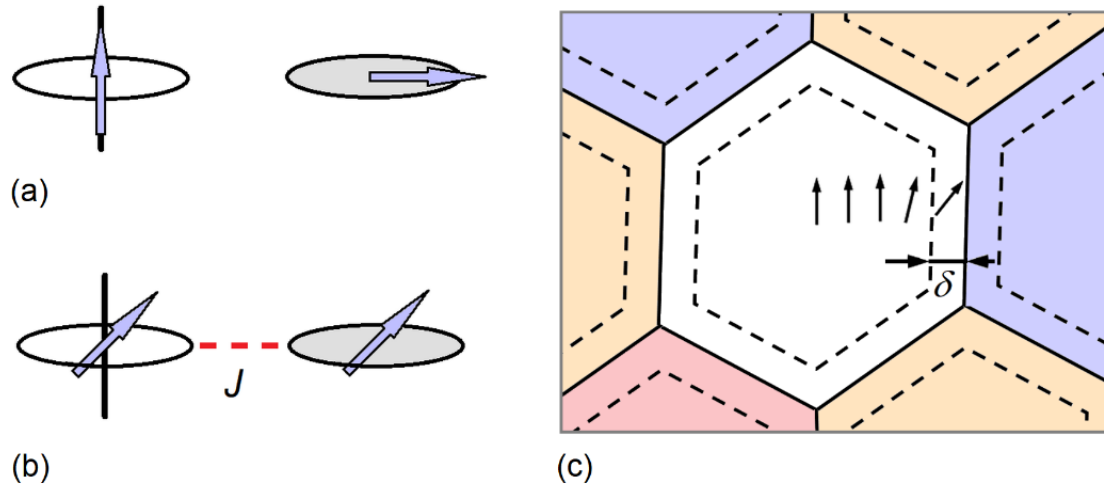


Figure 3.5: Spin directions in polycrystalline $\text{Fe}_{3+x}\text{Co}_{3-x}\text{Ti}_2$: (a-b) intrinsic (atomic-scale) effects and (c) extrinsic (nanoscale) effects. The thick lines in (a-b) show the c -axis, whereas the gray circles symbolize the a - b -plane. Hexagons in (c) represent grains. Published DFT anisotropy calculations[24] support the coexistence of easy-axis and easy-plane anisotropies (a-b). Spin structures (a) and (b) differ by the absence or presence of interatomic exchange, respectively; the physically realized case is (b).

Fig. 3.5 compares the intrinsic (atomic-scale) and extrinsic (nanoscale) mechanisms operative in $\text{Fe}_{3+x}\text{Co}_{3-x}\text{Ti}_2$. The important point is that Eq. (3.2) does not fix the local magnetization direction because anisotropy energies are typically much smaller than interatomic exchange. In the present case, the temperature equivalents of anisotropy and exchange energies are of the orders of 0.1 K and 500 K, respectively. Without exchange

coupling, the spin direction would be determined by the local environment and lie, for example, along the c -axis or in the a - b basal plane, as illustrated in **Fig. 3.5(a)**. However, the strong interatomic exchange means that neighboring spins are almost parallel[49], as in **Fig. 3.5(b)**. Inhomogeneous magnetization states become important on a nanoscale, especially near grain-boundaries separating grains of different c -axis orientations (c).

The 6th-order anisotropy constants K_3 and K_3' tend to be much smaller than K_1 and are normally neglected. K_2 can also be neglected in many cases, so the only surviving term is $K_1 \sin^2 \theta$. Depending on the sign of K_1 , the preferred magnetization direction is easy-axis ($\theta = 0$, $K_1 > 0$) or easy-plane ($\theta = \pi/2$, $K_1 < 0$). These two scenarios correspond to the left and right parts of **Fig. 3.5(a)**, respectively. However, great care is necessary when K_1 is accidentally zero due to competing anisotropy-energy contributions if the easy-axis and easy-plane contributions nearly cancel each other. Depending on the values of K_1 and K_2 , the spin structure may then be of the easy-cone type, where the macroscopic spin direction forms an angle θ_c with the c -axis[10,25,30]. Easy-cone magnetism leads to characteristic singularities in the hysteresis loop[30], but our previous magnetization measurements[20] do not show any sign of such singularities. We, therefore, neglect K_2 in the following analysis.

The average c -axis misalignment angle $\langle \theta \rangle_0$ between randomly oriented grains is 57.3° , and the change in spin direction is confined to a boundary region of thickness δ , **Fig. 3.5**. The misalignment angle decays approximately exponentially with the distance r from the interface and obeys $\Delta \theta(r) \sim \exp(-r/\delta_0)$, where $\delta_0 = (C/K_1)^{1/2}$ and C is a function of exchange energy.[25] The average angular deviation from the grains' c -axis is obtained by

integration over r and considering that the grain's surface area is approximately equal to $6\delta/D$. This procedure leads to

$$\langle \theta \rangle = \frac{3 \delta_0}{D} \langle \theta \rangle_0 \quad (3.3)$$

Taking $\delta = \delta_0 = 3$ nm,[25] calculated from K_1 and C , and $D = 40$ nm yields $\langle \theta \rangle = 13^\circ$. This estimate is in the right ballpark, but at the lower end of the experimental results, so the mechanism outlined in this paragraph partly explains the experimental data.

A substantially improved description is obtained by including the competition between atomic-scale easy-axis and easy-plane anisotropies. In an extreme scenario, $K_1 = 0$ yields $\delta = \infty$ and a strongly enhanced θ_c . However, δ is *de facto* limited by the grain size and by the nonzero residual coherent anisotropy $\langle K_1 \rangle$, so that $\langle \theta(x) \rangle$ does not diverge but reaches a finite maximum on Co addition.

For simplicity, we assume that a fraction $1 - p$ of all Fe/Co atoms has an easy-axis anisotropy of energy density $K_o \sin^2 \theta$, and the remaining fraction p has easy-plane anisotropy, $-K_p \sin^2 \theta$. Note that K_o and K_p are both positive in this definition. The parameter p reflects the chemical composition and may lead to a zero net anisotropy $\langle K_1 \rangle$ at some value x_c because the two anisotropy contributions have opposite signs. Straightforward anisotropy averaging yields

$$\langle K_1 \rangle = (1 - p) K_o - p K_p \quad (3.4a)$$

$$\text{and } \langle K_1^2 \rangle = (1 - p) K_o^2 + p K_p^2 \quad (3.4b)$$

Physically, atoms with easy-axis and easy-plane anisotropy are randomly distributed in each grain, which leads to partial anisotropy competition.

The anisotropy fluctuations are described by an energy δE obeying

$$\delta E^2 = \int \langle K_1(\vec{r}) K_1(\vec{r}') \rangle d\vec{r} d\vec{r}' \quad (3.5)$$

where the integration is over one grain. Assuming that the anisotropies of neighboring atoms are uncorrelated, we can write

$$\langle K_1(\vec{r}) K_1(\vec{r}') \rangle = V_o \delta(\vec{r} - \vec{r}') \langle K_1^2 \rangle \quad (3.6)$$

where V_o is the crystal volume per Fe/Co atom. Inserting Eq. (3.6) into Eq. (3.5) and performing the integration yields

$$\delta E^2 = V_o V_g \langle K_1^2 \rangle \quad (3.7)$$

Here V_g is the grain volume. The energy δE can be written in terms of a net anisotropy K_{eff} arising from the anisotropy fluctuations: $\delta E = K_{\text{eff}} V_g$. From random-anisotropy ferromagnetism, it is known that the micromagnetic behavior of such effective anisotropies is similar to that of $\langle K_1 \rangle$. For example, K_{eff} results in a decreasing of coercivity field in nanocrystalline soft magnets[33].

To determine δE , we need to evaluate $\langle K_1^2 \rangle$. Near x_c , we write $p = p_c + \gamma(x - x_c)$, where the parameter γ describes how the chemical changes create atomic-scale easy-plane anisotropies. Substitution of p into Eq. (3.4a-b) and taking into account that $\langle K_1(p_c) \rangle = 0$ yields

$$\langle K_1 \rangle = -\gamma(x - x_c) (K_o + K_p) \quad (3.8a)$$

and

$$\langle K_1^2 \rangle = K_o K_p + \gamma(x - x_c) (K_p^2 - K_o^2) \quad (3.8b)$$

At $x=x_c$, $\langle K_1 \rangle$ vanishes but $\langle K_1^2 \rangle = K_o K_p$, which is nonzero.

Combining Eqs. (3.8b) and (3.7) yields $\delta E^2 = V_o V_g [K_o K_p + \gamma(x - x_c)(K_p^2 - K_o^2)]$

and

$$K_{\text{eff}} = \sqrt{\frac{V_o}{V_g} [K_o K_p + \gamma(x - x_c)(K_p^2 - K_o^2)]} \quad (3.9)$$

The magnitudes of the involved atomic anisotropies are all comparable magnitude, so we can assume $K_o = K_p = K_1 \approx 1 \text{ MJ/m}^3$ and obtain the estimated $K_{\text{eff}} = (V_o/V_g)^{1/2} K_1$ for $x=x_c$. V_o/V_g leads to a grain-size-dependent reduction of the effective anisotropy, similar to the situation in other random-anisotropy magnets. Via $\delta_{\text{eff}} = (C/K_{\text{eff}})^{1/2}$, it yields an enhancement of the thickness δ_{eff} of the grain-boundary region and, according to Eq. (3.3), an increase in the misalignment angle $\langle \theta \rangle$.

For a quantitative estimate, we take into account that $V_o/V_g = (d_o/D)^3$, where $d_o \approx 0.29 \text{ nm}$ is the distance between neighboring Fe/Co atoms. This yields

$$\delta_{\text{eff}} = (D/d_o)^{3/4} \delta_o \quad (3.10)$$

Using $D = 40 \text{ nm}$ and Eq. (3.3) yields an enhancement of $\langle \theta \rangle$ by a factor of 40, much more than required to bridge the disagreement between Eq. (3.3) and the experimental results. The reason for the overestimation is the inaccurate assumption of a full-fledged competition between atomic easy-axis and easy-plane anisotropies, $\langle K_1 \rangle = 0$.

The power-law established by Eq. (3.10), $\delta_{\text{eff}} \sim D^{3/4}$ is remarkable because it means that the thickness of the magnetic boundary region ($\delta = \delta_{\text{eff}}$) increases nearly linearly with grain size. The physical expectation is that the atomic effects, such as competing for local anisotropies, vanish in the macroscopic limit. In fact, Eq. (3.10) predicts the average

misalignment angle $\langle\theta\rangle$ to decrease with grain size D , but only very weakly, scaling as $\delta_{\text{eff}}/D \sim 1/D^{1/4}$. For example, increasing the grain size from 40 nm to 1000 nm reduces $\langle\theta\rangle$ by a factor of only 2.2.

3.4 Summary

In summary, we have used neutron powder diffraction to investigate the magnetic structure and magnetic anisotropy of polycrystalline Fe-Co-Ti alloys. The most interesting finding in this work is the non-zero misalignment angle θ_c , which indicates a non-zero projection of the magnetic moments onto both the c axis and basal plane and the dependence of θ_c on the Co content. We explain these findings as a type of random-anisotropy effect caused by Co-Fe chemical disorder that translates into a micromagnetic spin canting. The added Co leads to a K_1 distribution, that is, to an atomic-scale coexistence of easy-axis and easy-plane anisotropies, and this distribution enhances the width δ in **Fig. 3.5** and, therefore the angle θ_c . An interesting feature is the weak power-law dependence of δ on D , which explains why the atomic-scale chemical-disorder effect is visible on a scale of about 40 nm.

References

- [1] Strnat K J 1978 Rare-earth magnets in present production and development *J. Magn. Mater.* **7** 351–60
- [2] Strnat K J and Strnat R M W 1991 Rare earth-cobalt permanent magnets *J. Magn.*

Magn. Mater. **100** 38–56

- [3] Gutfleisch O, Willard M A, Brück E, Chen C H, Sankar S G and Liu J P 2011 Magnetic Materials and Devices for the 21st Century: Stronger, Lighter, and More Energy Efficient *Adv. Mater.* **23** 821–42
- [4] Skomski R, Manchanda P, Kumar P, Balamurugan B, Kashyap A and Sellmyer D J 2013 Predicting the Future of Permanent-Magnet Materials *IEEE Trans. Magn.* **49** 3215–20
- [5] Skomski R and Coey J M D 2016 Magnetic anisotropy — How much is enough for a permanent magnet? *Scr. Mater.* **112** 3–8
- [6] Cui J, Kramer M, Zhou L, Liu F, Gabay A, Hadjipanayis G, Balasubramanian B and Sellmyer D 2018 Current progress and future challenges in rare-earth-free permanent magnets *Acta Mater.* **158** 118–37
- [7] Kumar K 1988 $RETM_5$ and RE_2TM_{17} permanent magnets development *J. Appl. Phys.* **63** R13–57
- [8] Kumar R, Yelon W B and Fuerst C D 1988 Neutron determination of the magnetic order and site preference in $Er_2(Co_xFe_{1-x})_{17}$ *J. Appl. Phys.* **63** 3725–7
- [9] Herbst J F 1991 $R_2Fe_{14}B$ materials: Intrinsic properties and technological aspects *Rev. Mod. Phys.* **63** 819–98
- [10] Skomski R and Coey J M D 1999 *Permanent magnetism* (Bristol; Philadelphia: Institute of Physics Publishing)
- [11] Skomski R and Coey J M D 1993 Giant energy product in nanostructured two-phase magnets *Phys. Rev. B* **48** 15812–6

- [12] Bader S D 2006 Colloquium: Opportunities in nanomagnetism *Rev. Mod. Phys.* **78** 1–15
- [13] Jones N 2011 Materials science: The pull of stronger magnets *Nature* **472** 22–3
- [14] Coey J M D 2011 Hard Magnetic Materials: A Perspective *IEEE Trans. Magn.* **47** 4671–81
- [15] Coey J M D 2014 New permanent magnets; manganese compounds *J. Phys. Condens. Matter* **26** 64211
- [16] Snow R J, Bhatkar H, N'Diaye A T, Arenholz E and Idzerda Y U 2018 Large moments in bcc $\text{Fe}_x\text{Co}_y\text{Mn}_z$ ternary alloy thin films *Appl. Phys. Lett.* **112** 72403
- [17] Lewis L H, Pinkerton F E, Bordeaux N, Mubarak A, Poirier E, Goldstein J I, Skomski R and Barmak K 2014 De Magnete et Meteorite: Cosmically Motivated Materials *IEEE Magn. Lett.* **5** 1–4
- [18] Balasubramanian B, Das B, Skomski R, Zhang W Y and Sellmyer D J 2013 Novel nanostructured rare-earth-free magnetic materials with high energy products *Adv. Mater.* **25** 6090–3
- [19] Néel L, Pauleve J, Pauthenet R, Laugier J and Dautreppe D 1964 Magnetic properties of an iron - nickel single crystal ordered by neutron bombardment *J. Appl. Phys.* **35** 873–6
- [20] Sanvito S, Oses C, Xue J, Tiwari A, Zic M, Archer T, Tozman P, Venkatesan M, Coey M and Curtarolo S 2017 Accelerated discovery of new magnets in the Heusler alloy family *Sci. Adv.* **3** 1–10
- [21] Balamurugan B, Das B, Zhang W Y, Skomski R and Sellmyer D J 2014 Hf-Co

and Zr-Co alloys for rare-earth-free permanent magnets *J. Phys. Condens. Matter* **26**

- [22] Zhang J, Nguyen M C, Balasubramanian B, Das B, Sellmyer D J, Zeng Z, Ho K-M and Wang C-Z 2016 Crystal structure and magnetic properties of new $\text{Fe}_3\text{Co}_3\text{X}_2$ ($X = \text{Ti, Nb}$) intermetallic compounds *J. Phys. D. Appl. Phys.* **49** 175002
- [23] Xu X, Zhang X, Yin Y, Balasubramanian B, Das B, Liu Y, Huq A and Sellmyer D J 2017 Anti-site mixing and magnetic properties of $\text{Fe}_3\text{Co}_3\text{Nb}_2$ studied via neutron powder diffraction *J. Phys. D. Appl. Phys.* **50** 25002
- [24] Balasubramanian B, Das B, Nguyen M C, Xu X, Zhang J, Zhang X, Liu Y, Huq A, Valloppilly S R, Jin Y, Wang C-Z, Ho K-M and Sellmyer D J 2016 Structure and magnetism of new rare-earth-free intermetallic compounds: $\text{Fe}_{3+x}\text{Co}_{3-x}\text{Ti}_2$ ($0 \leq x \leq 3$) *APL Mater.* **4** 116109
- [25] Skomski R 2003 Nanomagnetism *J. Phys. Condens. Matter* **15** R841–96
- [26] Weissmüller J, Michels A, Barker J G, Wiedenmann A, Erb U and Shull R D 2001 Analysis of the small-angle neutron scattering of nanocrystalline ferromagnets using a micromagnetics model *Phys. Rev. B* **63** 214414
- [27] Michels A and Weissmueller J 2008 Magnetic-field-dependent small-angle neutron scattering on random anisotropy ferromagnets *Reports Prog. Phys.* **71** 37
- [28] Michels A 2014 Magnetic small-angle neutron scattering of bulk ferromagnets *J. Phys. Condens. Matter* **26** 383201
- [29] Balasubramanian B, Manchanda P, Skomski R, Mukherjee P, Valloppilly S R, Das B, Hadjipanayis G C and Sellmyer D J 2016 High-coercivity magnetism in

- nanostructures with strong easy-plane anisotropy *Appl. Phys. Lett.* **108** 152406
- [30] Bolzoni F, Moze O and Pareti L 1987 First-order field-induced magnetization transitions in single-crystal $\text{Nd}_2\text{Fe}_{14}\text{B}$ *J. Appl. Phys.* **62** 615–20
- [31] Callen E, Liu Y J and Cullen J R 1977 Initial magnetization, remanence, and coercivity of the random anisotropy amorphous ferromagnet *Phys. Rev. B* **16** 263–70
- [32] Sellmyer D J and Nafis S 1986 Phase-Transition Behavior in a Random-Anisotropy System *Phys. Rev. Lett.* **57** 1173–6
- [33] Herzer G 1992 Nanocrystalline soft magnetic materials *J. Magn. Magn. Mater.* **112** 258–62
- [34] Shull C G, Strauser W A and Wollan E O 1951 Neutron diffraction by paramagnetic and antiferromagnetic substances *Phys. Rev.* **83** 333–45
- [35] Roberts B W 1956 Neutron Diffraction Study of the Structures and Magnetic Properties of Manganese Bismuthide *Phys. Rev.* **104** 607–16
- [36] Braun P B and Goedkoop J A 1963 An X-ray and neutron diffraction investigation of the magnetic phase $\text{Al}_{0.89}\text{Mn}_{1.11}$ *Acta Crystallogr.* **16** 737–40
- [37] Andresen A F, Halg W, Fischer P and Stoll E 1967 The magnetic & crystallographic properties of MnBi studied by Neutron diffraction *Acta Chem. Scand.* **21** 1543–54
- [38] Yang Y C, Ho W W, Lin C, Yang J L, Zhou H M, Zhu J X, Zeng X X, Zhang B S and Jin L 1984 Neutron diffraction study of hard magnetic alloy MnAlC *J. Appl. Phys.* **55** 2053–4

- [39] Squires G L 2013 Introduction to the theory of thermal neutron scattering
- [40] Cui J, Choi J P, Li G, Polikarpov E, Darsell J, Kramer M J, Zarkevich N A, Wang L L, Johnson D D, Marinescu M, Huang Q Z, Wu H, Vuong N V. and Liu J P 2014 Development of MnBi permanent magnet: Neutron diffraction of MnBi powder *J. Appl. Phys.* **115** 17A743
- [41] Givord D, Li H S and Tasset F 1985 Polarized neutron study of the compounds $\text{Y}_2\text{Fe}_{14}\text{B}$ and $\text{Nd}_2\text{Fe}_{14}\text{B}$ *J. Appl. Phys.* **57** 4100–2
- [42] Herbst J F and Yelon W B 1985 Crystal and magnetic structure of $\text{Pr}_2\text{Fe}_{14}\text{B}$ and $\text{Dy}_2\text{Fe}_{14}\text{B}$ *J. Appl. Phys.* **57** 2343–5
- [43] Ritveld H M 1969 A profile refinement method for nuclear and magnetic structures *J. Appl. Crystallogr.* **2** 65
- [44] Rodríguez-Carvajal J 1993 Recent advances in magnetic structure determination by neutron powder diffraction *Phys. B Phys. Condens. Matter* **192** 55–69
- [45] Sears V F 1992 Neutron scattering lengths and cross sections *Neutron News* **3** 26–37
- [46] Supplementary See *Suppl. Mater.*
<https://journals.aps.org/prmaterials/supplemental/10.1103/PhysRevMaterials.3.064403> more Inf. *Diffr. spectra fit.*
- [47] Lide D R 1994 *CRC handbook of chemistry and physics : a ready-reference book of chemical and physical data* (Boca Raton, FL: CRC Press)
- [48] Prince International Union of Crystallography., E 2011 *International tables for crystallography. Volume C, Volume C*, (Chichester: J. Wiley & Sons for the

International union of crystallography)

- [49] Giacoletto L J 2008 Physics of magnetism *Proc. IEEE* **53** 2169–2169

Chapter IV: Effect of Boron Doping on Magnetic Anisotropy in Fe₂Ni Alloy Grown by Spin Melting Method

4.1 Introduction

Magnetic anisotropy comes from structure anisotropy, and one example is L1₀-FeNi. Fe and Ni are both soft magnetic while Fe has a body center cubic phase and Ni has a face center cubic face. Different ratios of iron and nickel results in different crystal structure and magnetic structure. One of the most famous compounds of Fe-Ni is called permalloy, with a Fe-Ni ratio of 20:80. Permalloy has a very low magnetic anisotropy energy which means it is a soft magnetic material. Fe₇₀Ni₃₀ is called invar alloys since the thermal expansion can be very close to zero over several degrees. L1₀-FeNi is a well-ordered Fe₅₀Ni₅₀ intermetallic compound with a magnetic anisotropy as high as 1 MJ/m³. [1] The crystal structure of L1₀-FeNi is shown in **Fig. 4.1**, [2] with $a=b=3.57\text{\AA}$ and $c=3.58\text{\AA}$. As a comparison, the magnetic anisotropy of Fe-Ni solid solution is usually lower than 50 kJ/m³ (5×10^5 erg/cm³). [3] However, L1₀-FeNi requires millions of years to anneal, and it is only found in meteorites. As a result, a well-ordered FeNi alloy with an appropriate annealing time might be a good candidate for hard magnets.

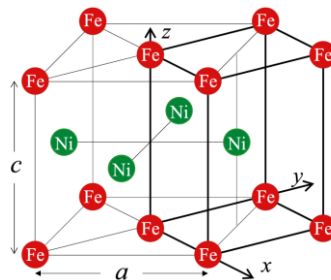


Figure 4.1: Crystal structure of L1₀-FeNi. [2]

Boron's unique chemical properties and its reactions with metals have yielded a large class of metal borides with compositions ranging from the most boron-rich YB_{66} to the most metal-rich $Nd_2Fe_{14}B$ (the best permanent magnet to date). The latter compound is probably the most famous metal boride (neodymium magnet). Moreover, boron-rich material displays high stability toward radiation. For example, YB_{66} is used as monochromators for soft synchrotron radiation,[4] and LaB_6 is used as a thermionic emitter.[5] In many crystal structures of metal-rich borides, the boron atoms are located in trigonal prisms built by metal atoms, but sometimes it is octahedral (boride perovskites[6]) or square antiprismatic ($CuAl_2$ -type borides[7]). Due to the small ionic radius of boron, it is always used in doping to refine the grain size of various magnetic materials, for example, $Co_{88}Hf$ [8] and $Ni_{50}Mn_{35}In_{15}$ [9]. The ability of boron to form strong chemical bonds with itself and with metallic elements has enabled us to construct new structures with desirable properties.[10] Doping boron in alloys does not always change the crystal structure of the material. However, boron plays a role in forming fine structures like dense lamella structures.[11] As a result, doping boron may play a positive role in forming a crystal structure different from the original one, which increases the magnetic anisotropy of the material.

In this work, we focus on the crystal structure and magnetic anisotropy of the Fe_4Ni_2B compound. Mixing Fe and Ni result in either a face center cubic or body center cubic structure and the transition ratio is around Fe: Ni=2:1. So Fe_4Ni_2 has two possible crystal structures (face center cubic and body center cubic). However, Fe_4Ni_2 alloy has a low magnetic anisotropy of around $500J/m^3$ (5×10^3 ergs/cm³),[3] and the coercivity can be as low as 80 A/m (1 Oe).[12] By adding boron into Fe_2Ni , theoretical prediction

shows that $\text{Fe}_4\text{Ni}_2\text{B}$ has a tetragonal structure with $a=b=3.611\text{\AA}$ and $c=11.128\text{\AA}$. The predicted crystal structure of $\text{Fe}_4\text{Ni}_2\text{B}$ is shown in **Fig. 4.2**, which can be treated as a combination of three distorted face center cubic. We found that adding boron increases the magnetic anisotropy energy to more than 6 kJ/m^3 ($6\times 10^4\text{ ergs/cm}^3$), which is 10 times larger than Fe_2Ni alloy. This dramatic difference in magnetic anisotropy may come from the difference of crystal structure induced by boron bonds.

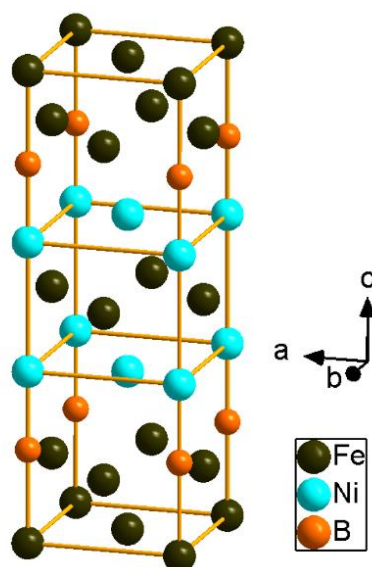


Figure 4.2: Theoretical crystal structure of $\text{Fe}_4\text{Ni}_2\text{B}$.

4.2 Experiment Details

Two batches of Fe-Ni-B samples with different proportions of boron have been used to study the effect of B on crystal structure and magnetism. The nominal molar ratio of Fe, Ni, and B is 4:2:1 and 4:2:1.3, corresponding to a weight ratio of 111.69: 58.69: 10.81 and 111.69: 58.69: 14.05, respectively. The polycrystalline samples are first

produced by arc melting. The samples are put in an arc melting furnace ABJ-338 and melted into a bulk alloy via an electric arc struck between a tungsten electrode and metals placed in a copper holder. In our experiment, the chamber is backfilled with Argon to avoid oxidation. Then, the melted Fe-Ni-B alloy is put into a melt-spinning instrument (Edmund Bühler GmbH melt spinner SC) with an argon environment. The melt spinning instrument drops melted liquid alloys onto a rotating wheel, which is cooled internally. In our experiment, a wheel speed of 57.5 m/s was used to produce rapidly quenched ribbons of approximate width of 2 mm and thickness of 40 μm . The produced alloy strips are annealed in MTI 1700C Compact Muffle Furnace in a vacuum environment with a temperature range between 570 K (300 $^{\circ}\text{C}$) and 870 K (600 $^{\circ}\text{C}$). X-ray diffraction is carried out with PANalytical Empyrean Diffractometer using Cu K_{α} radiation of a wavelength of 1.5406 \AA . A Quantum Design MPMS superconducting quantum-interference device (SQUID) was used to measure the magnetic properties.

4.3 Crystal Structure of Fe-Ni-B Alloy

Sample	XPS including Boron (at.%)	Component with XPS data
$\text{Fe}_4\text{Ni}_2\text{B}$ nominal	Fe: 57.1 Ni: 28.7 B: 14.2	$\text{Fe}_4\text{Ni}_2\text{B}$
$\text{Fe}_4\text{Ni}_2\text{B}_{1.05}$	Fe: 59.3 Ni: 31.1 B: 9.6	$\text{Fe}_4\text{Ni}_{2.09}\text{B}_{0.65}$
$\text{Fe}_4\text{Ni}_2\text{B}_{1.2}$	Fe: 51.7 Ni: 26.3 B: 22.0	$\text{Fe}_4\text{Ni}_{2.02}\text{B}_{1.71}$

Table 4.1: Composition analysis for $\text{Fe}_4\text{Ni}_2\text{B}$ samples

X-ray Photoelectron Spectroscopy (XPS) is carried out to ensure the successful doping of boron. **Table 4.1** shows the composition analysis for two sets of $\text{Fe}_4\text{Ni}_2\text{B}_x$. In both sets, boron doping is confirmed, and the B proportion is correlated to the nominal values. We can control the ratio of iron and nickel well, but the portion of boron is hard to control due to the extreme light weight of the boron element. However, in both cases, there is no doubt about the existence of boron. As a result, in this chapter, we will focus on the effect of boron instead of different compositions of boron in alloys.

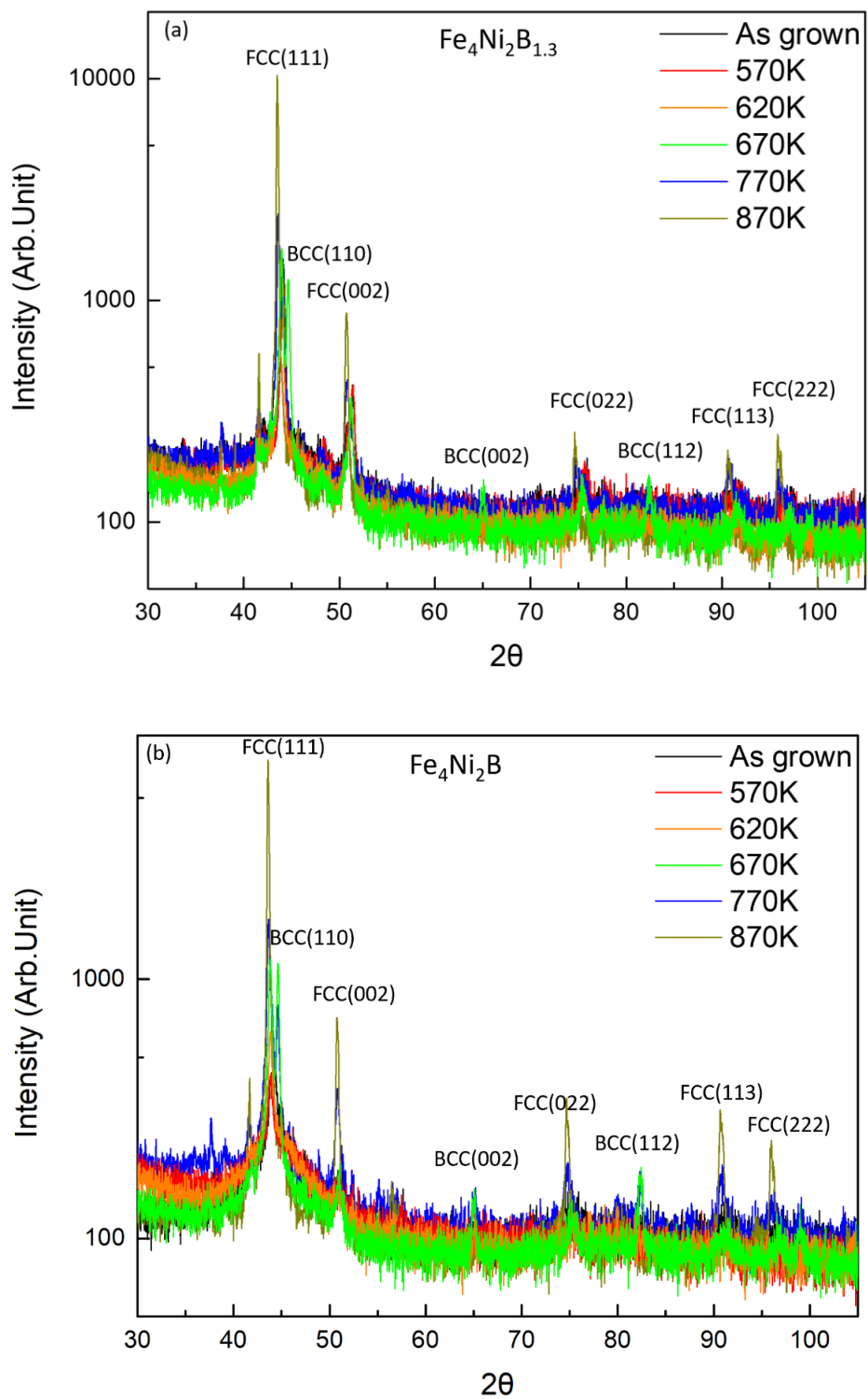


Figure 4.3: X-ray diffraction pattern of (a) $\text{Fe}_4\text{Ni}_2\text{B}_{1.3}$ and (b) $\text{Fe}_4\text{Ni}_2\text{B}$ at different annealing temperatures.

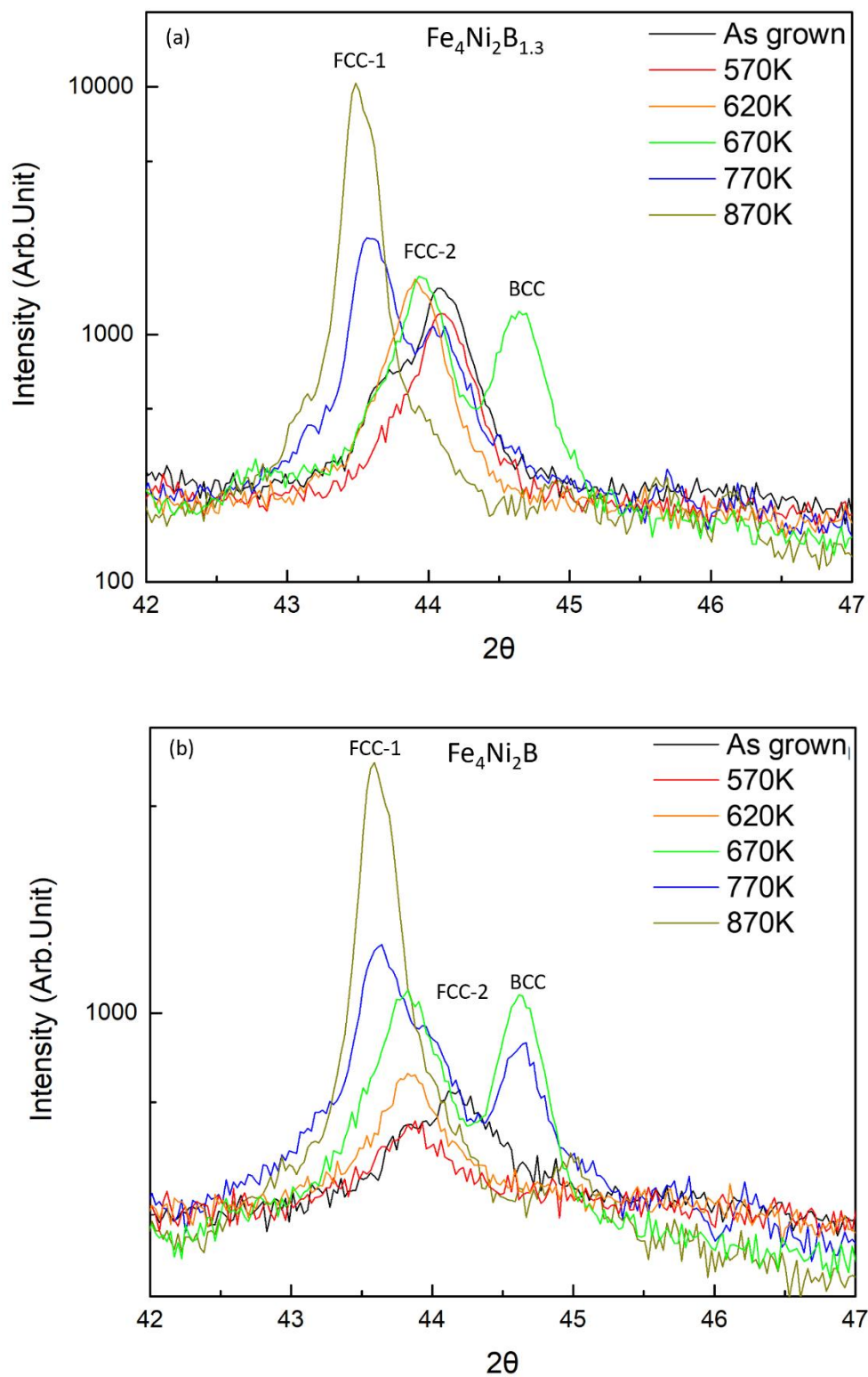


Figure 4.4: Enlarged graphs of the X-ray diffraction pattern from **Fig. 4.3** around the highest peak at $2\theta=44^\circ$ are shown in (a) and (b) for $\text{Fe}_4\text{Ni}_2\text{B}_{1.3}$ and $\text{Fe}_4\text{Ni}_2\text{B}$, respectively.

The X-ray diffraction pattern is displayed in **Fig. 4.3(a) and (b)**, with most peaks indexed. In addition to the as-grown samples, other samples have been annealed at a temperature range from 570 K (300 °C) to 870 K (600 °C).

The peaks with the highest intensity always appear around 2θ is equal to 44° , as displayed in two enlarged graphs in **Fig. 4.4(a) and (b)**. We clearly found one body center cubic structure (BCC) and two face center cubic structures (FCC-1 and FCC-2) separated. The D-spacing of the material can be calculated by Bragg's law, $2d\sin\theta=n\lambda$, where θ is the incident angle of the x-ray, λ is the wavelength of the x-ray, and d is the distance between planes. The crystal structure and cell parameter are determined by peaks in a broad range, as shown in **Fig. 4.3(a) and (b)**. The lattice constant of BCC can be calculated with peaks (110) (002) and (112), while the Lattice constant of FCC can be calculated with peaks (111) (002) (022) (113) and (222). **Tables 4.2 to 4.7** show the peak position and calculated cell parameter for three structures, the average cell parameters for FCC-1, FCC-2 and BCC are 3.592 Å, 3.562 Å, and 2.865, respectively. As a comparison, the lattice constant for Fe and Ni is 2.855 Å and 3.499 Å, respectively.[13] The lattice constant for a face center cubic Fe_2Ni is 3.58Å.[14] **Table 4.8** compares $\text{L}_{10}\text{-FeNi}$, FeNi alloy, $\text{Fe}_4\text{Ni}_2\text{B}$, and Ni. The two FCC structures in $\text{Fe}_4\text{Ni}_2\text{B}_{1.3}$ can be identified clearly in **Fig. 4.4(a)**, especially for samples annealing at 670 K (400 °C) and 770 K (500 °C), and BCC structure only appears in 670 K (400 °C) annealing sample. However, two FCC structures for $\text{Fe}_4\text{Ni}_2\text{B}$ is similar, and BCC structure appear in 670 K (400 °C), 770 K (500 °C) and 870 K (600 °C) annealed samples. This may suggest that boron enhances the preference of Fe-Ni alloy to FCC structure. And more boron in $\text{Fe}_4\text{Ni}_2\text{B}_{1.3}$ results in a

smaller lattice constant than that of the FCC-2 structure, which is consistent with previous study.[15]

Annealing temperature		Peak (111)	Peak (002)	Peak (022)	Peak (113)	Peak (222)
770 K (500 °C)	Peak position 2θ (°)	43.58	50.78	74.66	90.65	95.93
	Lattice constant (Å)	3.594	3.593	3.592	3.593	3.593
870 K (600 °C)	Peak position 2θ (°)	43.52	50.75	74.66	90.65	95.90
	Lattice constant (Å)	3.598	3.595	3.593	3.593	3.594

Table 4.2: Peak position (2θ) and corresponding lattice constant of FCC-1 structure in $\text{Fe}_4\text{Ni}_2\text{B}_{1.3}$.

Annealing temperature		Peak (111)	Peak (002)	Peak (022)	Peak (113)	Peak (222)
770 K (500 °C)	Peak position 2θ (°)	43.68	50.81	74.78	90.80	96.02
	Lattice constant (Å)	3.586	3.591	3.588	3.588	3.590
870 K (600 °C)	Peak position 2θ (°)	43.57	50.81	74.65	90.77	96.04
	Lattice constant (Å)	3.595	3.591	3.593	3.589	3.590

Table 4.3: Peak position (2θ) and corresponding lattice constant of FCC-1 structure in $\text{Fe}_4\text{Ni}_2\text{B}$.

Annealing temperature		Peak (111)	Peak (002)	Peak (022)	Peak (113)	Peak (222)
570 K (300 °C)	Peak position 2θ (°)	44.12	51.40	75.80	92.05	97.21
	Lattice constant (Å)	3.552	3.553	3.547	3.550	3.557
620 K (350 °C)	Peak position 2θ (°)	43.92	51.24	75.63	92.42	97.65
	Lattice constant (Å)	3.568	3.563	3.554	3.539	3.545
670 K (400 °C)	Peak position 2θ (°)	44.24	51.31	75.82	92.13	97.54
	Lattice constant (Å)	3.553	3.558	3.546	3.548	3.548
770 K (500 °C)	Peak position 2θ (°)	44.05	51.12	75.55	92.27	97.66
	Lattice constant (Å)	3.558	3.570	3.557	3.544	3.544

Table 4.4: Peak position (2θ) and corresponding lattice constant of FCC-2 structure in $\text{Fe}_4\text{Ni}_2\text{B}_{1.3}$.

Annealing temperature		Peak (111)	Peak (002)	Peak (022)	Peak (113)	Peak (222)
570 K (300 °C)	Peak position 2θ (°)	43.67	51.05	75.07	91.25	97.13
	Lattice constant (Å)	3.587	3.575	3.576	3.574	3.559
620 K (350 °C)	Peak position 2θ (°)	43.60	51.10	74.95	91.22	97.08
	Lattice constant (Å)	3.593	3.572	3.581	3.575	3.561
670 K (400 °C)	Peak position 2θ (°)	43.62	50.95	75.16	91.19	97.26
	Lattice constant (Å)	3.591	3.581	3.572	3.576	3.555

Table 4.5: Peak position (2θ) and corresponding lattice constant of FCC-2 structure in $\text{Fe}_4\text{Ni}_2\text{B}$.

Annealing temperature		Peak (110)	Peak (002)	Peak (112)
670 K (400 °C)	Peak position 2θ (°)	44.69	65.07	82.376
	Lattice constant (Å)	2.865	2.865	2.865

Table 4.6: Peak position (2θ) and corresponding lattice constant of BCC structure in $\text{Fe}_4\text{Ni}_2\text{B}_{1.3}$.

Annealing temperature		Peak (110)	Peak (002)	Peak (112)
670 K (400 °C)	Peak position 2θ (°)	44.64	65.07	82.43
	Lattice constant (Å)	2.868	2.865	2.864
770 K (500 °C)	Peak position 2θ (°)	44.66	65.12	82.35
	Lattice constant (Å)	2.867	2.863	2.866

Table 4.7: Peak position (2θ) and corresponding lattice constant of BCC structure in $\text{Fe}_4\text{Ni}_2\text{B}$.

	Lattice constant (Å)	Anisotropy constant (J/m^3)
L10-FeNi	3.57	$0.5-1 \times 10^6$
Fe_2Ni alloy	3.58	500
$\text{Fe}_4\text{Ni}_2\text{B}$	FCC1: 3.592	6000-12000
	FCC2: 3.562	
Ni	3.499	-5000

Table 4.8: Lattice constant and magnetic anisotropy constant of L1₀-FeNi, FeNi alloy, $\text{Fe}_4\text{Ni}_2\text{B}$, and Ni. All of them are face center cubic structures. XRD shows $\text{Fe}_4\text{Ni}_2\text{B}$ has two face center cubic structures.

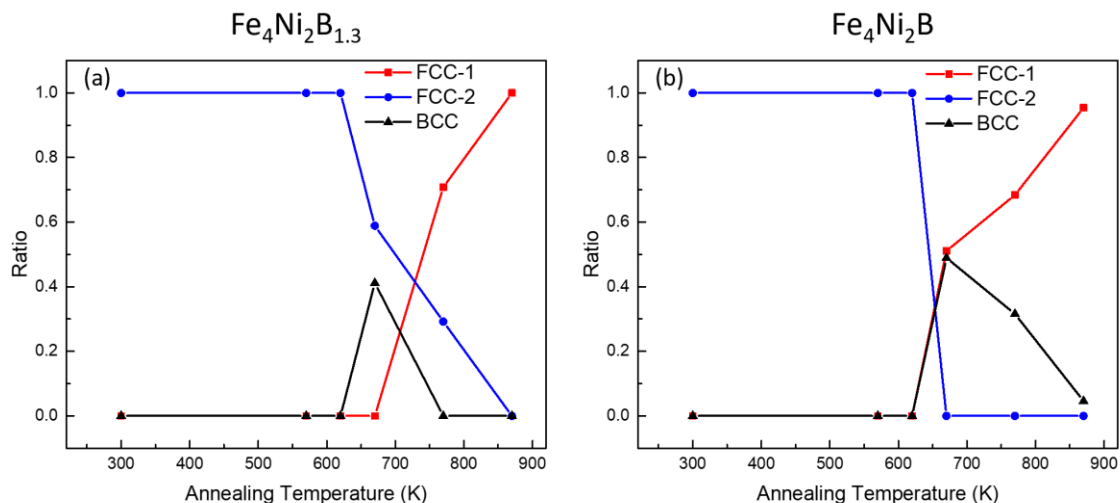


Figure 4.5: Composition ratio of three structures for different annealing temperatures.

Fig. 4.5 shows the proportion of different structures for samples of different annealing conditions. The Data is determined by the area of the highest peak around $2\theta=44^\circ$. For the as-grown sample and the samples of low annealing temperature (570 K/300 °C and 620 K/350 °C), there is only the FCC-2 structure with a cell parameter of around 3.56 Å. As the annealing temperature increases, the BCC and the FCC-1 structures start to appear at the cost of the FCC-2 structure. On the other hand, both the FCC-2 and the BCC structures appear to be intermediate structures because, for a high annealing temperature (870 K/600 °C), only the FCC-1 structure is left. For the $\text{Fe}_4\text{Ni}_2\text{B}_{1.3}$ sample, the range of annealing temperature for which the BCC structure occurs is very narrow such that there is no obvious coexistence of the BCC and the FCC-1 structures. Since the two batches of samples only differ in boron composition, a higher boron concentration destabilizes the BCC structure and promotes the FCC-1 structure.

4.4 Magnetic Behavior of Fe-Ni-B Alloy

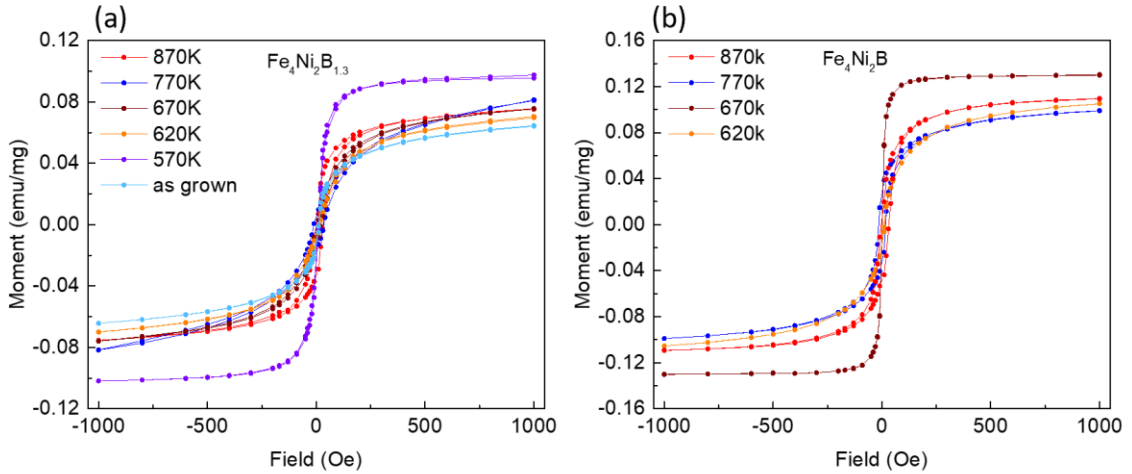


Figure 4.6: SQUID data for (a) $\text{Fe}_4\text{Ni}_2\text{B}_{1.3}$ and (b) $\text{Fe}_4\text{Ni}_2\text{B}$ for different temperatures.

Fig. 4.6 is the magnetization-field relation measured using SQUID for $\text{Fe}_4\text{Ni}_2\text{B}_{1.3}$ and $\text{Fe}_4\text{Ni}_2\text{B}$ at room temperature in the field range -1000 Oe to 1000 Oe. No subtraction of the background signal is necessary since the signal from samples are dominant (> 99%). The coercivity field is about 50 Oe, while saturation magnetization is around $1 \times 10^{-4} \text{ A} \cdot \text{m}^2/\text{g}$ (0.1 emu/mg), in comparison, saturation magnetization for Fe and Ni is $2.2 \times 10^{-4} \text{ A} \cdot \text{m}^2/\text{g}$ (0.22 emu/g) and $5.6 \times 10^{-5} \text{ A} \cdot \text{m}^2/\text{g}$ (0.056 emu/g), respectively[16].

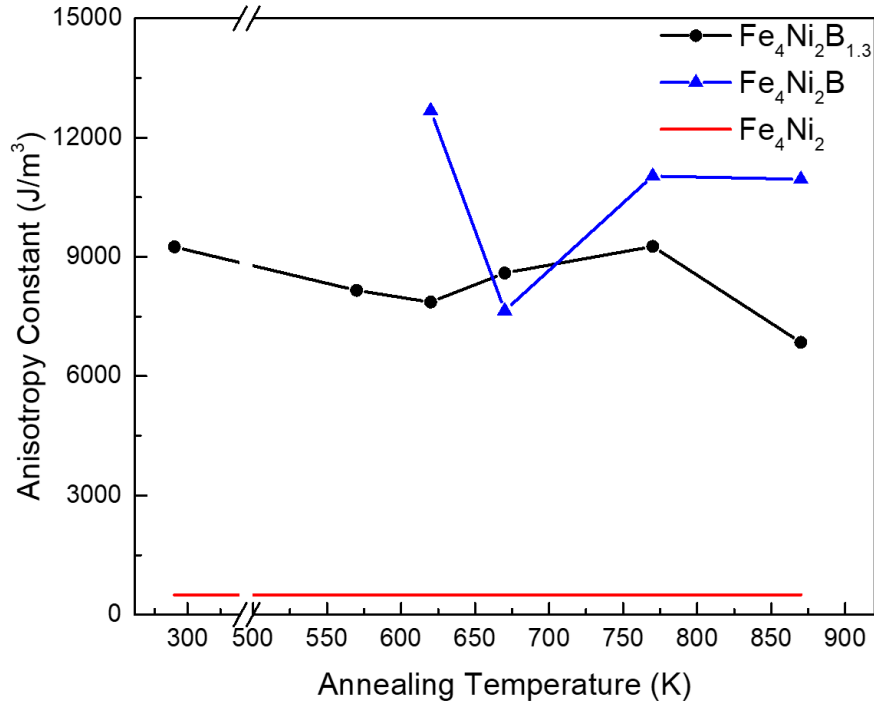


Figure 4.7: Anisotropy constant of Fe₄Ni₂B_{1.3} and Fe₄Ni₂B compared to Fe₄Ni₂

We use the law of approach to saturation method (LAS) to estimate the magnetocrystalline anisotropy constant K_1 . [17,18] The experimental magnetization data from **Fig. 4.6** in the high field range (higher than 500Oe) were fitted using the expression $M = M_s(1 - A/H^2) + \chi H$, where χ is the high-field susceptibility, and A is a parameter related to K_1 and the saturation magnetization M_s through $A = \frac{4K_1^2}{5M_s^2}$. The anisotropy constant is compared with that of Fe₄Ni₂ (also written as Fe₂Ni or Fe_{0.67}Ni_{0.33}). As **Fig. 4.7** shows, we see a clear increase in the anisotropy constant when adding boron into the iron-nickel alloy.

Boron should play an important role in Fe₄Ni₂B. Although we cannot resolve the exact crystal structure of Fe₄Ni₂B, previous work suggested that the strong covalent

metal–boron bonds in metal borides change the crystal structure.[10,11] The detailed structure difference between Fe₂Ni and Fe₄Ni₂B shown in **Table 4.8** may include a change in structural anisotropy. This structural anisotropy is expected to be the reason that the magnetic anisotropy constant increases from 500J/m³ (5×10³ ergs/cm³) to 6000J/m³ (6×10⁴ ergs/cm³).

4.5 Summary

To increase the magnetic anisotropy of Fe₂Ni alloy, we studied the effect of boron in FeNi alloy. We dope boron into Fe₂Ni with arc melting and melt spinning. Structure analysis with X-ray diffraction shows face center cubic or body center cubic structure in Fe₄Ni₂B alloy according to different annealing temperatures. Magnetic analysis with SQUID shows that the presence of boron dramatically increases the anisotropy of Fe₄Ni₂B by changing the lattice constant due to the strong metal-boron bonds. These results indicate that boron plays an important role in increasing the magnetic anisotropy of metal alloy, and Fe₄Ni₂B is a good candidate for rare-earth-free permanent magnets.

References

- [1] Paulevé J, Chamberod A, Krebs K and Bourret A 1968 Magnetization Curves of Fe–Ni (50–50) Single Crystals Ordered by Neutron Irradiation with an Applied Magnetic Field *J. Appl. Phys.* **39** 989–90
- [2] Miura Y, Ozaki S, Kuwahara Y, Tsujikawa M, Abe K and Shirai M 2013 The origin of perpendicular magneto-crystalline anisotropy in L1₀–FeNi under tetragonal distortion *J. Phys. Condens. Matter* **25** 106005

- [3] Hall R C 1959 Single Crystal Anisotropy and Magnetostriction Constants of Several Ferromagnetic Materials Including Alloys of NiFe, SiFe, AlFe, CoNi, and CoFe *J. Appl. Phys.* **30** 816–9
- [4] Wong J, Tanaka T, Rowen M, Schäfers F, Müller B R and Rek Z U 1999 YB₆₆-- a new soft X-ray monochromator for synchrotron radiation. II. Characterization *J. Synchrotron Radiat.* **6** 1086–95
- [5] Lafferty J M 1951 Boride Cathodes *J. Appl. Phys.* **22** 299–309
- [6] Fokwa B P T 2010 Transition-Metal-Rich Borides – Fascinating Crystal Structures and Magnetic Properties *Eur. J. Inorg. Chem.* **2010** 3075–92
- [7] Villars P 1997 *Pearson's handbook : crystallographic data for intermetallic phases.* (Materials Park, OH: ASM International)
- [8] Chang H W, Liao M C, Shih C W, Chang W C, Yang C C, Hsiao C H and Ouyang H 2014 Hard magnetic property enhancement of Co₇Hf-based ribbons by boron doping *Appl. Phys. Lett.* **105** 192404
- [9] Pandey S, Quetz A, Rodionov I D, Aryal A, Blinov M I, Titov I S, Prudnikov V N, Granovsky A B, Dubenko I, Stadler S and Ali N 2015 Magnetic, transport, and magnetocaloric properties of boron doped Ni-Mn-In alloys *J. Appl. Phys.* **117** 183905
- [10] Scheifers J P, Zhang Y and Fokwa B P T 2017 Boron: Enabling Exciting Metal-Rich Structures and Magnetic Properties *Acc. Chem. Res.* **50** 2317–25
- [11] Choi M, Cho S, Jo I, Song Y, Kim C, Yu J and Kim Y 2017 Boron behavior induced lamellar structure and anisotropic magnetic properties of Nd₂Fe₁₄B during HDDR process *J. Korean Phys. Soc.* **71** 130–3

- [12] Jerome R, Valet T and Galtier P 1994 Correlation between magnetic and structural properties of Ni₈₀Fe₂₀ sputtered thin films deposited on Cr and Ta buffer layers *IEEE Trans. Magn.* **30** 4878–80
- [13] Davey W P 1925 Precision Measurements of the Lattice Constants of Twelve Common Metals *Phys. Rev.* **25** 753–61
- [14] Hayase M, Shiga M and Nakamura Y 1973 Spontaneous Volume Magnetostriction and Lattice Constant of Face-Centered Cubic Fe-Ni and Ni-Cu Alloys *J. Phys. Soc. Japan* **34** 925–33
- [15] Xu X G, Yang H L, Wu Y, Zhang D L, Wu S Z, Miao J, Jiang Y, Qin X B, Cao X Z and Wang B Y 2010 Intrinsic room temperature ferromagnetism in boron-doped ZnO *Appl. Phys. Lett.* **97** 232502
- [16] Crangle J, Goodman G M and Sucksmith W 1971 The magnetization of pure iron and nickel *Proc. R. Soc. London. A. Math. Phys. Sci.* **321** 477–91
- [17] Kneller E 1962 *Ferromagnetism* (Berlin: Springer)
- [18] Hadjipanayis G, Sellmyer D J and Brandt B 1981 Rare-earth-rich metallic glasses. I. Magnetic hysteresis *Phys. Rev. B* **23** 3349–54

Chapter V: Magnetic Moments and Spin Structure in Single-Phase B20

$\text{Co}_{1+x}\text{Si}_{1-x}$ ($x=0.043$)

5.1 Introduction

The large atomic radius of metalloids, i.e., Si and Ge suppresses the electron transfer between transition metal (M) atoms and enlarges both the local density of states and spin-orbit coupling due to hybridization between M (Mn, Fe, Co) and Si/Ge states[1], typically leading to B20 crystal structures.[2–8] As illustrated in **Fig. 5.1(a)**, the B20 structure can be viewed as a rock-salt structure with a dimerization-type distortion involving displacement of M and Si/Ge atoms along the [111] direction[2], resulting in a crystal structure of non-centrosymmetric $P2_13$ space group with chirality, which induces the Dzyaloshinskii-Moriya (DM) exchange interaction,[9,10] favoring helical spin structures. The chiral structure of B20 materials also leads to a topological electronic structure with chiral fermions that produce transport properties of topological features.[11–15] In the helical phase, the spin directions rotate while propagating along the symmetry axis, resulting in short-range ferromagnetic and long-range antiferromagnetic alignments.[3–5,16] Helical spin structures with multiple propagation directions lead to the skyrmions spin texture.[17]

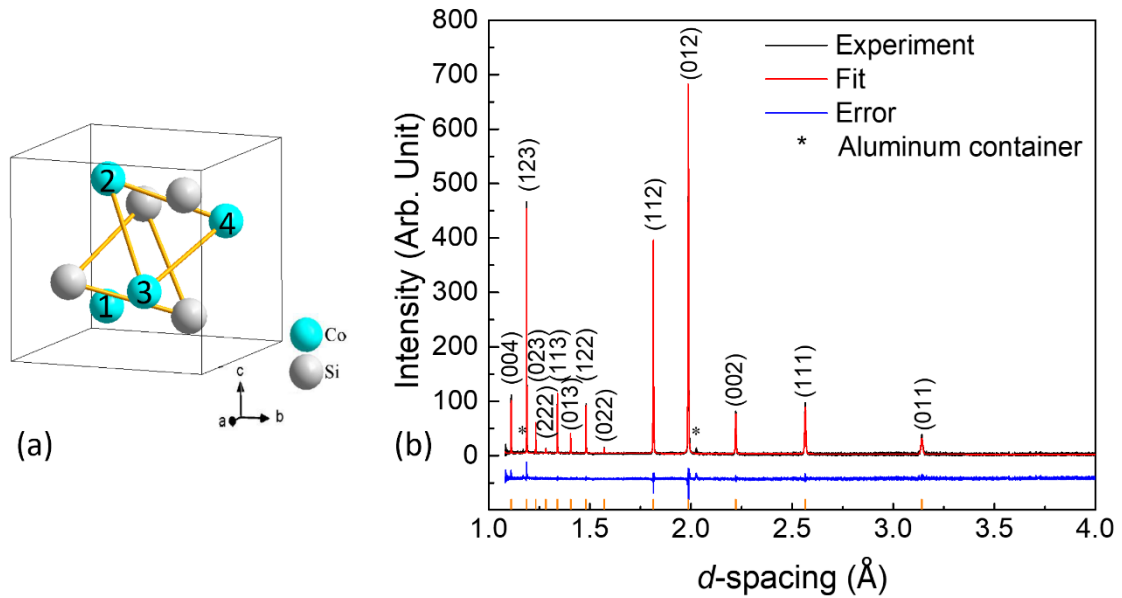


Figure 5.1:(a) Crystal structure of B20 Co-Si. Co atoms are indexed for describing spin structures. (b) Powder neutron diffraction pattern of Co-Si at 320 K and the fitting using the B20 structure.

The magnetic properties of B20 materials are sensitive to atomic species of the M site. As one of the most studied B20 materials,[2,16–18] MnSi exhibits a helical spin structure propagating along the [111] direction with a period of around 19 nm;[17] the magnetic moment is $0.4 \mu_B/\text{Mn atom}$ [2] while the Curie temperature T_c is only 29.5 K.[17] In contrast, CoSi and FeSi are diamagnetic and paramagnetic, respectively.[4] Interestingly, solid solutions of CoSi and FeSi, i.e., $\text{Fe}_x\text{Co}_{1-x}\text{Si}$, have helical spin structures for $0.2 < x < 0.95$,[3,4,19] with maximum magnetic ordering temperature about 59 K [4], maximum moment $0.17 \mu_B/(\text{Co/Fe})$, and helical period between 30 nm and 230 nm respectively[3]. $\text{Co}_x\text{Mn}_{1-x}\text{Si}$ and $\text{Fe}_x\text{Mn}_{1-x}\text{Si}$ are helimagnetic for $x < 0.08$ and $x < 0.19$ respectively.[3,6]

Replacing Si with Ge in MnSi leads to MnGe, another helimagnetic material with a B20 structure, a much higher ordering temperature (170 K), a much higher magnetic moment of $1.5 \mu_B/\text{Mn}$, and a much smaller helical period (3 - 6 nm related to temperature).[5,20] FeGe is a helimagnetic material with a magnetic moment of $1.0 \mu_B/\text{Fe}$ atom and ordering temperature around 278 K, and a period of approximately 70 nm;[7,21–23] $\text{Co}_x\text{Fe}_{1-x}\text{Ge}$ is also helimagnetic for $x \leq 0.8$, whose helical period strongly depends on x . [8,24] The formation of a helical phase in Fe-Ge is not restricted to B20 structures but also occurs with similar periodicity in amorphous materials with short-range order.[25]

Besides the atomic species on the M site and that on the Si/Ge site, relative stoichiometry between the M and Si/Ge sites also has a significant impact on the magnetic properties. Replacing a small portion of Si with Co ($\text{Co}_{1+x}\text{Si}_{1-x}$) induces magnetic ordering above a critical excess Co content of $x_c = 0.028$. [26] According to density-functional-theory (DFT) calculations, the excess Co atoms exhibit a large magnetic moment ($1.7 \mu_B/\text{Co}$) and also spin polarizing the surrounding Co atoms, which subsequently cause magnetic ordering in $\text{Co}_{1+x}\text{Si}_{1-x}$ through a quantum phase transition above x_c . The magnetometry measurements show magnetic transition temperatures of about 275 K and 328 K for $\text{Co}_{1.029}\text{Si}_{0.971}$ and $\text{Co}_{1.043}\text{Si}_{0.957}$, respectively.[26] $\text{Co}_{1.043}\text{Si}_{0.957}$ reveals further helimagnetic order and skyrmion lattices with a helical period of 17 nm at 300 K.[26] The small skyrmion dimension at high temperatures ($\lambda \sim 17$ nm) makes $\text{Co}_{1.043}\text{Si}_{0.957}$ an intriguing system from the viewpoint of understanding its spin structures and exploring skyrmions for practical room-temperature applications.

On the other hand, the question remains for the average Co magnetic moment in $\text{Co}_{1-x}\text{Si}_{1-x}$. For $\text{Co}_{1.043}\text{Si}_{0.957}$, the theory predicts a moment of $0.18 \mu_{\text{B}}/\text{Co}$, similar to that in $\text{Fe}_x\text{Co}_{1-x}\text{Si}$. [3] In contrast, magnetometry measurements show a magnetization of $0.11 \mu_{\text{B}}/\text{Co}$ at 70 kOe and 2 K, which still increases with the field. [26] The slow saturation suggests a robust conical state related to the small helical periodicity [27] in $\text{Co}_{1.043}\text{Si}_{0.957}$.

In this work, we report the magnetism and spin structure in single-phase B20 $\text{Co}_{1.043}\text{Si}_{0.957}$ (here referred to as Co-Si) using neutron powder diffraction (NPD) and x-ray magnetic circular dichroism (XMCD) spectroscopy. NPD allows for probing both the spin structure and the magnetic moment once the magnetic and nuclear contributions are separated, and the spin structure is taken into account. XMCD spectroscopy with total electron yield quantifies the normal moments near the surface (2-5 nm) [28] averaged over $100 \mu\text{m}$ in the lateral direction. The measured moments, $(0.3 \pm 0.1) \mu_{\text{B}}/\text{Co}$ at 0 kOe (NPD) and $(0.18 - 0.31) \mu_{\text{B}}/\text{Co}$ at 3 kOe (XMCD), are both substantially larger than the high-field magnetometry value, confirming the emergence of high-field conical states in Co-Si.

5.2 Experiment Details

The $\text{Co}_{1.043}\text{Si}_{0.957}$ ribbons with an approximate width of 2 mm and thickness of $40 \mu\text{m}$ were synthesized via melt-spinning. [26] For this, high-purity Co and Si with appropriate amounts were melted using a conventional arc-melting process to prepare the $\text{Co}_{1.043}\text{Si}_{0.957}$ alloy. The arc-melted alloy was then re-melted to a molten state in a quartz tube and subsequently ejected onto the surface of a water-cooled copper wheel rotating

with a speed of 15 m/s to form the ribbons. The cooling rate is of order 10^6 K s^{-1} . Our earlier study shows that the non-equilibrium rapid-quenching process creates $\text{Co}_{1+x}\text{Si}_{1-x}$ alloys with a maximum Co solubility of $x = 0.043$. The ribbons were mechanically grinded into powders suitable for neutron powder diffraction (NPD) measurements. The composition of $\text{Co}_{1+x}\text{Si}_{1-x}$ ($x=0.043$) was measured by energy dispersive x-ray spectroscopy (EDS). Rietveld refinement of XRD patterns and a linear increase of lattice constant on increasing Co content confirm that the excess Co atoms replace Si, and our alloy is a substitutional alloy of the solid-solution type.[26] Temperature-dependent high-resolution NPD measurements were carried out without an external magnetic field on the time-of-flight (TOF) powder diffractometer, POWGEN. POWGEN is a third-generation powder diffractometer and has the highest resolution to probe large unit cells in the powder suite at the Spallation Neutron Source Oak Ridge National Laboratory. The data were collected with neutrons with a central wavelength of 2.665 \AA . A cryofurnace was used as the sample environment to cover the temperature region between 20 K and 360 K. The sample mass was 3.53 g. The neutron diffraction patterns were analyzed using the Rietveld method, and the structure refinement was carried out using the FullProf program.[29] X-ray absorption spectroscopy (XAS) and x-ray magnetic circular dichroism (XMCD) spectroscopy were performed by detecting the total electron yield at beamline 4.0.2 at the Advanced Light Source, Berkeley, CA, which performs high resolution spectroscopy using circularly and linearly polarized X-rays. For these measurements, the ribbon sample was thinned into a thin film with a thickness $\approx 100 \text{ nm}$ using an ion-milling process at the Molecular Foundry, Berkeley, CA.

5.3 Spin Structure and Magnetic Moment from NPD

5.3.1 Crystal Structure

The powder neutron diffraction pattern of $\text{Co}_{1.043}\text{Si}_{0.957}$ at 320 K is displayed in **Fig. 5.1(b)** as a function of the spacing between diffraction planes d (called d -spacing). Taking advantage of the substantial contrast of the neutron scattering length of Co (2.49 fm) and Si (4.15 fm), the experimental spectrum can be fit using the B20 structure and the $\text{Co}_{1.043}\text{Si}_{0.957}$ composition with a random distribution of Co on Si sites by varying the lattice constants and atomic positions using the software FullProf.[29] All peaks are identified with the Miller indices (h, k, l) , as marked in **Fig. 5.1(b)**, except for the two peaks from the aluminum container. The diffraction peaks shift toward a larger d direction with increasing temperature, indicating thermal expansion [**Figs. 5.2(a-c)**]. The lattice constant is extracted using structural refinement and displayed in **Fig. 5.2(d)** as a function of temperature. Above 200 K, the thermal expansion is essentially linear with a coefficient of approximately $1.1 \times 10^{-5}/\text{K}$.

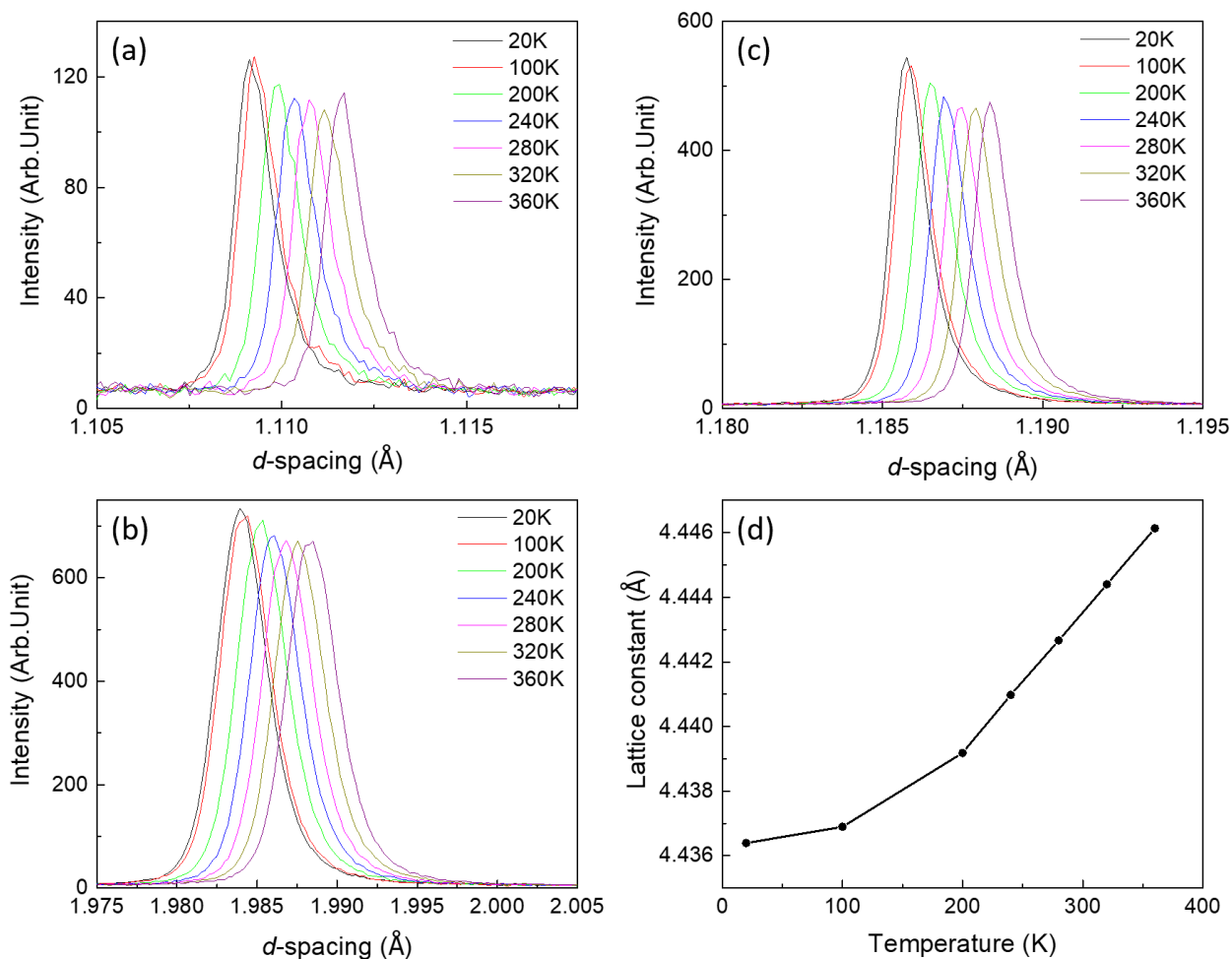


Figure 5.2: Neutron diffraction patterns at various temperatures for (a) (004), (b) (123), and (c) (012) peaks. (d) Temperature dependence of the lattice constants a .

5.3.2 Analysis of NPD Peak Broadening

Peak width is a parameter independent of peak intensity and position. In powder diffraction, peak width is determined by the size of the crystallites. Therefore, diffraction peak width is not expected to change with temperature as long as the temperature is not high enough to cause the change in crystallite size.

On the other hand, as the temperature changes, NPD peak width broadening has been observed for $\text{Co}_{1.043}\text{Si}_{0.957}$ studied in this work. As shown in **Fig. 5.3(a)**, after shifting and renormalization, the two (123) peak profiles measured at 20 and 320 K are plotted together as an example. A broadening of the 320 K peak compared to the 20 K peak is visible. The broadening is described using a factor called peak width ratio (PWR) using the 20 K peak profile as a reference. Essentially, the horizontal coordinate of the 320 K peak is scaled by the peak width ratio, which is varied to match the 20 K peak profile. The extracted peak width ratio is plotted in **Fig. 5.3(b)**.

Various processes can cause peak broadening. One possibility is the structural transition, e.g., from a cubic structure to a tetragonal structure. In this case, the single diffraction peak in the cubic structure may split in the tetragonal structure. When the splitting is too small to resolve, it manifests as a peak broadening. In this case, the relative splitting can be estimated from the broadening. Assuming the high-symmetry axis is c , **Fig. 5.3(b)** shows the calculated expansion of the c axis based on the lattice constants of $\text{Co}_{1.043}\text{Si}_{0.957}$, which is on the order of 10^{-3}\AA ; this value is too small to be meaningful.

Another possibility is that the diffraction peak consists of a main peak and hidden satellite peaks. In this case, the broadening suggests shifting of the satellite peaks.

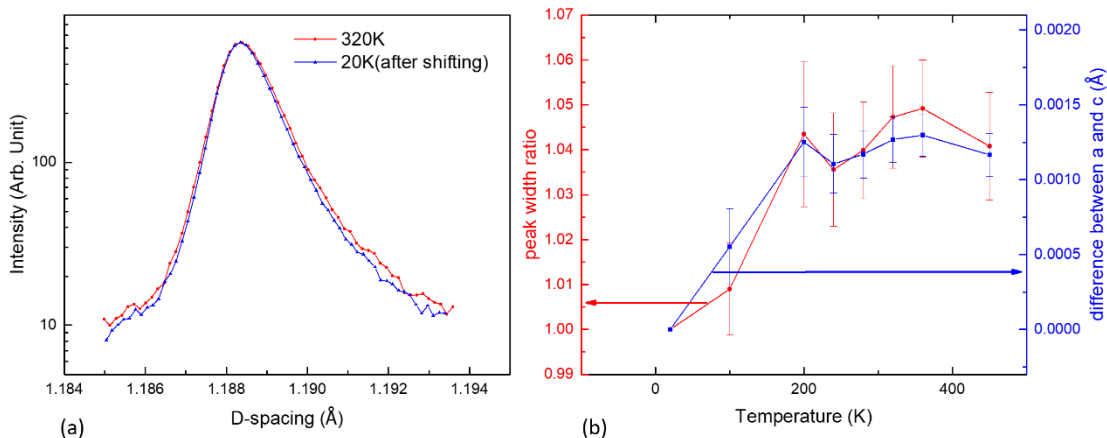


Figure 5.3: (a) peaks (123) at 20 K and 320 K which show a difference in peak width. (b) peak width ratio and possible expansion on the c axis. Due to thermal expansion, there is a slightly difference in peak position with the same peak at different temperature, “after shifting” in (a) means we move the peak at 20 K along x axis to be comparable to the same peak at 320 K.

5.3.3 Separation of Magnetic and Nuclear Contributions of the NPD

In **Chapter 2.3**, we separate the magnetic and nuclear contributions according to neutron powder diffraction data.

For magnetic materials, the neutron powder diffraction with an unpolarized beam contains nuclear (I_n) and magnetic (I_m) contributions, i.e., the total intensity $I(T, \vec{k}) = I_n(T, \vec{k}) + I_m(T, \vec{k})$, where T is temperature and \vec{k} is the wave-vector transfer, which is along the direction normal to the diffraction planes that can be expressed in reciprocal space vectors[30]. Notice that the experimental data in **Fig. 5.1(b)** and **Fig. 5.2(a-c)** corresponds to $I(T, \vec{k})$ summed over \vec{k} of different direction but the same magnitude

$|\vec{k}| = \frac{2\pi}{d}$, or $\sum_{|\vec{k}|=\frac{2\pi}{d}} I(T, \vec{k})$. Typically, the nuclear contribution decreases gradually with temperature due to the fluctuation of atomic positions at high temperature. The magnetic contribution, on the other hand, is expected to vanish at the magnetic ordering temperature. Our observations in **Figs. 5.2(a) to (c)** reveal a rapidly decreasing diffraction intensity at low temperature which becomes nearly constant at around 320 K, consistent with the magnetic transition occurring at around 320 K.[26]

The nuclear contribution $I_n(T)$ can be predicted if the Debye-Waller factor and I_n are known at a certain temperature since F_n is typically temperature independent as long as the structural symmetry is preserved. Lacking magnetic order at 320 K [26], the magnetic diffraction intensity is expected to be minimal. The function $W(T,d)$ can be written as $W(T,d) = \beta T/(4d^2)$, which represents the effect of thermal fluctuation of atomic positions.[31] One can fit the peak intensity as a function of d at 320 K using the linear relation between $\ln(I_n)/T$ and $1/(4d^2)$, yielding $\beta = 6 \times 10^{-4} \text{ \AA}^2/\text{T}$. The nuclear term is obtained as $I_n(T, \vec{k}) = I_n(T_1, \vec{k}) e^{-2\beta(T-T_1)/d^2}$ with $T_1 = 320 \text{ K}$. The magnetic contribution $I_m(T)$ is then extracted by subtracting the nuclear contribution, $I_m(T, \vec{k}) = I(T, \vec{k}) - I_n(T, \vec{k})$. **Fig. 5.4(a)** displays the magnetic contribution after removal of the Debye-Waller factor and the $B(\vec{K})$, i.e., $\sum_{|\vec{k}|=\frac{2\pi}{d}} \frac{I_m(T, \vec{k})}{B(\vec{K}) e^{-2W(T,d)}}$, where $B(\vec{K})$ is the multiplicity (number of possible \vec{k} of the same $|\vec{k}|$) of a diffraction peak at certain d . Overall, the magnetic contribution decreases with temperature and vanishes at about 320 K, while the magnitude varies significantly between diffraction peaks of different \vec{k} (or d).

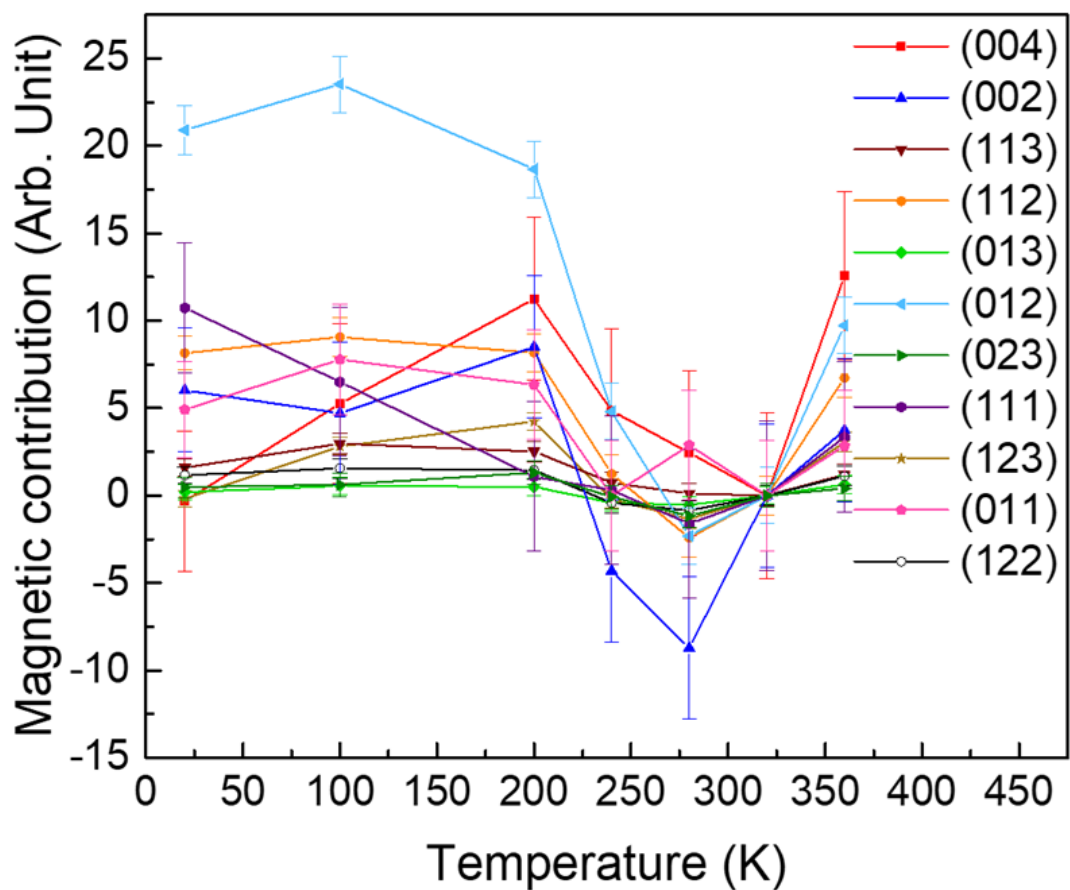


Figure 5.4: Experimental magnetic contribution as a function of temperature obtained by removing the nuclear contribution, multiplicity, and the Debye-Waller factor (see text) from the measured intensity (peak area).

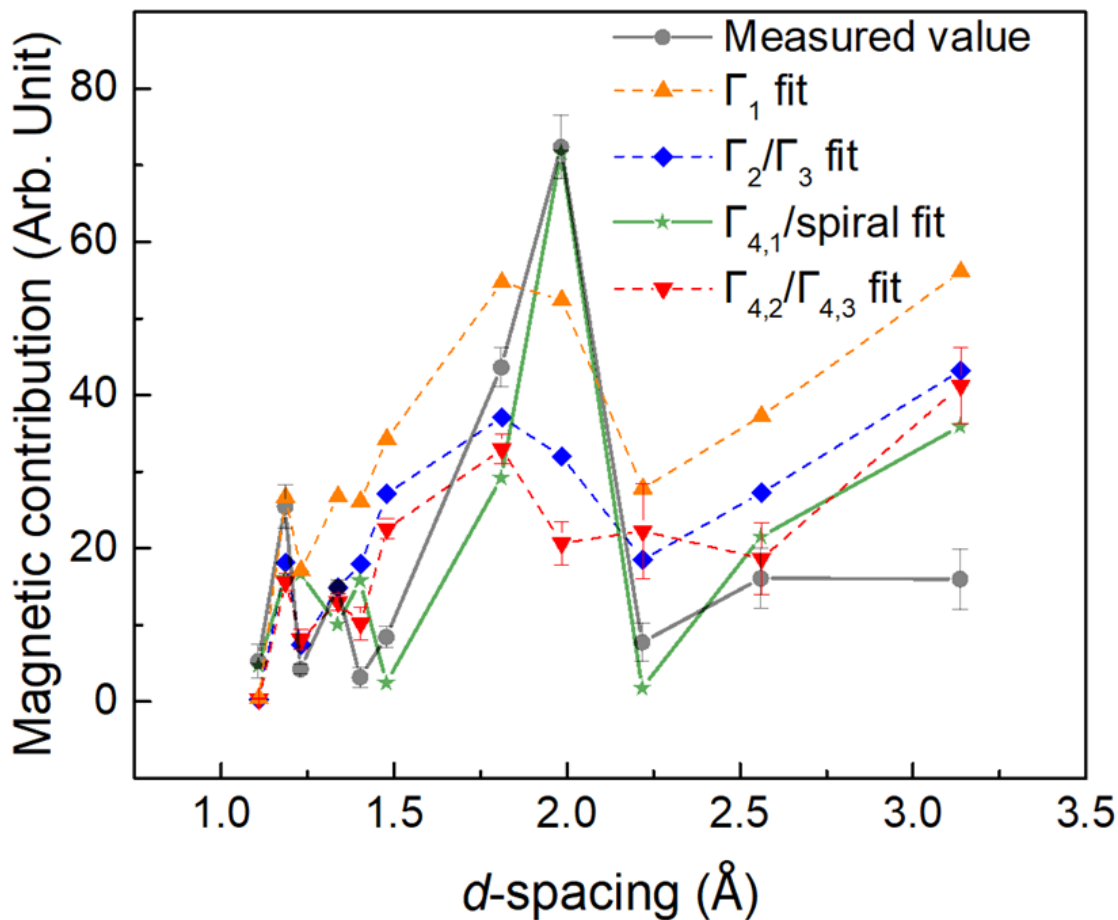


Figure 5.5: Experiment value of magnetic contribution as a function of d calculated by summing the data in **Fig. 5.4** over temperature. Also plotted are the best fit of the theoretical magnetic contribution $AF_m^2(\vec{k})$ to the experimental values by varying the factor A for different spin structures. Dashed lines are guidelines for eyes. The “error bars” of the theoretical contributions correspond to the variation when the spins are along different directions.

To highlight the dependence of the magnetic contribution on d , data in **Fig. 5.4** were summed over T and scaled with the peak multiplicity, i.e., $\sum_{|\vec{k}|=\frac{2\pi}{d}, T} \frac{I_m(T, \vec{k})}{B(\vec{k})e^{-2W(T, d)}}$ (**Fig. 5.5**). This dependence of the magnetic contribution on d is the key to analyzing the underlying spin structure.

With **Chapter 2.3.3**, we can calculate the magnetic contribution of neutron powder diffraction, the magnetic contribution is related to the spin structure.

$$F_m^2(\vec{k}) = \frac{1}{2} (\gamma r_0 g)^2 \left| \sum_{\vec{r}} \vec{q}(\vec{k}, \vec{r}) f'(\vec{k}, \vec{r}) \exp(i\vec{k} \cdot \vec{r}) \right|^2 \quad (5.1)$$

with

$$\vec{q}(\vec{k}, \vec{r}) \equiv \vec{s}(\vec{r}) - \hat{k}[\hat{k} \cdot \vec{s}(\vec{r})]. \quad (5.2)$$

A helical structure with a propagation vector \vec{k}_s , can be considered by writing $\vec{s}(\vec{r}) = \vec{s}_0(\vec{u})e^{-i\vec{k}_s \cdot \vec{R}}$ and $\vec{q}(\vec{k}, \vec{r}) = \vec{q}_0(\vec{k}, \vec{u})e^{-i\vec{k}_s \cdot \vec{R}}$, yielding

$$\sum_{\vec{r}} \vec{q}(\vec{k}, \vec{r}) f'(\vec{k}, \vec{r}) e^{i\vec{k} \cdot \vec{r}} = \sum_{\vec{u}} \vec{q}_0(\vec{k}, \vec{u}) f'(\vec{k}, \vec{u}) e^{i\vec{k} \cdot \vec{u}} \sum_{\vec{R}} e^{i(\vec{k}_s + \vec{k}) \cdot \vec{R}} \quad (5.3)$$

As shown in **Fig. 5.1(a)**, there are 4 Co sites in the B20 unit cell. While the site Co1 is on the [111] axis, the other three sites, Co2, Co3, and Co4, are related by the three-fold rotation along the [111] axis. The spin structure is described by the spin vectors on these Co sites $\vec{s}_0(\vec{u})$ and the propagation vector \vec{k}_s .

5.3.4 Group Theory Analysis of Spin Structures Allowed by the B20

Crystal Structure

In the following, we examine possible spin structures allowed by the $P2_13$ space group of the B20 structure using group theory.[32] The magnetic diffraction contribution simulated according to these spin structures will be compared with the experimental observation of Co-Si to determine the most likely spin structures.

First, we consider the case with no superstructure, i.e., $k_s = 0$ or uniform magnetization. According to the group theory analysis[32], the spin structure can be described by 4 irreducible Γ_1 to Γ_4 representations of the $P2_13$ space group, as displayed in **Table 5.1**. While the one-dimensional Γ_1 to Γ_3 appear only once, the three-dimensional Γ_4 appears three times. All spin structures have a zero net magnetic moment for the unit cell, meaning antiferromagnetic (AFM) order, except for $\Gamma_{4,1}$, which is ferromagnetic. More specifically, the AFM structures of Γ_1 , $\Gamma_{4,2}$, and $\Gamma_{4,3}$ are collinear, while Γ_2 and Γ_3 are non-collinear. Compared with the experimental observation, only the ferromagnetic spin structure $\Gamma_{4,1}$ generates a magnetic contribution that matches reasonably well, while other spin structures do not (**Fig. 5.5**).

With a propagation vector $\vec{k}_s \parallel [111]$, the arrangement Co magnetic moment can be divided into two groups, Co1 in group I and Co2 – Co4 for group II. **Table 5.2** shows the spin structure of the spin helix for $\vec{k}_s \parallel [111]$ allowed by the $P2_13$ space group for Co group I. The two helical spin structures $\Gamma_2(\text{I})$ and $\Gamma_3(\text{I})$ of opposite chirality are one-dimensional. Both spins are perpendicular to the $[111]$ axis and rotate along the axis from unit cell to unit cell [see **Fig. 5.3**]. **Table 5.3** shows the spin structure for the Co group II, where $\Gamma_2(\text{II})$

and $\Gamma_3(\text{II})$ form helical structure as $\Gamma_{2,1}(\text{II}) + e^{-\frac{i2\pi}{3}}\Gamma_{2,2}(\text{II}) + e^{-\frac{i4\pi}{3}}\Gamma_{2,3}(\text{II})$ and $\Gamma_{3,1}(\text{II}) + e^{\frac{i2\pi}{3}}\Gamma_{3,2}(\text{II}) + e^{\frac{i4\pi}{3}}\Gamma_{3,3}(\text{II})$ for Co group II, respectively. The additional restriction from the exchange interaction, which is not considered in the group-theory analysis, connects the spins of the two groups. For B20 material, the short-range exchange interaction is generally ferromagnetic,[3,8,24,26] meaning the magnetic moments are almost perfectly parallel within one unit cell. Under this constriction, two helical structures are formed, including all the Co atoms: $[\Gamma_2(\text{I})e^{\frac{ik_s a}{\sqrt{3}}}, \Gamma_{2,1}(\text{II}) + e^{-\frac{i2\pi}{3}}\Gamma_{2,2}(\text{II}) + e^{-\frac{i4\pi}{3}}\Gamma_{2,3}(\text{II})]$, and $[\Gamma_3(\text{I})e^{\frac{ik_s a}{\sqrt{3}}}, \Gamma_{3,1}(\text{II}) + e^{\frac{i2\pi}{3}}\Gamma_{3,2}(\text{II}) + e^{\frac{i4\pi}{3}}\Gamma_{3,3}(\text{II})]$, for opposite chirality, respectively [**Fig. 5.6(a)**].

Another propagation direction that leads to helical spins is $\vec{k}_s \parallel [100]$. There are also two groups of Co atoms: group I (Co1 and Co2) and group II (Co3 and Co4). **Table 5.4** shows the allowed spin structures for groups I and II with $\vec{k}_s \parallel [100]$. Again, helical structures are formed within both atomic groups. The restriction of exchange interaction connects the two groups and results in the helical structures, including all Co atoms: $[\Gamma_{1,2}(\text{I}) + i\Gamma_{1,3}(\text{I}), \Gamma_{1,2}(\text{II}) + i\Gamma_{1,3}(\text{II})]$ and $[\Gamma_{1,2}(\text{I}) - i\Gamma_{1,3}(\text{I}), \Gamma_{1,2}(\text{II}) - i\Gamma_{1,3}(\text{II})]$ for opposite chirality [**Fig. 5.6(b)**].

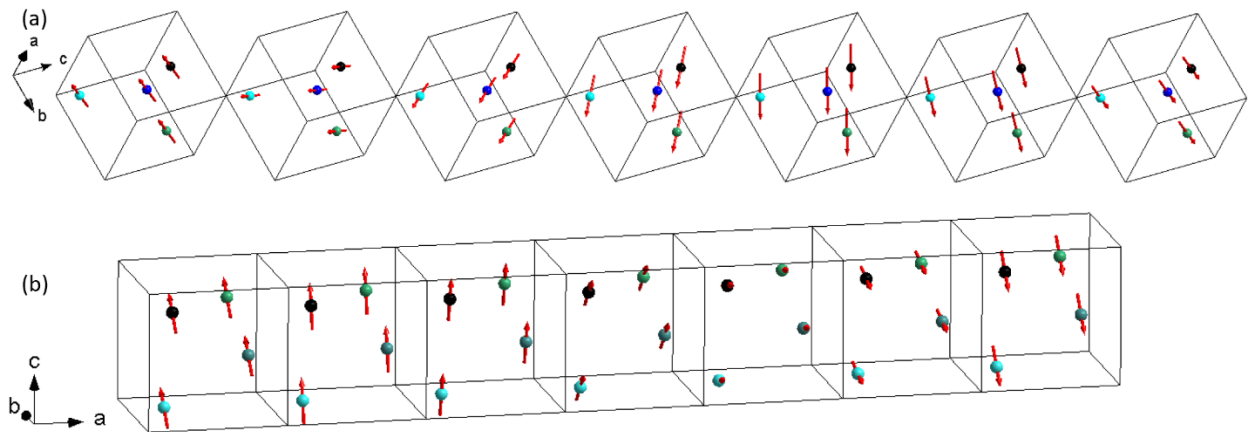


Figure 5.6: Schematic illustration of helical spin structures for propagation vector (a) $\vec{k}_S \parallel [111]$ and (b) $\vec{k}_S \parallel [100]$.

	Co1	Co2	Co3	Co4
Γ_1	(1, 1, 1)	(-1, -1, 1)	(-1, 1, -1)	(1, -1, -1)
Γ_2	$(1, e^{-\frac{i2\pi}{3}}, e^{\frac{i2\pi}{3}})$	$(-1, e^{\frac{i\pi}{3}}, e^{\frac{i2\pi}{3}})$	$(-1, e^{-\frac{i2\pi}{3}}, e^{-\frac{i\pi}{3}})$	$(1, e^{\frac{i\pi}{3}}, e^{-\frac{i\pi}{3}})$
Γ_3	$(1, e^{\frac{i2\pi}{3}}, e^{-\frac{i2\pi}{3}})$	$(-1, e^{-\frac{i\pi}{3}}, e^{-\frac{i2\pi}{3}})$	$(-1, e^{\frac{i2\pi}{3}}, e^{\frac{i\pi}{3}})$	$(1, e^{-\frac{i\pi}{3}}, e^{\frac{i\pi}{3}})$
$\Gamma_{4,1}$	(1, 0, 0) (0, 1, 0) (0, 0, 1)	(1, 0, 0) (0, 1, 0) (0, 0, 1)	(1, 0, 0) (0, 1, 0) (0, 0, 1)	((1, 0, 0) (0, 1, 0) (0, 0, 1)
$\Gamma_{4,2}$	(1, 0, 0) (0, 1, 0) (0, 0, 1)	(-1, 0, 0) (0, 1, 0) (0, 0, -1)	(1, 0, 0) (0, -1, 0) (0, 0, -1)	(-1, 0, 0) (0, -1, 0) (0, 0, 1)
$\Gamma_{4,3}$	(1, 0, 0) (0, 1, 0) (0, 0, 1)	(1, 0, 0) (0, -1, 0) (0, 0, -1)	(-1, 0, 0) (0, -1, 0) (0, 0, -1)	(-1, 0, 0) (0, 1, 0) (0, 0, 1)

Table 5.1. Directions of the magnetic moments (basis vectors) on different Co atoms [see **Fig. 5.1(a)**] for the allowed spin structures when there is no magnetic superstructure ($k_s = 0$).

	Co1
$\Gamma_2(\text{I})$	$(1, e^{-\frac{i2\pi}{3}}, e^{\frac{i2\pi}{3}})$
$\Gamma_3(\text{I})$	$(1, e^{\frac{i2\pi}{3}}, e^{-\frac{i2\pi}{3}})$

Table 5.2. Directions of the magnetic moments on Group I Co atom for the allowed spin structures when the propagation vector \vec{k}_s is along the [111] direction.

	Co2	Co3	Co4
$\Gamma_{2,1}(\text{II})$	(1,0,0)	$(0, e^{-\frac{i2\pi}{3}}, 0)$	$(0, 0, e^{\frac{i2\pi}{3}})$
$\Gamma_{2,2}(\text{II})$	(0,1,0)	$(0, 0, e^{-\frac{i2\pi}{3}})$	$(e^{\frac{i2\pi}{3}}, 0, 0)$
$\Gamma_{2,3}(\text{II})$	(0,0,1)	$(e^{-\frac{i2\pi}{3}}, 0, 0)$	$(0, e^{\frac{i2\pi}{3}}, 0)$
$\Gamma_{3,1}(\text{II})$	(1,0,0)	$(0, e^{\frac{i2\pi}{3}}, 0)$	$(0, 0, e^{-\frac{i2\pi}{3}})$
$\Gamma_{3,2}(\text{II})$	(0,1,0)	$(0, 0, e^{\frac{i2\pi}{3}})$	$(e^{-\frac{i2\pi}{3}}, 0, 0)$
$\Gamma_{3,3}(\text{II})$	(0,0,1)	$(e^{\frac{i2\pi}{3}}, 0, 0)$	$(0, e^{-\frac{i2\pi}{3}}, 0)$

Table 5.3. Directions of the magnetic moments on Group II Co atom for the allowed spin structures when the propagation vector \vec{k}_s is along the [111] direction.

	Co1 (Co3)	Co2 (Co4)
$\Gamma_{1,2}$	(0,1,0)	(0, $e^{-ika/2}$, 0)
$\Gamma_{1,3}$	(0,0,1)	(0,0, $e^{-ika/2}$)
$\Gamma_{2,2}$	(0,1,0)	(0, $-e^{-ika/2}$, 0)
$\Gamma_{2,3}$	(0,0,1)	(0,0, $-e^{-ika/2}$)

Table 5.4. Directions of the magnetic moments on the Group I (and II) Co atoms for the allowed spin structures when the propagation vector \vec{k} is along the [100] direction.

According to Eq. (5.3), the magnitude of the magnetic part depends on the vector structure factor $\vec{f}_s \equiv \sum_{\vec{u}} \vec{q}_0(\vec{k}, \vec{u}) f(\vec{k}, \vec{u}) e^{i\vec{k} \cdot \vec{u}}$ but not on \vec{k}_s which determines the diffraction angles, as long as the helical period is much larger than one unit cell. In other words, except for the diffraction angles, the magnetic contributions of the helical spin structure and the ferromagnetic spin structure $\Gamma_4(1)$ are expected to be nearly the same [Fig. 5.5]. Therefore, the helical spins whose periods are much larger than the unit cell, also match the experimentally observed magnetic parts.

The result that the zero-field helical propagation vector is along either the [111] or the [001] directions [see Appendix B] is consistent with the micromagnetic analysis in the earlier work[33]. Experimentally, the helical spin structure of B20 magnets, such as MnSi[17] and $\text{Fe}_x\text{Co}_{1-x}\text{Ge}$ [8], has a propagation vector \vec{k}_s along the threefold rotation symmetry axis [111]. Helical propagation vector along [111] and [100] have been reported in B20 FeGe[34] and MnGe[5].

5.3.5 Magnitude of the Magnetic Moment

Once the magnetic and nuclear contributions to the NPD are separated, and the spin structure is known, one can estimate the magnitude of the spin by comparing the magnetic contribution and the nuclear contribution written as

$$F_n^2 = \left| \sum_{\vec{r}} f_n(\vec{k}, \vec{r}) \exp(i\vec{k} \cdot \vec{r}) \right|^2 \quad (5.4).$$

where $f_n(\vec{k}, \vec{r})$ is the isotope-specific nuclear structure form factor. Notice that this is typically not the case for small-angle neutron diffraction that only measures the magnetic contribution[22]. According to Eqs. (5.3) and (5.4), the ratio of the magnetic to the nuclear contribution is, for the ferromagnetic spin structure $\Gamma_{4,1}$ and the helical spin structure, solely determined by the magnitude of the spins (magnetic moments) [30,35], which is found to be $0.3 \pm 0.1 \mu_B/\text{Co}$, where the magnetic contribution is an average for $T < 320$ K.

5.4 Surface Magnetization Probed by XMCD Spectroscopy

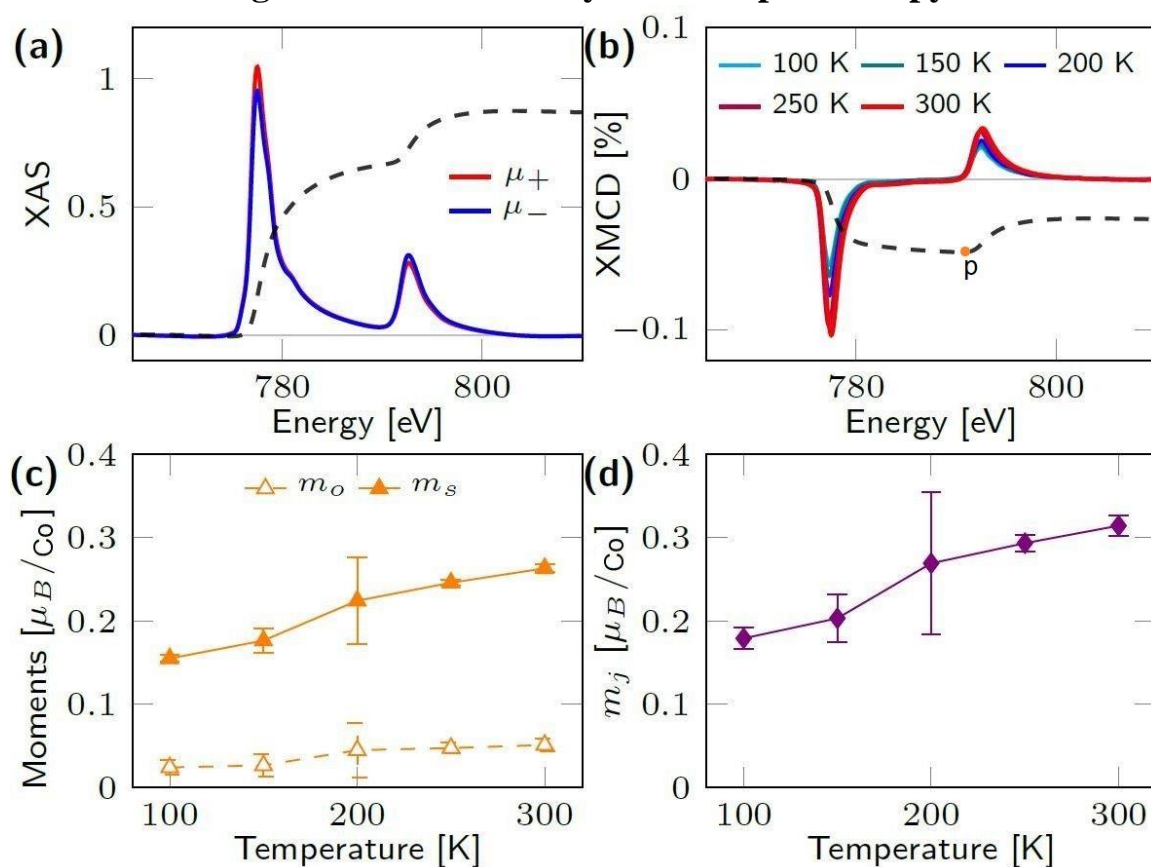


Figure 5.7: (a) X-ray absorption spectra (XAS) measured with left and right circular polarized light at 300 K near Co $L_{3,2}$ edges (2p \rightarrow 3d) and (b) XMCD spectra temperatures for $\text{Co}_{1.043}\text{Si}_{0.957}$. The dashed (black) curves in (a) and (b) correspond to the integrals of room-temperature XAS (r) and XMCD (q) spectra and p is an integral point used for determining spin moment (m_s). (c) Spin and orbital (m_o) moments at different temperatures. (d) Total magnetic moment $m_j = m_o + m_s$.

XAS spectra near the Co $L_{3,2}$ edges (760 – 830 eV) were measured at different temperatures from 100 K to 300 K in an external magnetic field (± 3 kOe) applied normal

to the sample surface. To exclude possible degradation of the free-standing film under the beam, observed in previous experiments, the following temperature series were used: 300, 200, 100, 150, and 250 K. **Figure 5.7(a)** shows the room-temperature XAS spectra for the photon angular momentum parallel (μ_+) and antiparallel (μ_-) to the applied magnetic field. The X-ray magnetic circular dichroism (XMCD) signal is obtained from the difference between the corresponding blue (μ_-) and red (μ_+) curves and is shown for different temperatures in **Fig. 5.7(b)**. The integrals of both XAS and XMCD spectra, $r = \int_{L3+L2}(\mu_+ + \mu_-) d\omega$, $q = \int_{L3+L2}(\mu_+ - \mu_-) d\omega$, and $p = \int_{L3}(\mu_+ - \mu_-) d\omega$, were used to quantify the orbital moment (m_o) and spin moment (m_s) using the sum rule by following $m_o = -\frac{4q}{3r} n_h$ and $m_s = -\frac{6p-4q}{r} n_h$, where n_h is the hole density per Co atom.^{23,24} Orbital and spin moments and average moment $m_j = m_o + m_s$ are shown as a function of temperature in **Figs. 5.7(c) and 5.7(d)**, respectively. The spin and, hence, total magnetic moment increases linearly with temperature from 0.18 to 0.31 μ_B/Co (**Fig. 5.7(d)**), which agrees with the NPD values of $(0.3 \pm 0.1) \mu_B/\text{Co}$. The unusual increase of the magnetic moment with temperature (**Fig. 5.7**) mimics the trend of peak broadening in NPD (see **Fig. 5.3**). It is unclear whether this trend is related to the temperature-dependent transition from helical to skyrmion spin structures around room temperature[26], an interesting aspect that calls for future studies.

5.5 Discussion

The $(0.3 \pm 0.1) \mu_B/\text{Co}$ value extracted from zero-field NPD corresponds to the magnetic moment after accounting for the spin alignment in the magnetic structure. The XMCD values in the range of $(0.18\text{-}0.31) \mu_B/\text{Co}$ are most likely only a small portion of the helical period due to surface sensitivity with a 2-5 nm probing depth. In addition, the weaker coupling of spins at the surface due to a smaller coordination number implies a stronger response to external magnetic fields (larger normal moment), which increases with temperature. Both NPD and XMCD values coincide with density functional theory $(0.18 \mu_B/\text{Co})$ [26] and differ substantially from magnetometry which measures the bulk net magnetization $(0.11 \mu_B/\text{Co}$ at 2 K and $0.07 \mu_B/\text{Co}$ at 300 K)[26]. Magnetometry shows that the field-dependent magnetization curves at 2 K and 300 K do not saturate in fields up to 70 kOe.[26] This is inconsistent with the ferromagnetic ordering since the incomplete saturation cannot be explained by the small magnetocrystalline anisotropies (1.8 and $0.043 \text{ Merg}/\text{cm}^3$ at 2 K and 300 K, respectively).[26] Instead, the slow saturation originates from helimagnetism in the Co-Si alloy, as indicated by DC susceptibility and Lorentz transmission electron microscopy, and the transformation from helical to conical phase at a high magnetic field.

Correlating the experimental with modeled magnetic contributions suggests that both ferromagnetic and helical spin structures (with a period exceeding the size of the unit cell) are most likely (**Fig. 5.5**). According to Eq. (5.3), the information of the helical period or \vec{k}_s is included in the factor $\sum_{\vec{R}} e^{i(\vec{k}_s + \vec{k}) \cdot \vec{R}}$ which determines the diffraction angle. In other words, the helical period may be extracted from the positions of the satellite peaks $\vec{k} \pm \vec{k}_s$ in neutron diffraction. Unfortunately, broadening effects due to chemical disorder and

multiple values of $|\vec{k} \pm \vec{k}_s|$ smear the satellite peaks, which prevent us from identifying satellite peaks in the powder neutron diffraction patterns. If satellite peaks are not observed due to the broadening of the main peaks, we can put a lower limit of helical period which is 120 nm.

5.6 Summary

In summary, the results of NPD measurements on $\text{Co}_{0.043}\text{Si}_{0.957}$ are consistent with the helical spin structure. The magnitude of the magnetic moment extracted from NPD ($0.3 \pm 0.1 \mu_{\text{B}}/\text{Co}$) coincides with theoretical estimates ($0.18 \mu_{\text{B}}/\text{Co}$) and the surface magnetization retrieved from XMCD spectroscopy ($0.18 - 0.31 \mu_{\text{B}}/\text{Co}$). All these values are substantially larger than the magnetometry value ($0.11 \mu_{\text{B}}/\text{Co}$), the data reflect the evolution of a coplanar helical spin structure into a noncoplanar conical spin structure with nonzero magnetization. The smaller magnetic moment measured by magnetometry suggests that the external field produced by magnetometry is not enough to get fully aligned spins in $\text{Co}_{0.043}\text{Si}_{0.957}$, which is exactly the behavior of helical spin.

References

- [1] Anisimov V I, Hlubina R, Korotin M A, Mazurenko V V, Rice T M, Shorikov A O and Sigrist M 2002 First-Order Transition between a Small Gap Semiconductor and a Ferromagnetic Metal in the Isoelectronic Alloy $\text{FeSi}_{1-x}\text{Ge}_x$ *Phys. Rev. Lett.* **89** 257203
- [2] Jeong T and Pickett W E 2004 Implications of the B20 crystal structure for the

magneto-electronic structure of MnSi *Phys. Rev. B - Condens. Matter Mater. Phys.* **70** 075114

- [3] Beille J, Voiron J and Roth M 1983 Long period helimagnetism in the cubic B20 $\text{Fe}_x\text{Co}_{1-x}\text{Si}$ and $\text{Co}_x\text{Mn}_{1-x}\text{Si}$ alloys *Solid State Commun.* **47** 399–402
- [4] Beille J, Voiron J, Towfiq F, Roth M and Zhang Z Y 1981 Helimagnetic structure of the $\text{Fe}_x\text{Co}_{1-x}\text{Si}$ alloys *J. Phys. F Met. Phys.* **11** 2153–60
- [5] Kanazawa N, Onose Y, Arima T, Okuyama D, Ohoyama K, Wakimoto S, Kakurai K, Ishiwata S and Tokura Y 2011 Large topological hall effect in a short-period helimagnet MnGe *Phys. Rev. Lett.* **106** 156603
- [6] Bauer A, Neubauer A, Franz C, Münzer W, Garst M and Pfleiderer C 2010 Quantum phase transitions in single-crystal $\text{Mn}_{1-x}\text{Fe}_x\text{Si}$ and $\text{Mn}_{1-x}\text{Co}_x\text{Si}$: Crystal growth, magnetization, ac susceptibility, and specific heat *Phys. Rev. B* **82** 64404
- [7] Zheng F, Rybakov F N, Borisov A B, Song D, Wang S, Li Z A, Du H, Kiselev N S, Caron J, Kovács A, Tian M, Zhang Y, Blügel S and Dunin-Borkowski R E 2018 Experimental observation of chiral magnetic bobbars in B20-type FeGe *Nat. Nanotechnol.* **13** 451–5
- [8] Spencer C S, Gayles J, Porter N A, Sugimoto S, Aslam Z, Kinane C J, Charlton T R, Freimuth F, Chadov S, Langridge S, Sinova J, Felser C, Blügel S, Mokrousov Y and Marrows C H 2018 Helical magnetic structure and the anomalous and topological Hall effects in epitaxial B20 $\text{Fe}_{1-y}\text{Co}_y\text{Ge}$ films *Phys. Rev. B* **97** 214406
- [9] Dzyaloshinsky I 1958 A thermodynamic theory of “weak” ferromagnetism of antiferromagnetics *J. Phys. Chem. Solids* **4** 241–55

- [10] Moriya T 1960 Anisotropic superexchange interaction and weak ferromagnetism *Phys. Rev.* **120** 91–8
- [11] Rao Z, Li H, Zhang T, Tian S, Li C, Fu B, Tang C, Wang L, Li Z, Fan W, Li J, Huang Y, Liu Z, Long Y, Fang C, Weng H, Shi Y, Lei H, Sun Y, Qian T and Ding H 2019 Observation of unconventional chiral fermions with long Fermi arcs in CoSi *Nature* **567** 496–9
- [12] Sanchez D S, Belopolski I, Cochran T A, Xu X, Yin J-X, Chang G, Xie W, Manna K, Süß V, Huang C-Y, Alidoust N, Multer D, Zhang S S, Shumiya N, Wang X, Wang G-Q, Chang T-R, Felser C, Xu S-Y, Jia S, Lin H and Hasan M Z 2019 Topological chiral crystals with helicoid-arc quantum states *Nature* **567** 500–5
- [13] Wilde M A, Dodenhöft M, Niedermayr A, Bauer A, Hirschmann M M, Alpin K, Schnyder A P and Pfleiderer C 2021 Symmetry-enforced topological nodal planes at the Fermi surface of a chiral magnet *Nature* **594** 374–9
- [14] Li H, Xu S, Rao Z-C, Zhou L-Q, Wang Z-J, Zhou S-M, Tian S-J, Gao S-Y, Li J-J, Huang Y-B, Lei H-C, Weng H-M, Sun Y-J, Xia T-L, Qian T and Ding H 2019 Chiral fermion reversal in chiral crystals *Nat. Commun.* **10** 5505
- [15] Ni Z, Wang K, Zhang Y, Pozo O, Xu B, Han X, Manna K, Paglione J, Felser C, Grushin A G, de Juan F, Mele E J and Wu L 2021 Giant topological longitudinal circular photo-galvanic effect in the chiral multifold semimetal CoSi *Nat. Commun.* **12** 154
- [16] Neubauer A, Pfleiderer C, Binz B, Rosch A, Ritz R, Niklowitz P G and Böni P

- 2009 Topological hall effect in the a phase of MnSi *Phys. Rev. Lett.* **102** 186602
- [17] Mühlbauer S, Binz B, Jonietz F, Pfleiderer C, Rosch A, Neubauer A, Georgii R and Böni P 2009 Skyrmion Lattice in a Chiral Magnet *Science*. **323** 915 LP – 919
- [18] Binz B, Vishwanath A and Aji V 2006 Theory of the helical spin crystal: A candidate for the partially ordered state of MnSi *Phys. Rev. Lett.* **96** 207202
- [19] Takeda M, Endoh Y, Kakurai K, Onose Y, Suzuki J and Tokura Y 2009 Nematic-to-smectic transition of magnetic texture in conical state *J. Phys. Soc. Japan* **78** 093704
- [20] Takizawa H, Sato T, Endo T and Shimada M 1988 High-pressure synthesis and electrical and magnetic properties of MnGe and CoGe with the cubic B20 structure *J. Solid State Chem.* **73** 40–6
- [21] Yamada H, Terao K, Ohta H and Kulatov E 2003 Electronic structure and magnetism of FeGe with B20-type structure *Phys. B Condens. Matter* **329–333** 1131–3
- [22] Lebech B, Bernhard J and Freltoft T 1989 Magnetic structures of cubic FeGe studied by small-angle neutron scattering *J. Phys. Condens. Matter* **1** 6105–22
- [23] DiTusa J F, Zhang S B, Yamaura K, Xiong Y, Prestigiacomo J C, Fulfer B W, Adams P W, Brickson M I, Browne D A, Capan C, Fisk Z and Chan J Y 2014 Magnetic, thermodynamic, and electrical transport properties of the noncentrosymmetric B20 germanides MnGe and CoGe *Phys. Rev. B* **90** 144404
- [24] Grigoriev S V., Siegfried S A, Altynbayev E V., Potapova N M, Dyadkin V, Moskvina E V., Menzel D, Heinemann A, Axenov S N, Fomicheva L N and

- Tsvyashchenko A V. 2014 Flip of spin helix chirality and ferromagnetic state in $\text{Fe}_{1-x}\text{Co}_x\text{Ge}$ compounds *Phys. Rev. B - Condens. Matter Mater. Phys.* **90** 174414
- [25] Streubel R, Bouma D S, Bruni F, Chen X, Ercius P, Ciston J, N'Diaye A T, Roy S, Kevan S D, Fischer P and Hellman F 2021 Chiral Spin Textures in Amorphous Iron–Germanium Thick Films *Adv. Mater.* **33** 2004830
- [26] Balasubramanian B, Manchanda P, Pahari R, Chen Z, Zhang W, Valloppilly S R, Li X, Sarella A, Yue L, Ullah A, Dev P, Muller D A, Skomski R, Hadjipanayis G C and Sellmyer D J 2020 Chiral Magnetism and High-Temperature Skyrmions in B20-Ordered Co-Si *Phys. Rev. Lett.* **124** 57201
- [27] Turgut E, Park A, Nguyen K, Moehle A, Muller D A and Fuchs G D 2017 Chiral magnetic excitations in FeGe films *Phys. Rev. B* **95** 134416
- [28] Stöhr Siegmund, Hans-Christoph, J 2006 *Magnetism from fundamentals to nanoscale dynamics* (Springer)
- [29] Rodríguez-Carvajal J 1993 Recent advances in magnetic structure determination by neutron powder diffraction *Phys. B Phys. Condens. Matter* **192** 55–69
- [30] Squires G L 2013 Introduction to the theory of thermal neutron scattering
- [31] Xu X, Zhang X, Yin Y, Balasubramanian B, Das B, Liu Y, Huq A and Sellmyer D J 2017 Anti-site mixing and magnetic properties of $\text{Fe}_3\text{Co}_3\text{Nb}_2$ studied via neutron powder diffraction *J. Phys. D. Appl. Phys.* **50** 25002
- [32] Kovalev O V, Stokes H T and Hatch D M 1993 *Representations of the crystallographic space groups : irreducible representations, induced representations, and corepresentations* (Yverdon, Switzerland; Langhorne, Pa.:

Gordon and Breach)

- [33] Bak P and Jensen M H 1980 Theory of helical magnetic structures and phase transitions in MnSi and FeGe *J. Phys. C Solid State Phys.* **13** L881–5
- [34] Uchida M, Nagaosa N, He J P, Kaneko Y, Iguchi S, Matsui Y and Tokura Y 2008 Topological spin textures in the helimagnet FeGe *Phys. Rev. B* **77** 184402
- [35] Wang H, Balasubramanian B, Pahari R, Skomski R, Liu Y, Huq A, Sellmyer D J and Xu X 2019 Noncollinear spin structure in $\text{Fe}_{3+x}\text{Co}_{3-x}\text{Ti}_2$ ($x=0,2,3$) from neutron diffraction *Phys. Rev. Mater.* **3** 064403

Chapter VI: Conclusion and Outlook

This dissertation focuses on understanding and improving the magnetic properties of rare-earth-free magnetic material. The intermetallic magnet alloys are synthesized by arc melting and melt-spinning. The crystal and magnetic properties are analyzed by X-ray diffraction, neutron diffraction, and superconducting quantum interference device.

The magnetic anisotropy of rare-earth-free magnets is one of the significant concerns compared to rare-earth magnetics like $\text{Nd}_2\text{Fe}_{14}\text{B}$ and $\text{Sm}_2\text{Co}_{17}$. In chapter III, we analyze the polycrystalline Fe-Co-Ti spin structure by neutron powder diffraction. The noncollinear spin structure comes from the random-anisotropy effect, leading to a K_1 distribution. This effect increases the boundary region between magnetic domains, which is visible on a scale of 40 nm. In chapter VI, we doped boron inside the Fe_2Ni compound to increase the magnetic anisotropy of Fe-Ni alloys. We saw a significant increase in anisotropy energy for $\text{Fe}_4\text{Ni}_2\text{B}$ alloys. We explain the large anisotropy in $\text{Fe}_4\text{Ni}_2\text{B}$ as the structure difference compared to Fe_2Ni induced by the strong metal-boron bonds.

The spin structure is also important in magnetic materials. In chapter V, we investigate the spin structure of Co-Si, which is famous for its B20 structure. We found that replacing a small amount of Si with Co, $\text{Co}_{1.043}\text{Si}_{0.957}$ shows a helical spin structure different from CoSi with diamagnetism.

So far, we have studied three kinds of rare-earth magnetic with magnetic anisotropy and spin structure topics. However, there is yet any rare-earth-free magnetic that can replace $\text{Nd}_2\text{Fe}_{14}\text{B}$ or $\text{Sm}_2\text{Co}_{17}$. The effort to find suitable substitutes is still needed in the future.

Appendix A: Magnetism of Cobalt-Nitride Measured by Neutron

Diffraction

This appendix discusses the thin-film neutron diffraction of $\text{Co}_{0.3}\text{N}$ deposited on Si substrate, which is done in DEMAND beamline in Oak Ridge National Laboratory.

A.1 Introduction

New materials discovery has governed the development of science and technology for decades.[1–3] Many of the most important magnetic materials were discovered through enlightened solid-state chemistry and intermetallic-compound research.[4–6] This approach often has been focused on Fe or Co-based compounds since Fe and/or Co are required to achieve high saturation magnetic polarization J_s ($J_s = 4\pi M_s$, where M_s is the saturation magnetization) and Curie temperature (T_c). Magnetic anisotropy is another fundamental intrinsic property, essential to develop coercivity ($B_c = \mu_0 H_c$) in magnetic materials or thermal stability in nanomagnets. Magnetocrystalline anisotropy is a combined effect of spin-orbit coupling and crystal-field interactions and often requires rare-earth or expensive elements.[7] In contrast to the earlier methods, there are three relatively unexplored approaches to the problem of new magnetic-materials discovery. These include (i) the production of new structures by incorporation of gases such as nitrogen, (ii) the use of non-equilibrium methods to generate novel structures, and (iii) the use of high-speed computational methods stimulated by the materials genome initiative. In this research, we combine uniquely all of these approaches to achieve promising magnetic properties in Co-N compounds.

Considering the above-mentioned three approaches separately, it has been shown that the interstitial modification of N can improve the M_s , K_1 , and T_c values of Fe-rich magnetic materials such as Fe_{16}N_2 and $\text{Sm}_2\text{Fe}_{17}\text{N}_3$. [8] Some stoichiometric Co-N interstitial compounds have been reported such as Co_3N and Co_2N , but these exhibit poor magnetic properties. [9–11] An example is the hexagonal compound Co_3N , which crystallizes in the well-known ϵ - Fe_3N structure (space group $P6_322$) but exhibits a low magnetization (about 31 kA/m or 31 emu/cm³) at 5K. [9] The second approach that of non-equilibrium processing has focused on techniques such as sputtering and rapid quenching from the melt. These methods have produced interesting examples of magnetic compounds such as Co_3Si by sputtering [12] and TbCu_7 and ThMn_{12} -type structures by rapid quenching. [13–15] Finally, theoretical and computational tools for new materials discovery have significantly developed in recent years. First-principal calculations and machine-learning techniques show much potential for high-throughput computational materials design. Ideally, this approach can accelerate the discovery of new materials with high efficiency and speed by guiding synthesis methods on the composition and structure of new compounds. Several reviews of advances in this rapidly developing field have appeared recently. [16–21]

Transition-metal nitrides form a rich class of compounds with diverse electronic structures and properties. They are relatively unexplored compounds compared to oxides, yet they have properties ranging from metallic to semiconducting, with potential applications such as ceramics, magnets, catalysis, and others. [22–26] Nanoparticle syntheses have recently shown great potential for developing new Co-rich magnetic compounds with high magnetocrystalline anisotropy and magnetization. [12,27–30] In this

chapter, we investigate the magnetic property of new Co_3N compounds by neutron diffraction.

A.2 Experiment Details

Our nanoparticle experiments were carried out by cluster deposition using an inert-gas condensation.[12] In this method, which produces highly monodisperse metal and alloy nanoparticles, an atomic Co vapor produced using direct-current plasma sputtering is condensed in a cooled inert-gas atmosphere to form nanoparticles in the gas-aggregation chamber. To form Co_3N nanoparticles, we have fed nitrogen gas (N_2) into the gas-aggregation chamber. Stoichiometry and crystal structure was controlled by nitrogen flow rate, deposition pressure, and growth rate. The nanoparticles were then extracted from the gas-aggregation chamber to another chamber for room-temperature deposition on substrates. Dense nanoparticle films were deposited on Si (111) to measure x-ray diffraction (XRD) using a $\text{Cu K}\alpha$ wavelength of about 1.54 Å and magnetic properties using SQUID. Neutron diffraction was performed in the DEMAND beamline in Oak Ridge National Laboratory.

A.3 Crystal Structure of Co-N

Fig. A.1(A) shows the experimental XRD patterns for the nanoparticle samples prepared at different N_2 flow rates in standard cubic centimeters per minute (SCCM). Without the addition of N_2 into the gas-aggregation chamber, the sputtered Co atoms aggregate to form pure Co nanoparticles, which exhibit a mixture of hcp and fcc Co phases

as indexed in black and green fonts, respectively, in the XRD pattern (black curve in **Fig. A.1(A)**). At N_2 flow rates of about 25 SCCM (red curve) and 30 SCCM (blue curve), the XRD patterns of the nanoparticles are different from that of the Co nanoparticles (black curve) and existing equilibrium phases in the Co-N binary phase diagram,[31] and indicate the formation of new structures. Higher nitrogen flow rates cause the nanoparticles to crystallize in zincblende-type cubic CoN, as exemplified by the XRD pattern for 100 sccm (brown curve in **Fig. A.1(A)**). Crystal structures of the new cobalt nitrides were searched using the adaptive genetic algorithm [26,32,33], which was developed based on real-space cut-and-paste operations to generate descendent structures.[34] The searches were carried out at zero pressure and zero temperature with energy as the selection criteria to optimize the candidate structures. Out of several calculated structures, XRD patterns of the nanoparticles prepared at 25 SCCM (red curve) and 30 SCCM (blue curve) can be indexed with the new hexagonal (space group: $P63/mmc$, prototype: $CdMg_3$) and rhombohedral (space group: $R3c$) Co_3N structures, respectively. XPS results also show the Co/N atomic ratio for the hexagonal and rhombohedral nanoparticles as 3.3 and 2.8, respectively, and the corresponding stoichiometric values will be used while discussing the hexagonal and rhombohedral nanoparticles. While the rhombohedral-type $Co_{2.8}N$ nanoparticles are single-phase, the XRD pattern of the substituted hexagonal $Co_{3.3}N$ nanoparticles exhibits a low-intensity (111) peak corresponding to fcc Co.

We also have performed XRD profile analysis for the nanoparticles using the Rietveld refinement method, as shown in **Fig. A.1(B)**. The experimental XRD patterns of the nanoparticle samples prepared at the nitrogen flow rates of 25 and 30 SCCM are in good agreement with the simulated XRD patterns for the hexagonal and rhombohedral-

type Co_3N structures, respectively. Rietveld refinement yields a volume fraction of 3% fcc Co, as well as lattice parameters of $a = 5.042 \text{ \AA}$ and $c = 4.090 \text{ \AA}$ (hexagonal phase) and $a = 4.611 \text{ \AA}$ and $c = 13.062 \text{ \AA}$ (rhombohedral).

Note that the rhombohedral structure is an interstitial type, and the hexagonal Co_3N phase is a substitutional compound. **Fig. A.1(C-D)** shows the corresponding unit cells. In the rhombohedral structure, the nitrogen atoms form a sublattice by occupying some octahedral interstitial sites in the hcp-Co host lattice. The substituted hexagonal compound crystallizes in the CdMg_3 -type hexagonal structure. As in the rhombohedral structure, the nitrogen atoms form an ordered sublattice, corresponding to the Cd atoms in the prototype, but the structure is that of hcp cobalt, where one-fourth of the Co atoms are replaced by nitrogen.

As compared to hcp Co and fcc Co, the rhombohedral $\text{Co}_{2.8}\text{N}$ nanoparticles have several distinct and intense x-ray diffraction peaks at $2\theta = 39.12^\circ, 58.32^\circ, 70.89^\circ, 77.79^\circ, 85.23^\circ$ and 87.58° , corresponding to (110), (116), (030), (119), (306), and (223) reflections, respectively (blue curve in **Fig. A.1(A)**). On the other hand, it is important during the structural determination of $\text{Co}_{3.3}\text{N}$ nanoparticles using XRD to properly distinguish between the hcp Co and substituted CdMg_3 -type structures, which are closely related and have similar XRD patterns. The main difference is the larger unit cell, which means that hcp ($h k l$) peaks correspond to CdMg_3 ($2h 2k l$) peaks. A few distinct XRD peaks at lower angles from (100), (101), and (110) reflections are expected for the CdMg_3 -type structure, but the intensities of (100) and (110) peaks are small as compared to the intense XRD peaks such as (200), (002), and (201) and the substrate peak covers the (101) peak. However, a weak intensity peak corresponding to the (100) reflection of the CdMg_3 -type structure is

visible in the experimental XRD pattern (red curve in **Fig. A.1(A) and (B)**). Note that the intensity ratio between the (100) and (200) reflections from the experimental XRD pattern is $I(100)/I(200) \approx 0.58$, comparable with the standard theoretical intensity ratio $I(100)/I(200) = 0.37$ for $\text{Co}_{3.3}\text{N}$ nanoparticles with the CdMg_3 -type structure. In support of this result, the analysis of the intensity of the (002) XRD peak and electron diffraction results also indicates that the hexagonal phase is CdMg_3 , not the crystallographically very similar hcp Co; in addition, XPS measurements also show that the stoichiometry is close to Co_3N (see below)

Note that the (002) peak often has been observed to be the most intense XRD peak for hcp Co nanoparticles,[35–39] and this is also true for the pure Co nanoparticles reported in the present study (black curve in **Fig. A.1(A)**). In contrast, the most intense diffraction peak in the XRD pattern of the hexagonal $\text{Co}_{3.3}\text{N}$ nanoparticles is (201) as expected for the CdMg_3 -type structure.

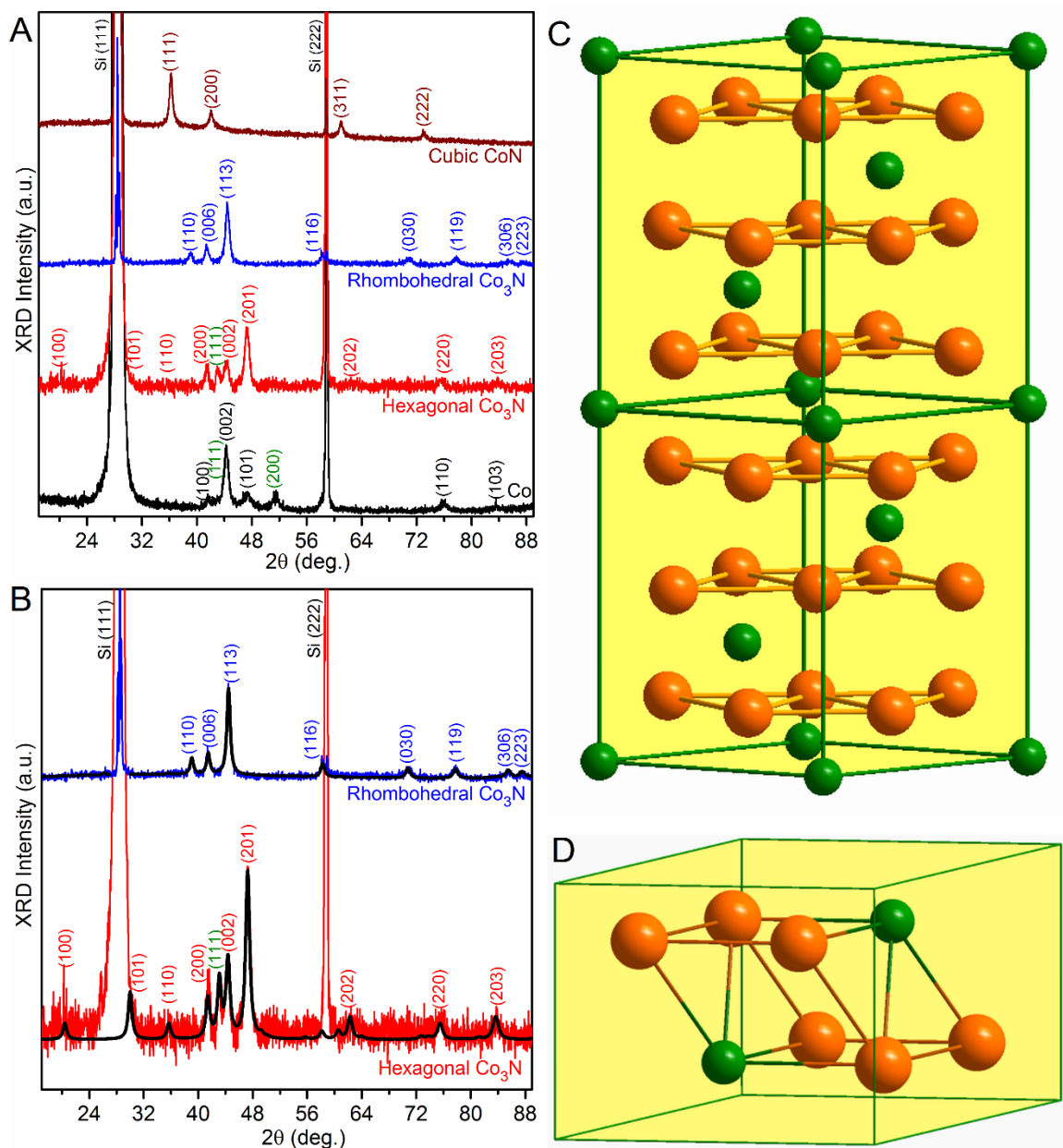


Figure. A.1 XRD patterns: (A) The experimental patterns measured using $\text{Cu K}\alpha$ wavelength of about 1.54 \AA for the nanoparticles prepared at different N_2 flow rates: Co (0 SCCM), hexagonal Co_3N (25 SCCM), rhombohedral Co_3N (30 SCCM), and cubic CoN (100 SCCM). (B) The experimental patterns of the hexagonal (red) and rhombohedral (blue) nanoparticles are fitted with the corresponding structures using Rietveld analysis (black curve). New Co_3N structures: (C) Rhombohedral and (D) CdMg_3 -type hexagonal.

A.4 Neutron Diffraction of $\text{Co}_{3.3}\text{N}$

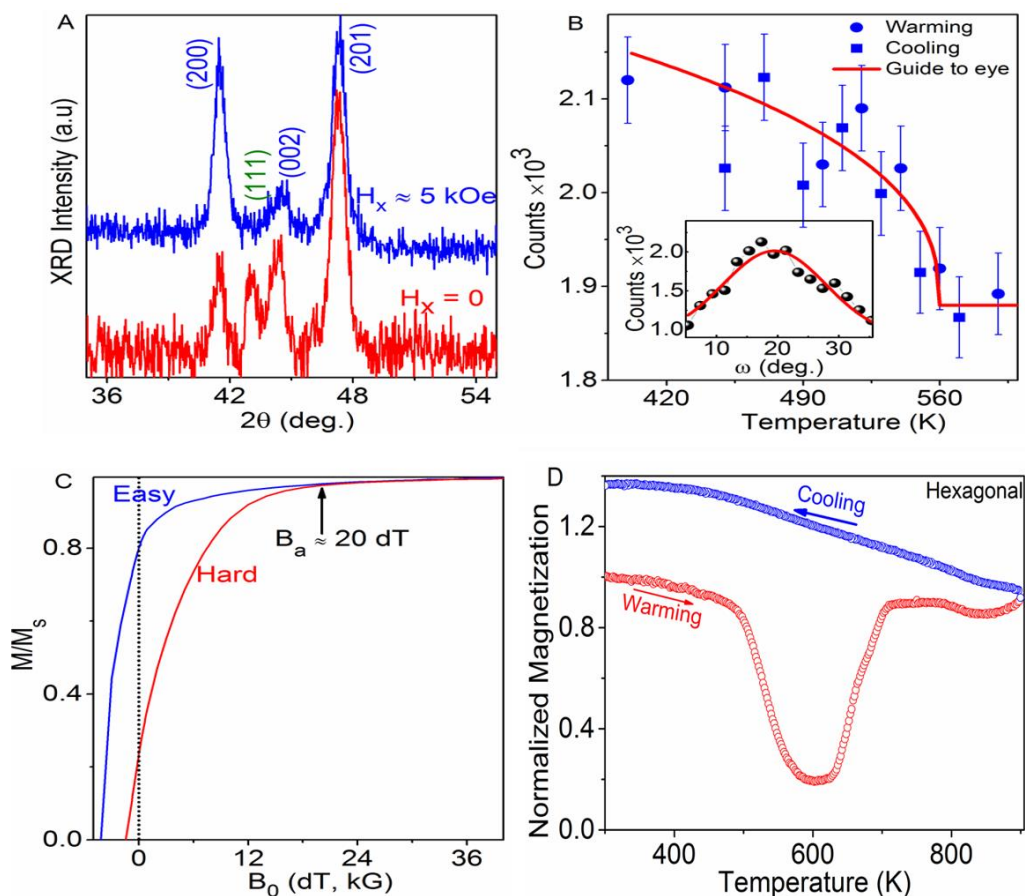


Figure A.2: Easy-axis aligned hexagonal-type $\text{Co}_{3.3}\text{N}$ nanoparticles: (A) Out-of-plane XRD patterns measured for the unaligned (red curve) and aligned (blue curve) samples. The XRD patterns are indexed to the CdMg₃-type hexagonal structure. (B) Neutron diffraction intensity of the (002) peak for the aligned nanoparticle film shows a transition for both warming (circle) and cooling (square) between 500 K and 600 K, whereas the red line is a guide to the eye. The inset shows the rocking curve of the (002) peak, whereas the red line is the Gaussian fit to the data. (C) Magnetic hysteresis loops measured at 10 K along the easy (x) and hard (y) axes. The anisotropy field $B_a \equiv \mu_0 H_a$ is indicated by an arrow. (D) Magnetization was measured as a function of temperature for the hexagonal $\text{Co}_{3.3}\text{N}$ nanoparticles in a magnetic field of 1.0 dT (1.0 kG) during warming (red curve) and cooling (blue curve). The magnetization is normalized with the room-temperature value. The depth of warming curve means a transition temperature around 600K.

To study the magnetic transition and phase stability of the hexagonal $\text{Co}_{3.3}\text{N}$ nanoparticles, we performed neutron diffraction on a thin-film sample composed of easy-axis-aligned hexagonal $\text{Co}_{3.3}\text{N}$ nanoparticles. The nanoparticles were aligned by applying a magnetic field parallel to the substrate during the deposition, i.e., the field was applied along the x-direction with respect to the substrate. **Fig. A.2(A)** compares the out-of-plane (z-axis) XRD patterns of the unaligned (isotropic) and aligned nanoparticles. It is clearly seen that the intensity of the (002) peak significantly decreases and that of the (200) peak increases in the XRD pattern of the aligned nanoparticles as compared to those corresponding intensities in the XRD pattern of the isotropic nanoparticles. This result indicates that the c-axis of the hexagonal Co_3N crystal is the easy direction for magnetization and is aligned along the direction of the magnetic field H_x , which is applied along the substrate plane during the deposition.

Generally, neutron diffraction consists of nuclear and magnetic contributions. Nuclear diffraction measures the ordering of atoms; it is more sensitive to N than to Co because the scattering length of N is about 3 times as large as Co.[40] On the other hand, magnetic diffraction measures the ordering of magnetic moments. The important result is that the temperature dependence of the (002) diffraction intensity shows a clear transition between 500 K and 600 K, as shown in **Fig. A.2(B)**, and this transition appears to be reversible (warming followed by cooling). Since neutron diffraction is sensitive to N, our result indicates that the structural decomposition of $\text{Co}_{3.3}\text{N}$ nanoparticles in terms of N loss is minimal up to 600 K. The transition observed between 500 and 600 K in **Fig. A.2(B)** is consistent with the magnetic transition shown by the temperature-dependent magnetization curve (**Fig. A.2(D)**). Therefore, there is a sizable magnetic contribution to the neutron

diffraction, which suggests a magnetic ordering. One can observe the magnetic transition in the (002) diffraction indicates a non-zero magnetic moment perpendicular to the c axis, which could be due to the exchange interaction between the partially aligned particles.[41]

As shown in the inset of **Fig. A.2(B)**, the rocking curve of (002) diffraction was measured to study the relation between the crystalline direction and the substrate orientation as well as to obtain the degree of magnetic alignment from the distribution of (002) intensity. The crystalline c axis appears to be closely aligned with the substrate plane in which the magnetic field was applied during the growth, with a 20-degree FWHM (full width at half maximum) angular dispersion. Rocking scans performed by the 4-circle neutron diffractometer probe the distribution of magnetic moment and (002) orientation.

A.5 Summary

The anisotropy of the hexagonal $\text{Co}_{3.3}\text{N}$ nanoparticles is in the range of several rare-earth-free permanent-magnet materials that have shown high coercivities and room-temperature energy products upon nanostructuring.[27,42,43] Therefore, they can have potential uses in microelectromechanical systems (MEMS) and also can be used to create future rare-earth-free permanent magnets, if scale-up methods are developed. X-ray and neutron diffraction shows that $\text{Co}_{3.3}\text{N}$ aligns well by applying a magnetic field parallel to the substrate during the deposition.

Reference

- [1] Stefano S, Corey O, Junkai X, Anurag T, Mario Z, Thomas A, Pelin T, Munuswamy V, Michael C and Stefano C 2017 Accelerated discovery of new magnets in the Heusler alloy family *Sci. Adv.* **3** e1602241
- [2] Collins C, Dyer M S, Pitcher M J, Whitehead G F S, Zanella M, Mandal P, Claridge J B, Darling G R and Rosseinsky M J 2017 Accelerated discovery of two crystal structure types in a complex inorganic phase field. *Nature* **546** 280–4
- [3] Vogel E 2007 Technology and metrology of new electronic materials and devices *Nat. Nanotechnol.* **2** 25–32
- [4] Strnat K, Hoffer G, Olson J, Ostertag W and Becker J J 1967 A Family of New Cobalt-Base Permanent Magnet Materials *J. Appl. Phys.* **38** 1001–2
- [5] Sagawa M, Fujimura S, Togawa N, Yamamoto H and Matsuura Y 1984 New material for permanent magnets on a base of Nd and Fe *J. Appl. Phys.* **55** 2083–7
- [6] Takahashi M, Shoji H, Takahashi H, Nashi H, Wakiyama T, Doi M and Matsui M 1994 Magnetic moment of α'' -Fe₁₆N₂ films *J. Appl. Phys.* **76** 6642–7
- [7] Skomski R and Sellmyer D J 2009 Anisotropy of rare-earth magnets *J. Rare Earths* **27** 675–9
- [8] Coey J M D and Sun H 1990 Improved magnetic properties by treatment of iron-based rare earth intermetallic compounds in ammonia *J. Magn. Magn. Mater.* **87** L251–4
- [9] Widenmeyer M, Shlyk L, Becker N, Dronskowski R, Meissner E and Niewa R

- 2016 Synthesis of Metastable Co_4N , Co_3N , Co_2N , and $\text{CoO}_{0.74}\text{N}_{0.24}$ from a Single Azide Precursor and Intermediates in CoBr_2 Ammonolysis *Eur. J. Inorg. Chem.* **2016** 4792–801
- [10] Lourenço M B, Carvalho M D, Fonseca P, Gasche T, Evans G, Godinho M and Cruz M M 2014 Stability and magnetic properties of cobalt nitrides *J. Alloys Compd.* **612** 176–82
- [11] Suzuki K, Kaneko T, Yoshida H, Morita H and Fujimori H 1995 Crystal structure and magnetic properties of the compound CoN *J. Alloys Compd.* **224** 232–6
- [12] Balasubramanian B, Manchanda P, Skomski R, Mukherjee P, Valloppilly S R, Das B, Hadjipanayis G C and Sellmyer D J 2016 High-coercivity magnetism in nanostructures with strong easy-plane anisotropy *Appl. Phys. Lett.* **108** 152406
- [13] Feng D Y, Liu Z W, Zheng Z G, Zeng D C and Zhang G Q 2013 The structure, anisotropy and coercivity of rapidly quenched TbCu_7 -type $\text{SmCo}_{7-x}\text{Zr}_x$ alloys and the effects of post-treatments *J. Magn. Magn. Mater.* **347** 18–25
- [14] Gabay A M and Hadjipanayis G C 2016 ThMn_{12} -type structure and uniaxial magnetic anisotropy in $\text{ZrFe}_{10}\text{Si}_2$ and $\text{Zr}_{1-x}\text{Ce}_x\text{Fe}_{10}\text{Si}_2$ alloys *J. Alloys Compd.* **657** 133–7
- [15] Zhang Z D, Liu W, Liu J P and Sellmyer D J 2000 Metastable phases in rare-earth permanent-magnet materials *J. Phys. D: Appl. Phys.* **33** R217–46
- [16] Nosengo N and Ceder G 2016 Can artificial intelligence create the next wonder material? *Nature* **533** 22–5

- [17] Raccuglia P, Elbert K C, Adler P D F, Falk C, Wenny M B, Mollo A, Zeller M, Friedler S A, Schrier J and Norquist A J 2016 Machine-learning-assisted materials discovery using failed experiments. *Nature* **533** 73–6
- [18] Jain A, Shin Y and Persson K A 2016 Computational predictions of energy materials using density functional theory *Nat. Rev. Mater.* **1** 15004
- [19] Chris-Kriton S 2016 A benchmark for materials simulation *Science*. **351** 1394–5
- [20] Kurt L, Gustav B, Torbjörn B, Peter B, Stefan B, Volker B, Damien C, E. C I, J. C S, Andrea D C, Stefano de G, Thierry D, Kay D J, Igor D M, Claudia D, Marcin D, Olle E, A. F-L J, F. G K, Luigi G, Paolo G, Matteo G, Stefan G, Xavier G, Oscar G, U. G E K, Andris G, François G, R. H D, J. H P, W. H N A, Diana I, B. J D, François J, Daniel J, Georg K, Klaus K, Emine K, O. K Y, M. L I L, Sven L, Martijn M, Nicola M, Ulrike N, Lars N, Taisuke O, Lorenzo P, J. P C, Ward P, J. P M I, Keith R, Manuel R, Gian-Marco R, Santanu S, Matthias S, Martin S, Karlheinz S, Sangeeta S, Francesca T, Patrik T, Alexandre T, Marc T, David V, J. van S M, Veronique V S, M. W J, R. Y J, Guo-Xu Z and Stefaan C 2016 Reproducibility in density functional theory calculations of solids *Science*. **351** aad3000
- [21] Curtarolo S, Hart G L W, Nardelli M B, Mingo N, Sanvito S and Levy O 2013 The high-throughput highway to computational materials design. *Nat. Mater.* **12** 191–201
- [22] Sun W, Holder A, Orvañanos B, Arca E, Zakutayev A, Lany S and Ceder G 2017 Thermodynamic Routes to Novel Metastable Nitrogen-Rich Nitrides *Chem. Mater.*

29 6936–46

- [23] Peng Z, Liang J, Fan W, Kejian D, Kangle L and Zehui Z 2017 High performance of a cobalt–nitrogen complex for the reduction and reductive coupling of nitro compounds into amines and their derivatives *Sci. Adv.* **3** e1601945
- [24] Crowhurst J C, Goncharov A F, Sadigh B, Evans C L, Morrall P G, Ferreira J L and Nelson A J 2006 Synthesis and characterization of the nitrides of platinum and iridium *Science* **311** 1275–8
- [25] Young A F, Sanloup C, Gregoryanz E, Scandolo S, Hemley R J and Mao H 2006 Synthesis of Novel Transition Metal Nitrides IrN₂ and OsN₂ *Phys. Rev. Lett.* **96** 155501
- [26] Zhao X, Nguyen M C, Zhang W Y, Wang C Z, Kramer M J, Sellmyer D J, Li X Z, Zhang F, Ke L Q, Antropov V P and Ho K M 2014 Exploring the Structural Complexity of Intermetallic Compounds by an Adaptive Genetic Algorithm *Phys. Rev. Lett.* **112** 45502
- [27] Balasubramanian B, Mukherjee P, Skomski R, Manchanda P, Das B and Sellmyer D J 2014 Magnetic nanostructuring and overcoming Brown's paradox to realize extraordinary high-temperature energy products *Sci. Rep.* **4** 6265
- [28] Harris V G, Chen Y, Yang A, Yoon S, Chen Z, Geiler A L, Gao J, Chinnasamy C N, Lewis L H, Vittoria C, Carpenter E E, Carroll K J, Goswami R, Willard M A, Kurihara L, Gjoka M and Kalogirou O 2010 High coercivity cobalt carbide nanoparticles processed via polyol reaction: a new permanent magnet material *J. Phys. D. Appl. Phys.* **43** 165003

- [29] Zamanpour M, Bennett S, Taheri P, Chen Y and Harris V G 2014 Magnetic properties and scale-up of nanostructured cobalt carbide permanent magnetic powders *J. Appl. Phys.* **115** 17A747
- [30] El-Gendy A A, Qian M, Huba Z J, Khanna S N and Carpenter E E 2014 Enhanced magnetic anisotropy in cobalt-carbide nanoparticles *Appl. Phys. Lett.* **104** 23111
- [31] Okamoto H 2010 *Desk handbook : phase diagrams for binary alloys* (Materials Park: ASM International)
- [32] Zhao X, Ke L, Wang C-Z and Ho K-M 2016 Metastable cobalt nitride structures with high magnetic anisotropy for rare-earth free magnets *Phys. Chem. Chem. Phys.* **18** 31680–90
- [33] Wu S Q, Ji M, Wang C Z, Nguyen M C, Zhao X, Umemoto K, Wentzcovitch R M and Ho K M 2014 An adaptive genetic algorithm for crystal structure prediction. *J. Phys. Condens. Matter* **26** 35402
- [34] Deaven D M and Ho K M 1995 Molecular Geometry Optimization with a Genetic Algorithm *Phys. Rev. Lett.* **75** 288–91
- [35] Zhang Y-J, Yao Q, Zhang Y, Cui T-Y, Li D, Liu W, Lawrence W and Zhang Z-D 2008 Solvothermal Synthesis of Magnetic Chains Self-Assembled by Flowerlike Cobalt Submicrospheres *Cryst. Growth Des.* **8** 3206–12
- [36] Rao K S, Balaji T, Lingappaa Y, Reddy M R P and Prakash T L 2013 Synthesis and characterisation of ferromagnetic hexagonal cobalt nanoparticles *J. Exp. Nanosci.* **8** 162–70

- [37] Goyal R, Lamba S and Annapoorni S 2016 Growth of cobalt nanoparticles in Co–Al₂O₃ thin films deposited by RF sputtering *Phys. status solidi* **213** 1309–16
- [38] Arora N and Jagirdar B R 2012 Carbonization of solvent and capping agent based enhancement in the stabilization of cobalt nanoparticles and their magnetic study *J. Mater. Chem.* **22** 20671–9
- [39] Zhao X Q, Veintemillas-Verdaguer S, Bomati-Miguel O, Morales M P and Xu H B 2005 Thermal history dependence of the crystal structure of Co fine particles *Phys. Rev. B* **71** 24106
- [40] Sears V F 1992 Neutron scattering lengths and cross sections *Neutron News* *Neutron News* **3** 26–37
- [41] Xu X, Zhang X, Yin Y, Balasubramanian B, Das B, Liu Y, Huq A and Sellmyer D J 2017 Anti-site mixing and magnetic properties of Fe₃Co₃Nb₂ studied via neutron powder diffraction *J. Phys. D: Appl. Phys.* **50** 25002
- [42] Balasubramanian B, Das B, Skomski R, Zhang W Y and Sellmyer D J 2013 Novel nanostructured rare-earth-free magnetic materials with high energy products *Adv. Mater.* **25** 6090–3
- [43] McGuire M A and Rios O 2015 Evolution of magnetic properties and microstructure of Hf₂Co₁₁B alloys *J. Appl. Phys.* **117** 53912

Appendix B: Symmetry Analysis of the Spin Structure for CoSi by the Group Theory

Here we discuss the possible spin structure for the B20 structure with different propagation vectors.

B.1 Crystal Symmetry and Space Group

The symmetry of a crystal structure is described by the space group. The crystal structure returns to its equivalent position after a symmetry operation within the group. This sets the symmetry of the system. When properties of the system change with the symmetry operations, their behaviors (transformation) are representations of the groups. The irreducible representations are the basis that can be used to describe all possible behaviors.

Here we are concerned with the space group $P2_13$ (198). There are 12 members in the group. The basic information of the group is displayed in the tables below. Sm means symmetry operation.

		Inverse
Sm1	x, y, z	Sm1
Sm2	$x+1/2, -y+1/2, -z$	Sm2
Sm3	$-x, y+1/2, -z+1/2$	Sm3
Sm4	$-x+1/2, -y, z+1/2$	Sm4
Sm5	z, x, y	Sm9
Sm6	$z+1/2, -x+1/2, -y$	Sm12
Sm7	$-z, x+1/2, -y+1/2$	Sm10
Sm8	$-z+1/2, -x, y+1/2$	Sm11
Sm9	y, z, x	Sm5
Sm10	$y+1/2, -z+1/2, -x$	Sm7
Sm11	$-y, z+1/2, -x+1/2$	Sm8

Sm12	$-y+1/2, -z, x+1/2$	Sm6
------	---------------------	-----

I: inversion. R(X180): rotation along the x -axis by 180 degrees.

The multiplication table:

	Sm1	Sm2	Sm3	Sm4	Sm5	Sm6	Sm7	Sm8	Sm9	Sm10	Sm11	Sm12
Sm1	Sm1	Sm2	Sm3	Sm4	Sm5	Sm6	Sm7	Sm8	Sm9	Sm10	Sm11	Sm12
Sm2	Sm2	Sm1	Sm4	Sm3	Sm6	Sm5	Sm8	Sm7	Sm10	Sm9	Sm12	Sm11
Sm3	Sm3	Sm4	Sm1	Sm2	Sm7	Sm8	Sm5	Sm6	Sm11	Sm12	Sm9	Sm10
Sm4	Sm4	Sm3	Sm2	Sm1	Sm8	Sm7	Sm6	Sm5	Sm12	Sm11	Sm10	Sm9
Sm5	Sm5	Sm7	Sm8	Sm6	Sm9	Sm11	Sm12	Sm10	Sm1	Sm3	Sm4	Sm2
Sm6	Sm6	Sm8	Sm7	Sm5	Sm10	Sm12	Sm11	Sm9	Sm2	Sm4	Sm3	Sm1
Sm7	Sm7	Sm5	Sm6	Sm8	Sm11	Sm9	Sm10	Sm12	Sm3	Sm1	Sm2	Sm4
Sm8	Sm8	Sm6	Sm5	Sm7	Sm12	Sm10	Sm9	Sm11	Sm4	Sm2	Sm1	Sm3
Sm9	Sm9	Sm12	Sm10	Sm11	Sm1	Sm4	Sm2	Sm3	Sm5	Sm8	Sm6	Sm7
Sm10	Sm10	Sm11	Sm9	Sm11	Sm2	Sm3	Sm1	Sm4	Sm6	Sm7	Sm8	Sm8
Sm11	Sm11	Sm10	Sm12	Sm9	Sm3	Sm2	Sm4	Sm1	Sm7	Sm8	Sm8	Sm5
Sm12	Sm12	Sm9	Sm11	Sm10	Sm4	Sm1	Sm3	Sm2	Sm8	Sm8	Sm7	Sm6

Character table

	Class 1 Sm1	Class 2 (3) Sm2-sm4	Class 3 (4) Sm5-sm8	Sm4 (4) Sm9-sm12	
Γ_1	1	1	1	1	1
Γ_2	1	1	$\exp\left(i\frac{2\pi}{3}\right)$	$\exp\left(-i\frac{2\pi}{3}\right)$	1
Γ_3	1	1	$\exp\left(-i\frac{2\pi}{3}\right)$	$\exp\left(i\frac{2\pi}{3}\right)$	1
Γ_4	3	-1	0	0	3
$\Gamma_{Cos i}$	12	0	0	0	

Below we analyze the possible spin structures allowed by the crystal structure.

B.2 Propagation Vector $\vec{k} = (0, 0, 0)$

In this case, the full symmetry of the original $P2_13$ space group retains. Therefore, we do not have to make any changes to the group. This is also what we call the “Large representation”.

Basis vectors of the decomposed representations

For the propagation vector $\vec{k} = (0,0,0)$, the representation is magnetic moments on 4 Co atoms: $\vec{m}_i, i = 1,2,3,4$.

We only need to consider the magnetic atoms whose positions are:

Atom1: (x, x, x)

Atom2: $(-x+1/2, -x, x+1/2)$

Atom3: $(-x, x+1/2, -x+1/2)$

Atom4: $(x+1/2, -x+1/2, -x)$

where x represents the small distortion from the face center cubic structure.

The dimension of the representation is $l = 3 * 4 = 12$. The basis of the representation is $\{m_{1,x}, m_{1,y}, m_{1,z}, m_{2,x}, m_{2,y}, m_{2,z}, m_{3,x}, m_{3,y}, m_{3,z}, m_{4,x}, m_{4,y}, m_{4,z}\}$

Each irreducible representation corresponds to a subspace defined by a linear combination of l_i vectors and an eigen energy, where l_i is the dimension of the subspace. The vectors can be found using the software BasIreps in the FullProf package.

	Atom1	Atom2	Atom3	Atom4
Γ_1	(1, 1, 1)	(-1, -1, -1)	(-1, 1, -1)	(1, -1, -1)
Γ_2	$(1, e^{-\frac{i2\pi}{3}}, e^{\frac{i2\pi}{3}})$	$(-1, e^{\frac{i\pi}{3}}, e^{\frac{i2\pi}{3}})$	$(-1, e^{-\frac{i2\pi}{3}}, e^{-\frac{i\pi}{3}})$	$(1, e^{\frac{i\pi}{3}}, e^{-\frac{i\pi}{3}})$
Γ_3	$(1, e^{\frac{i2\pi}{3}}, e^{-\frac{i2\pi}{3}})$	$(-1, e^{-\frac{i\pi}{3}}, e^{-\frac{i2\pi}{3}})$	$(-1, e^{\frac{i2\pi}{3}}, e^{\frac{i\pi}{3}})$	$(1, e^{-\frac{i\pi}{3}}, e^{\frac{i\pi}{3}})$
$\Gamma_{4,1}$	(1, 0, 0) (0, 1, 0) (0, 0, 1)	(1, 0, 0) (0, 1, 0) (0, 0, 1)	(1, 0, 0) (0, 1, 0) (0, 0, 1)	(1, 0, 0) (0, 1, 0) (0, 0, 1)
$\Gamma_{4,2}$	(1, 0, 0) (0, 1, 0) (0, 0, 1)	(-1, 0, 0) (0, 1, 0) (0, 0, -1)	(1, 0, 0) (0, -1, 0) (0, 0, -1)	(-1, 0, 0) (0, -1, 0) (0, 0, 1)
$\Gamma_{4,3}$	(1, 0, 0) (0, 1, 0) (0, 0, 1)	(1, 0, 0) (0, -1, 0) (0, 0, -1)	(-1, 0, 0) (0, -1, 0) (0, 0, -1)	(-1, 0, 0) (0, 1, 0) (0, 0, 1)

Γ_1, Γ_2 and Γ_3 are non-collinear AFM states.

$\Gamma_{4,1}$ is an FM magnetic structure.

$\Gamma_{4,2}$ and $\Gamma_{4,3}$ can be both collinear and non-collinear AFM magnetic structures.

B.3 Propagation Vector $\vec{k} // [100]$

Here we need to use the multiplier group. In this case, we first pick the $\{R|\tau\}$ members where $R\vec{k} = \vec{k}$. This leads to only two members. Sm1 (x, y, z) and Sm2 (x+1/2, -y+1/2, -z).

Character table

	Class 1 Sm1	Class 2 (1) Sm2	
Γ_1	1	$-e^{ika/2}$	3
Γ_2	1	$-e^{ika/2}$	3
Γ_{CoSi}	6	0	

Representation decomposition

There are two representations, and each of them contains two atoms.

		Inverse
Sm1	x, y, z	Sm1
Sm2	x+1/2, -y+1/2, -z	Sm2

The irreducible representations can be found as the following.

For Atom 1 and Atom 2 (group I)

	Atom 1	Atom 2
$\Gamma_{1,1}(I)$	(1,0,0)	$(-e^{-ika/2}, 0, 0)$
$\Gamma_{1,2}(I)$	(0,1,0)	$(0, e^{-ika/2}, 0)$
$\Gamma_{1,3}(I)$	(0,0,1)	$(0, 0, e^{-ika/2})$
$\Gamma_{2,1}(I)$	(1,0,0)	$(e^{-ika/2}, 0, 0)$
$\Gamma_{2,2}(I)$	(0,1,0)	$(0, -e^{-ika/2}, 0)$
$\Gamma_{2,3}(I)$	(0,0,1)	$(0, 0, -e^{-ika/2})$

The result is identical for Atom 3 and Atom 4 (group II)

	Atom 3	Atom 4
$\Gamma_{1,1}(II)$	(1,0,0)	$(-e^{-ika/2}, 0, 0)$
$\Gamma_{1,2}(II)$	(0,1,0)	$(0, e^{-ika/2}, 0)$
$\Gamma_{1,3}(II)$	(0,0,1)	$(0, 0, e^{-ika/2})$
$\Gamma_{2,1}(II)$	(1,0,0)	$(e^{-ika/2}, 0, 0)$
$\Gamma_{2,2}(II)$	(0,1,0)	$(0, -e^{-ika/2}, 0)$
$\Gamma_{2,3}(II)$	(0,0,1)	$(0, 0, -e^{-ika/2})$

For a helical spin structure, the following conditions are required: (1) All the spins are perpendicular to \vec{k} . (2) Phase difference between spins follows propagation $\vec{S}(\vec{r}) = \vec{S}_0 e^{-i\vec{k}\cdot\vec{r}}$. (3) The magnitude of the spins is constant.

For a helical spin structure of $\vec{k} // [100]$, one expects an intrinsic phase difference between atoms 1&3 and atoms 2&4 according to $e^{-i\vec{k}\cdot\vec{r}} = e^{-\frac{ika}{2}}$, which can be clearly seen in $\Gamma_{2,1}$, $\Gamma_{1,2}$, and $\Gamma_{1,3}$, for both atom groups **I** and **II**. Among them, $\Gamma_{1,2}$, and $\Gamma_{1,3}$ are perpendicular to \vec{k} .

To make the spin rotate along \vec{k} , one needs to combine $\Gamma_{2,1}$ and $\Gamma_{1,2}$. Consider the spin structures formed using a linear combination

$$\Gamma_h(\mathbf{I}, \mathbf{II}) = \Gamma_{1,2}(\mathbf{I}, \mathbf{II}) + e^{i\phi} \Gamma_{1,3}(\mathbf{I}, \mathbf{II}) \quad (\mathbf{B.1})$$

atom 1 and atom 3 have the spin state $(0, 1, e^{i\phi}) e^{-i\vec{k}\cdot\vec{r}}$ while atom 2 and atom 4 have spin states of $(0, 1, e^{i\phi}) e^{-\left(\frac{ika}{2} + i\vec{k}\cdot\vec{r}\right)}$. Using $(0, 1, e^{i\phi}) e^{-i\vec{k}\cdot\vec{r}}$ as an example, the spin magnitude is $\sqrt{\cos^2(\vec{k}\cdot\vec{r}) + \cos^2(\vec{k}\cdot\vec{r} - \phi)}$. To make it constant, $\phi = \pm \frac{\pi}{2}$ is required, which corresponds to the opposite chirality.

Therefore, the helical spin structure is

$$\Gamma_h(\mathbf{I}, \mathbf{II}) = \Gamma_{1,2}(\mathbf{I}, \mathbf{II}) \pm i\Gamma_{1,3}(\mathbf{I}, \mathbf{II}) \quad (\mathbf{B.2})$$

One can verify that this satisfies all three conditions. In particular, when k is small (wavelength much longer than the unit cell), the spins within a unit cell are nearly parallel to each other.

The exchange interaction that requires nearly parallel alignment between the nearest neighbors connects the two groups. Hence, the helical structures including all atoms are

$$[\Gamma_{1,2}(\text{I}) + i\Gamma_{1,3}(\text{I}) \text{ and } \Gamma_{1,2}(\text{II}) + i\Gamma_{1,3}(\text{II})] \text{ and}$$

$$[\Gamma_{1,2}(\text{I}) - i\Gamma_{1,3}(\text{I}) \text{ and } \Gamma_{1,2}(\text{II}) - i\Gamma_{1,3}(\text{II})] \text{ for the opposite chirality.}$$

B.4 Propagation Vector $\vec{k} // [111]$

In this case, we first pick the $\{R|\tau\}$ members where $R\vec{k} = \vec{k}$. This leads to three members: Sm1 (x, y, z), Sm5 (z, x, y), Sm9 (y, z, x).

Character table

	Class 1 Sm1	Class 2 Sm5	Class 3 Sm9	
Γ_1	1	1	1	1
Γ_2	1	a	b	1
Γ_3	1	b	a	1
Γ_{CoSi}	3	0	0	

$$a = e^{\frac{i2\pi}{3}}, b = e^{\frac{i4\pi}{3}}$$

Representation decomposition

There are two representations.

		Inverse
Sm1	x, y, z	Sm1
Sm5	z, x, y	Sm9
Sm9	y, z, x	Sm5

One contains one atom (atom1) at (x, x, x) . The other contains three other atoms.

The irreducible representations can be found using the software BasIreps.

For Atom 1 (group I)

	Atom 1
$\Gamma_1(\mathbf{I})$	(1,1,1)
$\Gamma_2(\mathbf{I})$	$(1, e^{-\frac{i2\pi}{3}}, e^{\frac{i2\pi}{3}})$
$\Gamma_3(\mathbf{I})$	$(1, e^{\frac{i2\pi}{3}}, e^{-\frac{i2\pi}{3}})$

For Atom 2, Atom 3, and Atom 4 (group II)

	Atom 2	Atom 3	Atom 4
$\Gamma_{1,1}(\mathbf{II})$	(1,0,0)	(0,1,0)	(0,0,1)
$\Gamma_{1,2}(\mathbf{II})$	(0,1,0)	(0,0,1)	(1,0,0)
$\Gamma_{1,3}(\mathbf{II})$	(0,0,1)	(1,0,0)	(0,1,0)
$\Gamma_{2,1}(\mathbf{II})$	(1,0,0)	$(0, e^{-\frac{i2\pi}{3}}, 0)$	$(0, 0, e^{\frac{i2\pi}{3}})$
$\Gamma_{2,2}(\mathbf{II})$	(0,1,0)	$(0, 0, e^{-\frac{i2\pi}{3}})$	$(e^{\frac{i2\pi}{3}}, 0, 0)$
$\Gamma_{2,3}(\mathbf{II})$	(0,0,1)	$(e^{-\frac{i2\pi}{3}}, 0, 0)$	$(0, e^{\frac{i2\pi}{3}}, 0)$
$\Gamma_{3,1}(\mathbf{II})$	(1,0,0)	$(0, e^{\frac{i2\pi}{3}}, 0)$	$(0, 0, e^{-\frac{i2\pi}{3}})$
$\Gamma_{3,2}(\mathbf{II})$	(0,1,0)	$(0, 0, e^{\frac{i2\pi}{3}})$	$(e^{-\frac{i2\pi}{3}}, 0, 0)$
$\Gamma_{3,3}(\mathbf{II})$	(0,0,1)	$(e^{\frac{i2\pi}{3}}, 0, 0)$	$(0, e^{-\frac{i2\pi}{3}}, 0)$

One may verify that $\Gamma_2(\mathbf{I})$ and $\Gamma_3(\mathbf{I})$ already satisfies all the condition for helical spin structures for atom 1, corresponding to the opposite chirality.

$\Gamma_2(\mathbf{II})$ and $\Gamma_3(\mathbf{II})$ also naturally form two subspaces in which the sum of the spins forms the helical structure with opposite chirality. To form a helical structure, $\vec{S}(\vec{r}) = \vec{S}_0(\vec{r})e^{i\vec{k}\cdot\vec{r}}$ needs to be satisfied, where \vec{k} is along the [111] direction. The spins should be the same for atom 2, atom 3, and atom 4. Taking $\Gamma_2(\mathbf{II})$ as an example, a linear combination

$$\Gamma_{2,1}(\mathbf{II}) + e^{-\frac{i2\pi}{3}}\Gamma_{2,2}(\mathbf{II}) + e^{-\frac{i4\pi}{3}}\Gamma_{2,3}(\mathbf{II}) \quad (\mathbf{B.3})$$

makes the spins on atoms 2-4 rotate along \vec{k} .

To include both groups of atoms, the phase difference between the atom group I and the atom group II can be calculated as $e^{i\vec{k}\cdot\vec{r}} = e^{-\frac{ika}{\sqrt{3}}}$.

Hence, the helical structures including all atoms are

$$[\Gamma_2(\mathbf{I})e^{\frac{ika}{\sqrt{3}}} \text{ and } \Gamma_{2,1}(\mathbf{II}) + e^{-\frac{i2\pi}{3}}\Gamma_{2,2}(\mathbf{II}) + e^{-\frac{i4\pi}{3}}\Gamma_{2,3}(\mathbf{II})], \text{ and}$$

$$[\Gamma_3(\mathbf{I})e^{\frac{ika}{\sqrt{3}}} \text{ and } \Gamma_{3,1}(\mathbf{II}) + e^{\frac{i2\pi}{3}}\Gamma_{3,2}(\mathbf{II}) + e^{\frac{i4\pi}{3}}\Gamma_{3,3}(\mathbf{II})], \text{ for the opposite chirality respectively.}$$

B.5 Propagation Vector $\vec{k} // [110]$

In this case, we first pick the $\{R|\tau\}$ members for the multiplier group where $R\vec{k} = \vec{k}$. This leads to only one member: $S_{m1}(x, y, z)$.

Character table

	Class 1 Sm1	
Γ_1	1	3
Γ_{CoSi}	3	

Representation decomposition

		Inverse
Sm1	x, y, z	Sm1

The irreducible representation can be easily described as,

	Atom 1/Atom 2/Atom 3/Atom 4
Γ_1	(1,0,0)
Γ_2	(0,1,0)
Γ_3	(0,0,1)

Unlike the case with $\vec{k} // [111]$ and $\vec{k} // [100]$, where the intrinsic helical structure characteristics are built on the spin structure basis, for $\vec{k} // [110]$, no such connections between spins are seen, which means that the formation of helical structures is unlikely.

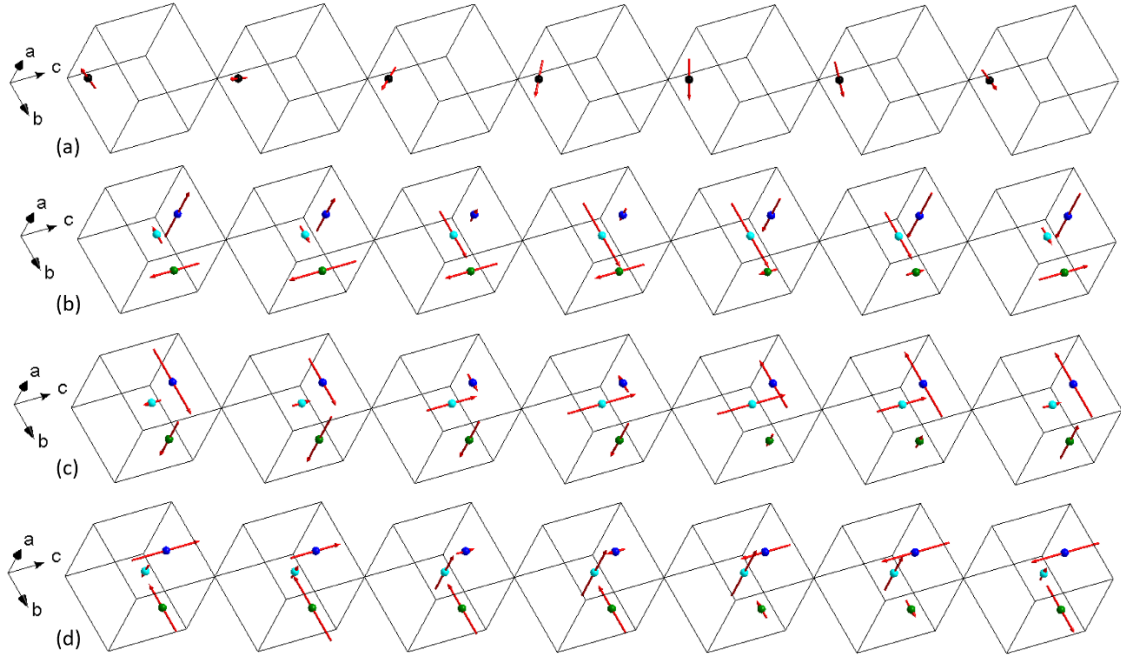


Figure B.1: Illustration of spin structure basis for $\vec{k}_s // [111]$. Atoms with the same color represent the same relative position in the unit cell. (a) magnetic structure $\Gamma_2(\text{I})$ of atoms in group I. (b)-(d) three one-dimensional magnetic structures $\Gamma_{2,1}(\text{II})$, $\Gamma_{2,2}(\text{II})$, and $\Gamma_{2,3}(\text{II})$ of atoms in group II. Note that these are only the basis of spins structures allowed by the crystal structures. The real spin structure may be their combination under additional constrictions (e.g., exchange interaction, see text).